



Characterization of Flow Dynamics in a Heart Simulator by means of PIV

Charakterisierung der Strömungsdynamik in einem Herzsimulator
mittels PIV

Master Thesis of

Luis Neff

At the Department of Mechanical Engineering,
Institute of Fluid Mechanics

Advisors: Prof. Dr.-Ing. Bettina Frohnafel
Dr.-Ing. Robin Leister
Dr.-Ing. Jochen Kriegseis
Dr.-Ing. Alexander Stroh
M.Sc. Roger Karl

Duration: May 2023 – November 2023

Task

April 27, 2023

Master-Thesis – experimental

Characterization of flow dynamics in a heart simulator by means of PIV

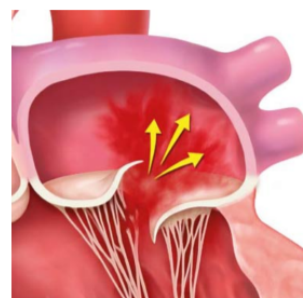
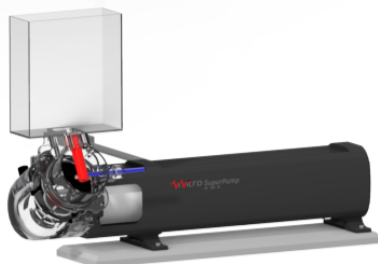
Motivation

Heart valve surgery is a very complex procedure which requires years of training and regular performance to be mastered. Recently, a simulator for experimental reproduction of the mitral valve dynamics has been developed at the University Hospital of Heidelberg in order to improve the patient-specific training and surgery planning. After successful tests, in the next step it is planned to analyze the dynamics of the flow and especially the back-flow (regurgitation jet) through a leaky heart valve in order to find connection between heart pathologies and different regurgitations jets (size/shape etc). The aim of the work is to improve understanding of the flow dynamics and link it to particular heart valve mechanics.

Content of the Thesis

In this thesis we carry out PIV experiments of pulsating flow through a heart valve simulator and investigate the effects of different pathologies (diseases) and of different load conditions (amplitude and frequency of the pump) on the flow:

- Classification of current scientific literature on PIV and heart valve flows.
- Preparation and conduction of different PIV experiments: e.g.: generic geometries as phase-averaged, eccentric jets, patient-specific valves
- Development of Post-processing methods to quantify and compare results e.g. vortex-identification methods
- facultativ: stereo PIV measurements



Requirements:

Basic knowledge in PIV or experimental techniques

Beneficial Skills:

python or matlab, vortex identification techniques

Start: immediately

Contact:

Robin Leister, Alexander Stroh

Institute of Fluid Mechanics

Kaiserstraße 10,

Room 110, Geb. 10.95

☎ +49 721 608-48151

✉ robin.leister@kit.edu

I declare that I have developed and written the enclosed thesis completely by myself, and have not used sources or means without declaration in the text.

Karlsruhe, 09. 11. 2023

.....
(Luis Neff)

Acknowledgement

I would like to express my gratitude to all those who have contributed to the success of this project.

I extend my special thanks to my supervisor, Dr.-Ing. Robin Leister, whose proficient guidance and thought-provoking recommendations proved invaluable to the completion of this work. I valued the professional communication and friendly working environment. Robin provided me with the optimum amount of autonomy to work independently on my preferred areas and consistently gave me precise advice and guidance on how to proceed.

Additionally, I am deeply grateful to Dr.-Ing. Jochen Kriegseis for entrusting me with the topic of this thesis and making it possible for me to start without any complications. During my work at the Institute of Fluid Mechanics (ISTM), Jochen's support in all experimental questions and his helping hand whenever needed was especially valuable.

In addition, I want to thank M.Sc. Roger Karl for his competent assistance in medical questions and his active support in the operation of the heart simulator. I especially admire his easygoing collaboration style and his innovative problem-solving skills. Roger also allowed me to observe a Mitral valve replacement surgery at the University clinic in Heidelberg. This was not only an interesting experience in itself, but also increased my motivation for the subject and contributed to my understanding of the problem. I express my gratitude for that opportunity.

I want to thank Dr. Alexander Stroh for bringing the project to the ISTM and for the stimulating discussions. Alex's dedication to this project was evident in every meeting.

I would like to express my gratitude to Prof. Dr.-Ing. Frohnapfel for providing me with the opportunity to work on an intriguing and interdisciplinary Master's thesis at the ISTM, KIT. I have thoroughly enjoyed working at ISTM and value the amiable working environment that you have established at your institute.

Kurzfassung

Diese Arbeit konzentriert sich auf die strömungsmechanische Charakterisierung von Regurgitationsjets, die durch insuffiziente Mitralklappen entstehen. Die Untersuchungen wurden mit Particle Image Velocimetry (PIV) Messtechnik und eigens entwickelten Post-Processing-Skripten durchgeführt. Die Mitralsuffizienz ist die häufigste Form der Herzklappenerkrankung und bezeichnet den Rückfluss von Blut in den linken Vorhof aufgrund einer insuffizienten Mitralklappe, was zu verschiedenen gesundheitlichen Komplikationen führt. Eine genaue Diagnose der Mitralsuffizienz ist für eine erfolgreiche Behandlung von entscheidender Bedeutung. Bei komplexen Regurgitationsjets ist die Aussagekraft herkömmlicher Methoden jedoch limitiert. Diese Studie zielt darauf ab, das Verständnis für die komplexe Strömungssituation von Regurgitationsjets zu verbessern und so zur Verbesserung der Diagnose und damit der Therapie beizutragen.

Dazu wurden phasengemittelte und phasenaufgelöste 2D2C-PIV-Experimente für verschiedene Mitralklappengeometrien im Herzsimulator durchgeführt. Der Laserlichtschnitt wurde traversiert, um quasi 3D Geschwindigkeitsdaten zu erhalten. Drei generische Mitralklappengeometrien unterschiedlicher Größe wurden untersucht: eine runde Lochblende, ein spitzen Oval und eine Tropfenform. Zusätzlich wurden eine exzentrische Klappengeometrie und eine patientenspezifische Klappe untersucht. Die Geschwindigkeitsdaten wurden bezüglich zeitlichem Strömungsverlauf und Form des Jets untersucht. Die Wirbel-dynamische Untersuchung basierte auf der Wirbelstärke, sowie dem Q - und Γ_1 -Kriterium. Die Ergebnisse der generischen Mitralklappen zeigten typische Merkmale von pulsierenden Jets. Unterschiede in der radialen Geschwindigkeitsverteilung konnten mit den unterschiedlichen Öffnungsformen in Verbindung gebracht werden. Die Sattel-behafteten radialen Profile der Axialgeschwindigkeit am Auslass können durch die geringe Einlasslänge und die scharfen Öffnungsränder erklärt werden. Zusätzlich zu periodisch wiederkehrenden Anfangswirbeln wurden Kelvin-Helmholtz-Instabilitäten in der Grenzschicht stromaufwärts detektiert. Die exzentrische Klappengeometrie zeigte ähnliche Beobachtungen, jedoch um den Winkel der Exzentrizität gedreht. Die patientenspezifische Mitralklappe ergab, im Vergleich zu den generischen Fällen, eine deutlich instabilere und turbulenterere Strömungssituation, was auf die komplexere Öffnungsform, die höhere Reynoldszahl und die größere Flexibilität der Klappenblätter zurückzuführen ist. Form und Richtung des Jets unterlagen starken zeitlichen und räumlichen Schwankungen. Gemittelte PIV-Auswertungen ergaben ein dominantes Anfangswirbelpaar, während Einzelbildpaar-auswertungen keine eindeutige Wirbelerkennung zeigten. Für zukünftige Untersuchungen wird empfohlen, das Innere des Atriums mit einer realistischeren Geometrie zu modellieren und Hochgeschwindigkeits-PIV zu verwenden.

Abstract

This thesis concentrates on characterizing the fluid mechanics of Mitral regurgitation jets within a heart simulator via Particle Image Velocimetry (PIV) and custom developed post-processing scripts. Mitral regurgitation is the most common type of valvular heart disease and is caused by blood flowing back into the left atrium due to an insufficient Mitral valve, resulting in several complications. It is essential to diagnose Mitral regurgitation accurately for successful treatment, but conventional diagnosis techniques have major limitations in complex flow situations. This study aims to enhance the comprehension of the complex flow situation of regurgitant jets and thus contribute to the diagnosis of Mitral regurgitation. Phase-averaged and phase-resolved 2D2C PIV experiments were conducted for varying Mitral valve geometries incorporated into a heart simulator. The laser light sheet was traversed to retrieve quasi 3D velocity data. Three generic Mitral valves geometries of different sizes were investigated: a pinhole, a pointed oval and a drop shape. In addition, an eccentric valve geometry and a patient-specific Mitral valve were investigated. The velocity data collected was analysed for the jet's temporal and spatial development. Evaluation of the vorticity and the application of the Q - and Γ_1 -criterion formed the vortex dynamical analysis of the jet.

The findings from the generic Mitral valves showed typical characteristics of pulsating free jets in terms of potential core length and axial velocity evolution. Differences in the spreading and radial distribution of velocity could be related to the different orifice shapes. Saddle-backed radial profiles of axial velocity observed near the outlet can be explained by the Mitral valve's geometrical properties. Specifically, the small inlet length and sharp orifice edges may account for this observation. Periodic starting vortex pairs were detected in addition to Kelvin-Helmholtz instabilities in the upstream boundary layer. The valve producing the eccentric jet showed similar observations but rotated with the angle of eccentricity. The patient-specific Mitral valve showed a significantly more unsteady and turbulent flow situation compared to the generic cases, which can be attributed to the more complex orifice shape, higher Reynolds number and increased flexibility of the valve leaflets. The jet's shape and direction experienced strong temporal and spatial fluctuations. Averaged PIV evaluations revealed a dominant starting vortex pair, while single image pair evaluations showed a disturbed and unsteady flow situation with no clear vortex detection. To pursue future investigations, it is recommended to model the atrium's interior with more realistic geometry and utilize high-speed PIV.

Contents

Task	ii
Acknowledgement	v
Kurzfassung	vi
Abstract	vii
Symbols and Abbreviations	x
List of Figures	xii
List of Figures	xvi
1 Introduction	1
1.1 Motivation	1
1.2 Objective	2
2 Fundamentals	3
2.1 Mitral Regurgitation	3
2.1.1 Anatomy and Function	3
2.1.2 Pathophysiology and Classification	7
2.1.3 Diagnosis Techniques	8
2.2 Fluid Mechanics	13
2.2.1 Fundamentals of Fluid Mechanics	13
2.2.2 Free Jets	15
2.2.3 Vortex Dynamics	20
2.3 Particle Image Velocimetry	23
2.3.1 Experimental Setup for PIV	23
2.3.2 Evaluation of PIV Recordings	25
2.4 State of the Art Research	28
3 Experimental Setup and Procedure	29
3.1 The Heart Simulator	29
3.2 PIV Setup and Procedure	33
4 Results and Discussion	36
4.1 Generic Mitral Regurgitation Orifice Phantoms	36
4.1.1 Temporal Velocity Distribution	37
4.1.2 Spatial Velocity Distribution	40
4.1.3 Vortex Detection	48
4.2 Eccentric Jet Producing Mitral Regurgitation Phantom	55
4.2.1 Temporal Velocity Distribution	55

4.2.2	Spatial Velocity Distribution	56
4.2.3	Vortex Detection	58
4.3	Patient-specific Mitral Valve	60
4.3.1	Temporal Velocity Distribution	61
4.3.2	Spatial Velocity Distribution	63
4.3.3	Vortex Detection	66
5	Conclusion and Outlook	70
	Bibliography	xvii
	Appendix	xxiv
A	Measurement Protocol	xxiv

Symbols and Abbreviations

Abbreviaton	Description
CW	Continuous wave
FOV	Field Of View
ISTM	Institut für Strömungsmechanik
KIT	Karlsruhe Institute of Technology
LA	Left Atrium
LV	Left Ventricle
MV	Mitral Valve
MR	Mitral Regurgitation
MROP	Mitral Regurgitation Orifice Phantom
NSE	Navier Stokes Equations
PISA	Proximal Isovelocity Surface Area
PIV	Particle Image Velocimetry
VC	Vena Contracta
VTI	Volume time integral
TEE	Transesophageal Echocardiog- raphy
US	Ultra sound

Symbol	Unit	Description
V_a	m/s	aliasing velocity
StrokeVol	ml	stroke volume of one heart beat
RVol	ml	regurgitation volume
f	Hz	frequency
f_v	Hz	vortex shedding frequency
D	m	orifice diameter
L	m	characteristic length
r	m	radius of a circular free jet
$r_{1/2}$	m	half-width radius
x_0	m	virtual origin of the jet
B	–	velocity decay rate
S	–	spreading rate
μ	kg/(m·s)	dynamic viscosity
ν	m ² /s	kinematic viscosity
ρ	kg/m ³	density
p	N/m ²	pressure
u	m/s	velocity, x component
u_0	m/s	velocity, x component at the outlet
$u_{0,\text{center}}$	m/s	velocity, x component at the outlet along the center line of the orifice
u_{avg}	m/s	average velocity, x component
u_{center}	m/s	velocity, x component along the center line of the orifice
u_{max}	m/s	maximum velocity, x component
u_{mag}	m/s	velocity magnitude
$u_{\text{mag},0}$	m/s	velocity magnitude at the outlet
$u_{\text{mag},0,\text{center}}$	m/s	velocity magnitude at the outlet along the center line of the orifice
$u_{\text{mag,avg}}$	m/s	average velocity magnitude
$u_{\text{mag,center}}$	m/s	velocity magnitude along the center line of the orifice
$u_{\text{mag,max}}$	m/s	maximum velocity magnitude
v	m/s	velocity, y component
ω	1/s	vorticity, z component
Q	1/s ²	value of the Q -criterion
Γ_1	–	value of the Γ_1 -criterion
P	m	reference point (Γ_1 -criterion)
Θ_M	°	angle of the local velocity field relative to a reference point P (Γ_1 -criterion)
U_M	m/s	velocity vector for the Γ_1 calculation
τ	Pa	shear stress
$\dot{\gamma}$	1/s	shear rate
t	s	time
Re	–	Reynolds number
St	–	Strouhal number
Wo	–	Womersley number
λ	nm	wave length
s^{xy}	μm/px	reproduction scale
M	–	magnification factor
τ_p	μs	particle response time
d_p	mm	particle diameter
y_{outlet}	mm	y -position of the outlet

List of Figures

2.1	Anatomy and normal blood flow in the human heart [62]	4
2.2	Blood flow into the left ventricle during diastole and ejection during systole. The subfigures a, b and c show the three different opening phases of the MV during diastole. The position d in the blood flow graph shows a slight back-flow of a healthy human heart due to a delay in the contraction of the papillary muscles and a billowing of the leaflets towards the left atrium. Figures are adopted from [15].	5
2.3	Extract of a Wiggers diagram as in [4]. It shows the pressure graphs in the aorta, the left atrium and the left ventricle for two cardiac cycles. Additionally, the points where the aortic valve and the Mitral valve open and close are marked.	6
2.4	Location and shape of the Mitral valve	6
2.5	Anatomy of the Mitral valve [70]	7
2.6	Carpentier type classification of Mitral regurgitation adapted from [28]. . .	8
2.7	Two exemplary images of the ultrasound modes used for Mitral regurgitation diagnosis; images from the measurements conducted by physicians in [48].	9
2.8	Left Ventricle (LV), left Atrium (LA), color jet area (Area), vena contracta (VC) and flow convergence (FC) recovered from a selected color-Doppler image, adapted by adding labels from [100]	10
2.9	Schematic presentation of the flow convergence method and relevant parameters, adapted from [100]. V_a = aliasing velocity, PISA = proximal isovelocity surface area, LV = left ventricle, LA = left atrium.	11
2.10	Shear stress τ as a function of shear rate $\dot{\gamma}$ for different kind of fluids. Pseudo-plastic shows the behavior of human blood. Adapted from [20]. . .	14
2.11	Schematic representation of broadening of the jets radial velocity profiles and the decrease of the mean velocity U_m along the axial direction, adopted from [32].	15
2.12	Radial profiles of axial velocity of a circular turbulent jet, adapted from [72]. $u(r)$ denotes the the axial velocity component and u_0 the outlet velocity of the jet.	16
2.13	Five representative snapshots of the peak velocity profiles of the transient Womersley flow in comparison to a plug-like ($\gamma = 9$) and parabolic profile ($\gamma = 2$); adopted from [78].	18
2.14	Saddle-backed outlet velocity profiles for different free jet cases observed by [85], [1], [45] and [74]	19
2.15	Axial development of the center line velocity for different inlet lengths compared to the orifice size, adopted from [23]. The black dots mark a thin orifice plate with with nearly zero inlet length.	20
2.16	Schematic representation of the chronological vortex roll-up in a Kelvin-Helmholtz instability, adapted from [35].	21

2.17	Vortex roll-up and decay in an axisymmetric jet boundary layer visualized by smoke, adopted from [64].	21
2.18	Schematic representation of the angle Θ_M of the local velocity field S relative to a reference point P , as used for the calculation of the Γ_1 -criterion [54]. U_M denotes an exemplary velocity vector in the flow field and PM the vector connecting vector with the reference point P	22
2.19	Experimental setup for planar 2C-2D PIV measurements: Tracer particles are illuminated by a laser light sheet and recorded by a high-speed camera. Via the displacement of particle images and the time delay between two subsequent images the velocity field of the flow is determined. Adopted from [75].	24
2.20	Geometric image reconstruction adopted from [75].	25
2.21	Schematic representation of PIV evaluation procedure	25
2.22	Composition of peaks in the cross-correlation function, adopted from [75]	26
2.23	Relative uncertainty for PIV measurements depending on pulse delay adopted from [75].	27
3.1	Model of the test setup including the heart simulator designed by Karl [48] (submitted), the PIV setup and an ultra sound probe used for the training and studies of physicians.	29
3.2	The artificial heart on the test rig at ISTM in Karlsruhe, photographed by Robin Leister.	30
3.3	Output signal of the ViVitro Labs Superpump for $f = 80$ bpm and StrokeVol = 115 ml; 4 period cycles.	31
3.4	First and last period cycle of a 10 minute at $f = 80$ bpm and StrokeVol = 115 ml recording of the ViVitro Labs cardiac piston pump used in the experiments. Δt indicates the the temporal deviation after 800 heart beats.	31
3.5	Overview of the laser-cutted MROP films and a photograph of the installed pinhole M Mitral regurgitation orifice phantom in the heart simulator.	32
3.6	Atrial and ventricular view of the patient-specific Mitral valve and a side view into the left ventricle of the heart simulator showing the artificial chords.	33
3.7	The heart simulator with the PIV setup in the ISTM lab, photographed by R. Leister.	34
4.1	Velocity magnitude u_{mag} fields for selected phases during regurgitation; pinhole L Mitral regurgitation orifice phantom.	38
4.2	Temporal course of the outlet velocity $u_0(y)$ for the Pinhole L. Green lines = phases with increasing velocity, red lines = phases with decreasing velocity.	38
4.3	Temporal flow velocity response of pinhole L to the piston travel distance of the cardiac piston pump represented by the output signal.	39
4.4	Consecutive PIV images in pixel-coordinates of Pinhole L showing the "wobbling" of the PVC film out the orifice during regurgitation.	40
4.5	Velocity magnitude u_{mag} distribution of three different orifice shapes at a fully developed state of the regurgitant jet.	41
4.6	Exemplary visualization of x/D position where radial distribution of the axial velocity is analysed and results for the pinhole shape, fully developed state, $t = 0.03$ s.	42
4.7	Radial distribution of the axial velocity for different x/D positions for slot and drop shaped orifices, fully developed state.	43
4.8	Center line velocity $u_{\text{center}}(x)$ for the fully developed state of the regurgitant jet originating from pinhole L; normalised for the maximum velocity in x -direction u_{max}	44

4.9	Center line velocities $u_{\text{center}}(x)$ for the fully developed phase of the regurgitant jet originating from pinholes S, M and L; all normalised for the respective maximum velocity in x -direction u_{max}	44
4.10	Center line velocities $u_{\text{center}}(x)$ for the fully developed phase of the regurgitant jet originating from pinholes S, M and L on an absolute axial coordinate scale; all normalised for the respective maximum velocity in x -direction u_{max}	45
4.11	Radius $r(x)$ and half-width radius $r_{1/2}(x)$ for two pinholes. The velocity magnitude u_{mag} calculation is based on phase-averaged PIV recordings.	45
4.12	Exemplary slices through the 3 dimensional 2 component velocity vector field of the slot and drop; calculated with phase-averaged PIV recordings.	46
4.13	Three dimensional spreading of the free jet originating from the slot; visualized via the velocity distribution in the x -planes at different axial positions x/D . The velocity magnitude $u_{\text{mag,avg}}$ is given in [m/s] and is calculated based on time-averaged PIV recordings.	47
4.14	Three dimensional spreading of the free jet originating from the drop; visualized via the velocity distribution in the x -planes at different axial positions x/D . The velocity magnitude $u_{\text{mag,avg}}$ is given in [m/s] and is calculated based on time-averaged PIV recordings.	47
4.15	Vorticity ω distribution for three different phases for pinhole L.	49
4.16	Vortex detection by means of the Q -criterium for three different phases during regurgitation for pinhole L.	50
4.17	Vortex detection by means of the Q - and Γ_1 -criterium for for pinhole L at $t = 770$ ms.	51
4.18	Vortex detection by means of Γ_1 for 9 phases of the regurgitant jet of slot L, separated by $\Delta t = 4$ ms each.	52
4.19	Outlet velocity in the center $u_{0,\text{center}}$ of slot L during regurgitation.	53
4.20	x -position (x -pos) of the strongest vortex detected by means of Γ_1 (blue solid line) and maximum vorticity magnitude $ \omega_{\text{max}} $ (red dotted line) for two period cycles (slot L).	53
4.21	x -position (x -pos) of the strongest vortex detected by means of Γ_1 (blue solid line) and maximum vorticity magnitude $ \omega_{\text{max}} $ (red dotted line) over the time t for 10 ms during regurgitation (slot L).	54
4.22	Overview of the velocity distribution of the eccentric jet producing Mitral valve phantom and temporal development of the velocity magnitude at the outlet ($u_{\text{mag},0}(y)$).	55
4.23	Outlet velocity magnitude $u_{\text{mag},0,\text{center}}$ for two period cycles for the eccentric jet producing Mitral valve phantom.	56
4.24	Spatial distribution of the velocity magnitude for the eccentric jet producing valve for the fully developed state of the regurgitant jet ($t = 785$ ms) rotated by 30°	57
4.25	Overview of the three-dimensional velocity magnitude u_{mag} distribution for the eccentric jet producing Mitral valve at a fully developed state	57
4.26	Vorticity and vortex detection by means of the Q - and Γ_1 -criterion for the eccentric jet producing Mitral valve phantom. The left side shows the time of emergence of the jet ($t = 720$ ms), while the right side shows the end of regurgitation ($t = 810$ ms).	58
4.27	Velocity fields for selected phases of the cardiac cycle for the patient-specific Mitral valve in the $z = 0$ plane.	61
4.28	Outlet velocity magnitude $u_{\text{mag},0,\text{center}}$ for two period cycles for the patient-specific Mitral valve ($z = 0$ plane).	62

4.29	Overview of the velocity magnitude $u_{\text{mag},0}$ of the patient-specific Mitral valve and temporal development of the velocity magnitude at the outlet ($u_{\text{mag},0}(y)$), both for the $z = 0$ plane.	63
4.30	Velocity magnitude $u_{\text{mag},0}$ of the patient-specific Mitral valve in different z -planes for $t = 70$ ms.	64
4.31	Velocity magnitude $u_{\text{mag},0}$ of the patient-specific Mitral valve for $z = +15$ mm and $t = 60$ ms.	65
4.32	Velocity magnitude u_{mag} in the outlet plane of the patient-specific Mitral valve at $t = 70$ ms. The height of the surface plot visualizes the magnitude of the velocity in addition to the color bar.	65
4.33	Vorticity and vortex detection by means of the Q - and Γ_1 -criterion for the patient-specific Mitral valve. The left side shows the time of emergence of the jet ($t = 30$ ms), while the right side shows the end of regurgitation ($t = 70$ ms), both for $z = 0$	67
4.34	Comparison of the Γ_1 application on the flow field for $t = 70$ ms and $z = -5$ mm for (a) a single image pair and (b) 40 in-phase averaged image pairs.	68
4.35	Γ_1 -criterion applied on in-phase averaged PIV evaluations of the patient-specific Mitral valve at $z = 0$ for six time steps during regurgitation.	69
A.1	Documentation of the PIV experiments conducted for this study, including the settings of the cardiac piston pump and the laser/ synchronizer.	xxv

List of Tables

2.1	Selection of MR severity grading parameters as presented by [100, 28] . . .	12
3.1	Sizes of regurgitation phantom orifices	32
4.1	Comparison of relevant parameters calculated from the phase-resolved PIV measurements for three orifice shapes.	37
4.2	Comparison of relevant parameters calculated from the phase-resolved PIV measurements in the z -plane $z = 0$ of the eccentric jet producing and patient-specific Mitral valve.	60

1. Introduction

In this chapter, the motivation for the subject of this thesis (Section 1.1) and the articulation of the objectives of the thesis (Section 1.2) will be pursued. Furthermore, the structure of the composition will be outlined together with the objectives.

1.1 Motivation

In 2022, cardiovascular diseases accounted for the highest number of deaths worldwide [86]. Additionally, Mitral valve insufficiency, also known as Mitral Regurgitation (MR), is the most prevalent valvular heart disease worldwide, affecting over 1.7% of the population [66, 25, 77]. MR denotes the backward flow of blood from the left ventricle (LV) into the left atrium (LA) due to an insufficient Mitral valve (MV). The retrograde flow is referred to as the regurgitation jet.

Common complications that arise in MR patients consist of the accumulation of fluid in the lungs due to increased pressure, a heightened risk of stroke due to distorted heart rhythm, and an unhealthy thickening of the atrial walls caused by the increased strain from the regurgitant jet [38, 87, 28, 14]. The latter two complications can be better understood by analysing the fluid dynamics of the regurgitant jet.

If left untreated, MR can worsen and potentially lead to death [77]. The appropriate treatment is heavily dependent on the diagnosis and the severity classification [100, 15]. Therefore, the precision and dependability of the diagnostic technique are of great interest. Presently, the most commonly used diagnostic technique is transesophageal echocardiography (TEE), an ultra sound technique, which has certain limitations and is significantly reliant upon the skill of the physician. The severity of Mitral regurgitation (MR) is generally underestimated by TEE-based assessments [100, 28, 3, 31]. In addition, complex regurgitant jets cannot be evaluated with confidence [96, 29, 73].

Particle Image Velocimetry (PIV) is an objective, reliable and accurate fluid mechanical measurement technique. While it cannot be conducted *in-vivo* (inside a living body), it provides crucial information on flow characteristics of regurgitant jets when tested *in-vitro* on a heart simulator. Thus, PIV is able to overcome the limitations of TEE-based methods and provides the opportunity to gain further fluid dynamic knowledge regarding regurgitant jets. With PIV, it is feasible to scrutinize both the temporal and spatial evolution of the regurgitant jet and recognise vortical structures in the flow [75, 84]. Therefore, it was selected as the measuring method for this examination.

1.2 Objective

The purpose of this research is to enhance comprehension of flow dynamics in the context of MR by means of PIV measurements on a heart simulator. To achieve this, an incremental approach is employed.

First, a generic case will be examined to verify the feasibility of PIV measurements on the heart simulator and to comprehend the flow dynamics for basic scenarios. Additionally, the impact of various orifice shapes on the regurgitant jet will be assessed. Furthermore, the generic cases enable a comparison with relevant fluid mechanical literature on pulsating free jets.

Second, an eccentric jet producing MV jet shall be designed and investigated, as this is a common case in MR patients and allows only a very limited diagnosis by common medical evaluation methods [73, 29, 96].

Third, a patient-specific MV shall be investigated providing information on the most realistic case possible in the heart simulator. The patient-specific MV experiment focuses on proofing the experimental setup for realistic cases and aims to characterise the flow dynamics of the regurgitant jet.

To achieve the goals, the following steps were taken.

- Research and classification of current scientific literature on PIV and MR. A summary of the medical and technical findings in this context can be found in Chapter 2. Chapter 2.1 focuses on the medical background of MR, Chapter 2.2 provides the relevant fluid mechanical fundamentals and Chapter 2.3 describes the theory of PIV.
- Design and manufacturing of different Mitral regurgitation orifice phantoms (MROPs) to be investigated in the heart simulator. In Chapter 3.1 the already existing setup of the heart simulator is described. The MROPs as well as the patient-specific MV are introduced.
- Preparation of the experimental setup for PIV measurements on the heart simulator. Chapter 3.2 describes the measurement technique deployed in this study.
- Conducting of phase-averaged and phase-resolved PIV measurements for all MROPs and the patient-specific valve. The experimental procedure is described in Chapter 3.2.
- Development of post-processing methods to quantify and compare results including vortex detection methods. The evaluation and interpretation of the generic MROPs measurements are found in Chapter 4.1. Chapter 4.2 and Chapter 4.3 provided the results of the eccentric jet producing and patient-specific MV respectively. A conclusion and outlook is provided in Chapter 5.

2. Fundamentals

In this chapter the basic knowledge essential for this study will be presented. Section 2.1 provides the medical and biological fundamentals necessary for the engineer reader to understand the basics of Mitral regurgitation (MR). In Section 2.2 the fluid mechanical theory is provided. This comprises the fundamental equations (Section 2.2.1), the theory of free jets including some special case relevant for this thesis (Section 2.2.2), and a section on vortex dynamics (Section 2.2.3). The theory regarding the measurement technique used in this study - Particle Image Velocimetry (PIV) - is summarized in Section 2.3. In Section 2.4 a brief literature review of relevant previous experimental studies on MR will be provided over-viewing the scientific state of the art in that regard.

2.1 Mitral Regurgitation

The heart is pumping blood through the circulatory system of the human body. Thereby all organs and tissues are supplied with vital oxygen and nutrients. The Mitral valve (MV) plays an essential role in the working principle of the human heart [52]. This will be explained in Section 2.1.1.

In case of an insufficient MV the function of the heart is hampered [25]. Section 2.1.2 explains the causes and effects of an insufficient valve (pathophysiology), and a classification of the disease is provided.

Various approaches to treating MR exist within the medical field. Depending on the mechanism behind and the severity of the MR, physicians have to decide which approach is followed. In evaluating the mechanism and severity of the disease at hand, the diagnosis technique plays an essential role. Section 2.1.3 provides an overview of the common methods in quantifying MR and outlines the limitations. [52, 38, 25, 15, 87]

2.1.1 Anatomy and Function

To comprehend the results of this study a few biological fundamentals of the human heart and its working principle, i.e. the cardiac cycle, need to be understood. In the following the parts of the human heart relevant for the study are described. After that, the Mitral valve and its role during the cardiac cycle is outlined.

The heart, which is a hollow organ, is approximately fist sized and positioned near the center of the thorax. It is divided into a right and left side, each consisting of two chambers, an atrium and a ventricle (Fig. 2.1a). The right heart is responsible for pumping the blood through the lungs (pulmonary circulation) into the left heart. The left heart

then pumps the blood further through the body circulation, back into the right heart. The four muscular chambers driving the circulation via contracting and relaxing are powered by electrical impulses generated within special cells in the heart, the so called sinuatrial node. [55, 52]

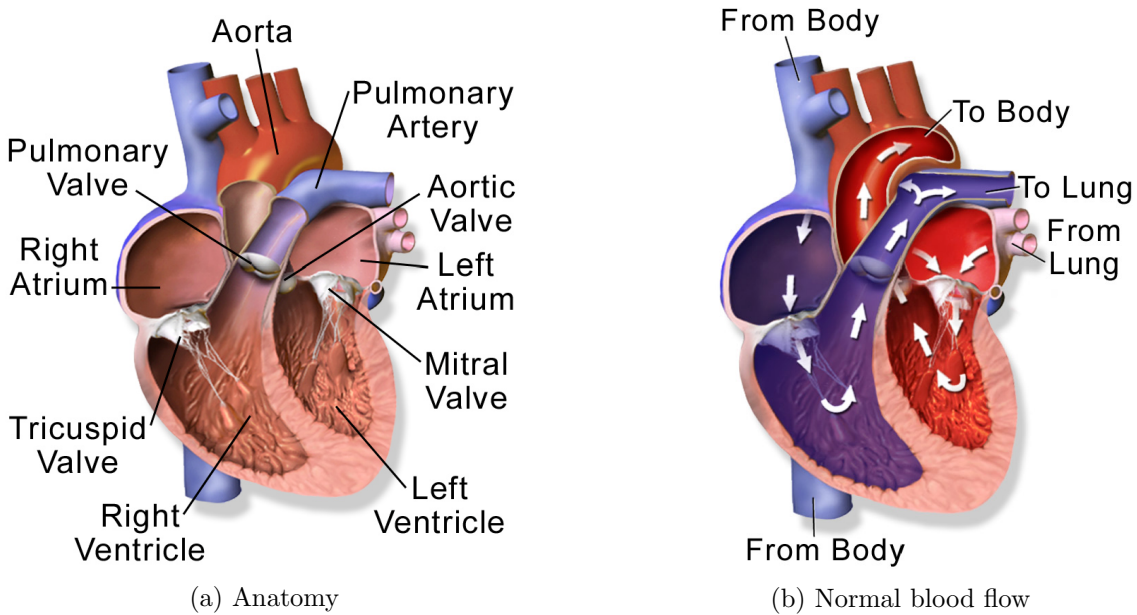


Figure 2.1: Anatomy and normal blood flow in the human heart [62]

Figure 2.1b shows the normal blood flow in a human heart during the cardiac cycle, which is an alternation between systole and diastole. The focus of this study is on the left heart, where the MV is located (Fig. 2.1a). Thus, the cardiac cycle will be described for the left heart only.

From the lungs, blood with high oxygen content, streams into the left atrium (LA) via the left pulmonary veins. During diastole, as shown on the right of Figure 2.2, the left ventricle (LV) dilates. This causes the MV to open and the filling of the LV begins. The diastolic filling is divided into three phases, as shown on the left of Figure 2.2. First, the leaflets of the MV open completely (Fig. 2.2(a)). After this full opening, the leaflets return to an intermediate position due to the decreased pressure. This reduces blood flow temporarily, as shown in Figure 2.2(b). Then, the contraction of the LA at the end of the diastole (Fig. 2.2(c)) increases blood flow again.

Subsequently, the ventricular contraction phase of the systole begins. When the pressure in the LV exceeds the pressure in the LA, the Mitral valve passively closes. Figure 2.2(d) shows, that there is a slight back-flow through the Mitral valve into the LA in a healthy human heart. This is due to a delay in the contraction of the papillary muscles and a billowing of the leaflets towards the LA [15].

To build up pressure further, the LV contracts. The MV is closed and the aortic valve opens due to the pressure gradient. Blood is ejected towards the body circulation (see bottom right of Fig. 2.2). For a healthy human at rest the aortic valve opens at a pressure of 80 mmHg and 70-80 ml of stroke volume are ejected into the aorta. During ejection, the pressure in the LV and thus in the aorta increases to 110-130 mmHg due to the contraction, for a healthy human heart. Those approximate values are dependent on age, size, gender, genetics and fitness of the patient. For patients with severe MR the peak pressure decrease by 10 to 15%. [83, 52, 38, 15]

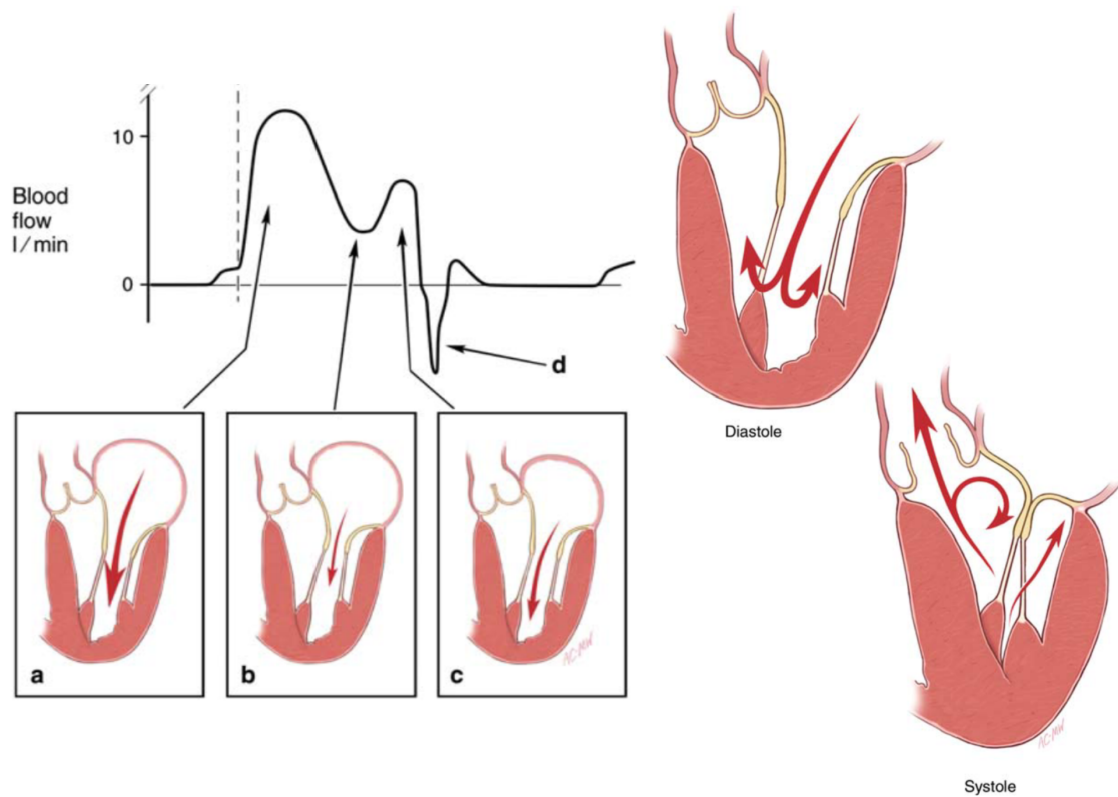


Figure 2.2: Blood flow into the left ventricle during diastole and ejection during systole. The subfigures a, b and c show the three different opening phases of the MV during diastole. The position d in the blood flow graph shows a slight back-flow of a healthy human heart due to a delay in the contraction of the papillary muscles and a billowing of the leaflets towards the left atrium. Figures are adopted from [15].

After the systole, diastole begins again. The pressure in the the LV decreases due to relaxation. As soon as it falls under the aortic pressure, the aortic valve closes. Subsequently, the pressure drops below the atrial pressure causing the MV to open. This marks the beginning of the filling phase again. [52, 38, 15]

Figure 2.3 shows the so-called Wiggers diagram [4], which summarizes the phenomena previously described by means of the pressure graphs of the a aorta (red line), LA (yellow line) and LV (blue line) for two cardiac cycles. In addition, the points where the different valves open and close are marked. It can be observed, that at the beginning of the systole, the Mitral valve between LA and LV closes, and subsequently the aortic valve opens, enabling the ejection towards the body circulation. At the end of the systole the aortic valve closes and shortly after the MV opens passively, enabling the blood flow from the LA to the LV.

2.1. Mitral Regurgitation

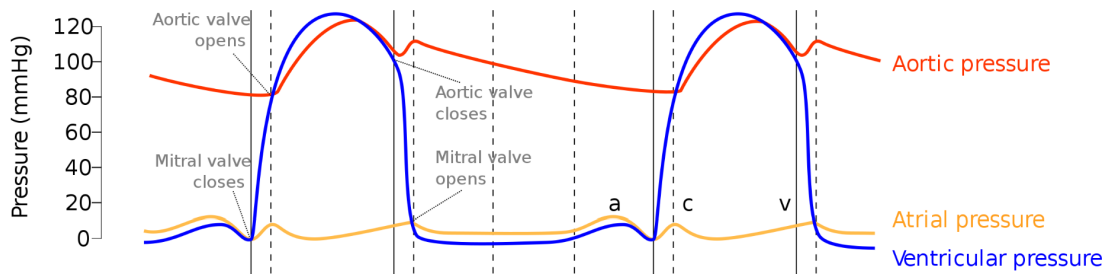
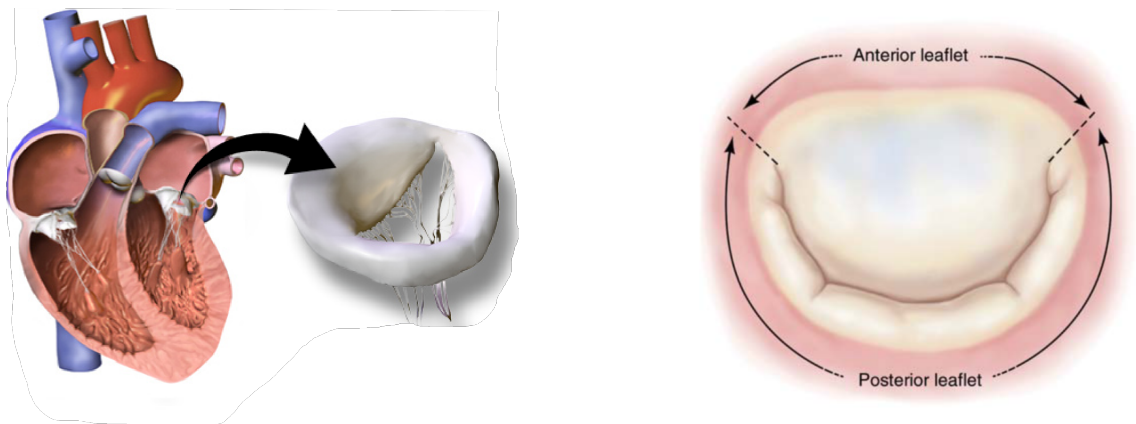


Figure 2.3: Extract of a Wiggers diagram as in [4]. It shows the pressure graphs in the aorta, the left atrium and the left ventricle for two cardiac cycles. Additionally, the points where the aortic valve and the Mitral valve open and close are marked.

Figure 2.4a illustrates the three-dimensional appearance of the MV between the LA and LV. The MV consists of two leaflets, the anterior and posterior leaflets, as shown from above in Figure 2.4b.



(a) Location and 3D shape the Mitral valve, adapted from [62]

(b) Anterior and posterior leaflet of the Mitral valve, adapted from [15]

Figure 2.4: Location and shape of the Mitral valve

The annulus surrounding the leaflets marks their connection to the wall. The chordae tendineae are tissue cords that connect the leaflets to the papillary muscles and are not only supporting the opening of the leaflets, but are also responsible for preventing the leaflets from retracting back into the atrium during the systole. Figure 2.5 provides an overview of Mitral valve anatomy.

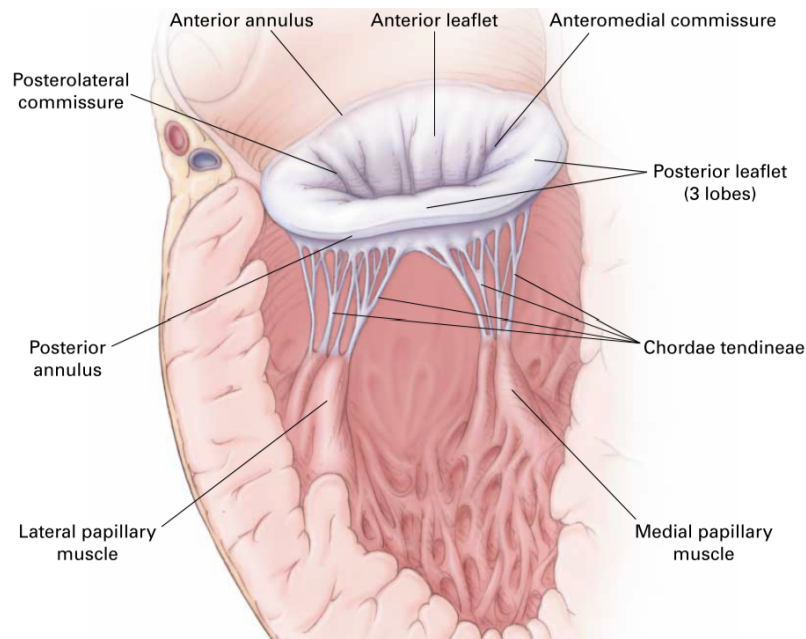


Figure 2.5: Anatomy of the Mitral valve [70]

2.1.2 Pathophysiology and Classification

As previously described, the leaflets of the Mitral valve close due to the pressure gradient between the LA and the LV. In the case of an insufficiency of the MV, leaflets poorly close during the ejection phase. Thus, the contracting LV empties in two directions - partly in direction of the system circulation, where it should go, and partly as a regurgitant jet into the LA, where it should not go.

To maintain cardiac output, the stroke volume and/ or the heart rate must be increased. This volume strain yields hypertrophy and dilatation of the LV, which means the ventricular walls become thick and stiff and tend to grow. This unphysiological growth of the ventricular walls leads to a worsening of their inner blood flow, resulting in a reduced oxygen supply. The heart is weakened and can fail if untreated. In case of severe inefficiencies the cardiac output cannot be maintained. This results in a significant loss of physical performance. The regurgitant jet in the atrium also distorts the heart rhythm increasing the risk of blood clots and strokes. Furthermore, due to the increased pressure in the lungs, fluid can build up there, potentially causing the lungs to fail. [38, 87, 28, 14]

Based on the cause, MR can be subdivided into primary and secondary MR, according to [38, 87, 28, 100].

- **Primary Mitral regurgitation** is caused by degenerative mechanisms. The insufficient closing is caused by deformed or damaged leaflets.
- **Secondary Mitral regurgitation** is a functional error of the Mitral valve. No structural problems with the valve itself exist, but insufficient closing of the leaflets is caused by dilation of the Mitral valve annulus or displacement of papillary muscles. The opening and closing forces are imbalanced.

Furthermore, Carpentier [15] classifies MR based on the leaflet motion, as follows

- **Type 1: Normal leaflet motion:** A central regurgitation jet occurs due to annular dilation or leaflet perforation although the leaflets are moving normally.
- **Type 2: Excessive leaflet motion:** An eccentric jet develops in the LA generated by ruptured papillary muscles or chords, or an elongation of the latter.

- **Type 3: Restricted leaflet motion**

- **3a: Restricted motion in both systole and diastole:** A central or eccentric jet may arise usually caused by a rheumatic heart disease.
- **3b: Restricted motion in systole:** A central or eccentric jet is caused by a dysfunction of the papillary muscles or a dilatation of the LV.

A summary of the above given Carpentier type classification as composed by El Sabbagh et al. [28] is given in Figure 2.6.

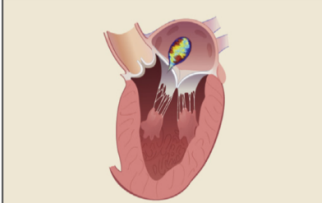
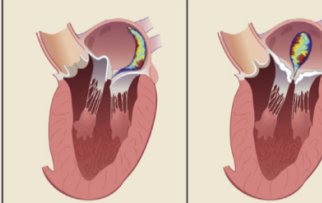
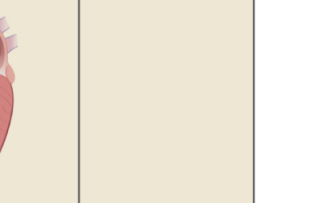
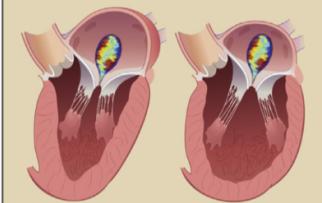
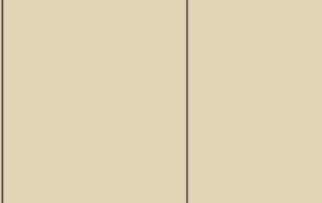
	Carpentier Type I (normal leaflet motion and position)	Carpentier Type II (excess leaflet motion)	Carpentier Type IIIa (restricted leaflet motion in systole and diastole)	Carpentier Type IIIb (restricted leaflet motion in systole)
PRIMARY MR	 <p>Leaflet Perforation Cleft</p>	 <p>Mitral Valve Prolapse</p>	 <p>Rheumatic Valve Disease Mitral Annular Calcification Drug Induced MR</p>	
SECONDARY MR	 <p>Atrial MR</p>	 <p>Nonischemic Cardiomyopathy</p>		 <p>Ischemic Cardiomyopathy</p>

Figure 2.6: Carpentier type classification of Mitral regurgitation adapted from [28].

A more detailed description of the underlying mechanisms of MR can be found in [15]. A definition of the eccentricity of regurgitant jets can be found in [56].

Turbulence, amongst other things, increase the shear forces and mixing of fluid flows [72, 81]. Even though in a healthy heart low turbulence levels are expected in the blood flow, Mitral regurgitation rises the transition to turbulence. On a positive note, turbulence in the heart increases the mixing and washout of the blood. The downside is, that increased shear forces lead to an amplified risk of platelet activation and formation of hemolysis. This means that red blood cells, which are responsible for the oxygen transport in the body, are dissolved and destroyed. [9, 71]

2.1.3 Diagnosis Techniques

The need for an intervention to reconstruct the valve strongly depends on the severity of the disease [70] and therefore, the diagnosis. Contemporary diagnosis techniques for the MR evaluation will be described in the following.

Different medical diagnosis techniques come into consideration. Physical examination detects systolic murmurs connected with MR, but does not allow for accurate assessment of the regurgitation severity [70]. X-ray or magnetic resonance imaging are either too expensive for routine examination or only provide information late in the course of the disease [38, 70]. If MR is suspected, Transesophageal echocardiography (TEE) is the method of

choice, as it is relatively cheap and allows for a evaluation of the severity [87, 70]. TEE is a non-invasive imaging technology, where a ultra sound (US) transducer is inserted into the esophagus. By changing the position and orientation of the transducer the structure and functioning of the heart in different planes can be assessed.

The ultrasound waves, emitted by the transducer, get reflected at the solid structures of the heart and the erythrocytes (red blood cells). The returning echos are translated into images of the heart’s structure including the valves and flow patterns of the blood. Besides using US to create images and identify structures of the heart, color-Doppler and continuous wave Doppler (CW-Doppler) are the most relevant tools for MR evaluation. In the color-Doppler mode the Doppler effect is utilized to measure flow velocities. Flow away from the transducer appears blue, while flow towards the transducers is colored red. [53]

Figure 2.7a shows an exemplary color Doppler image from the measurements conducted in [48]. If the flow velocity exceeds the US sampling rate an effect called alias effect occurs. This velocity is called the Nyquist limit and can be adjusted by the physician. In Figure 2.7a, for instance, blue areas appear in the middle of red colored areas. Clearly, a small patch of flow in the direction of the probe cannot move in the reverse direction. In this way, it is easy to see the occurrence of the alias effect, which can be used to identify the location of maximum velocity. In addition, for MR diagnosis, it is used to visualise the regurgitation jet. [53, 100, 28, 87]

The CW-Doppler mode is used to accurately measure high velocities [53]. Figure 2.7b shows an exemplary course of flow velocity of the regurgitant jet for one heart beat, recorded within the scope of [48].

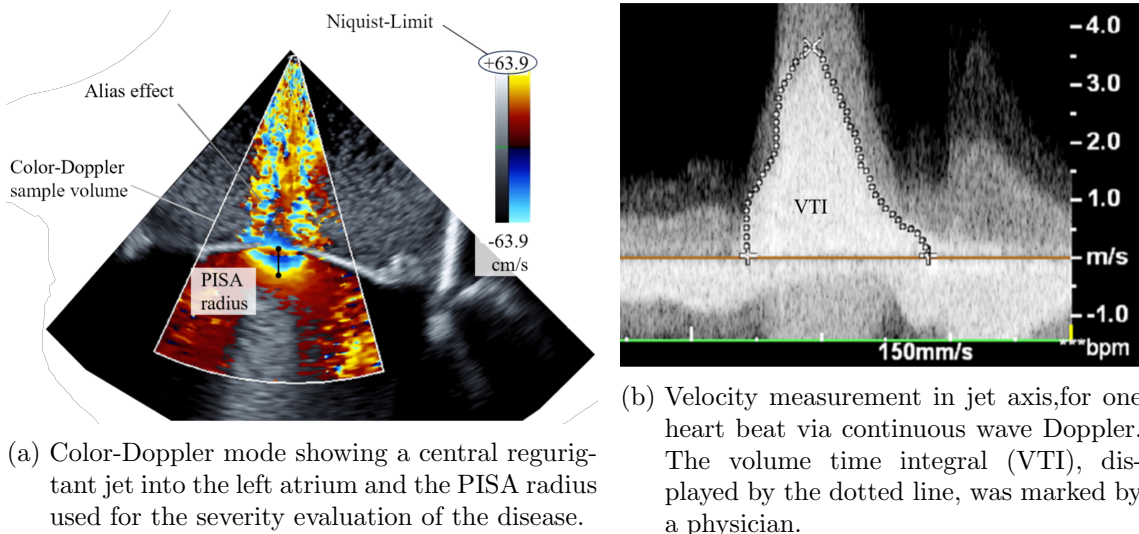


Figure 2.7: Two exemplary images of the ultrasound modes used for Mitral regurgitation diagnosis; images from the measurements conducted by physicians in [48].

Different qualitative, semi-quantitative and quantitative parameters derived from TEE allow for a MR severity grading. [38, 28, 100]

They will be described in the following and are summarized in Table 2.1.

Qualitative Evaluation Methods

Color-Doppler imaging can be used but is not best practice in quantitatively assessing severity of the disease [100, 70]. However, it is the gold standard in qualitative MR assessment.

Besides the morphology of the Mitral valve the five components depicted in Figure 2.8 are used to evaluate MR via color Doppler imaging [100, 28, 38]. These five evaluation methods, based on the guidelines from [100, 28, 38], and [87] are explained in detail in the following.

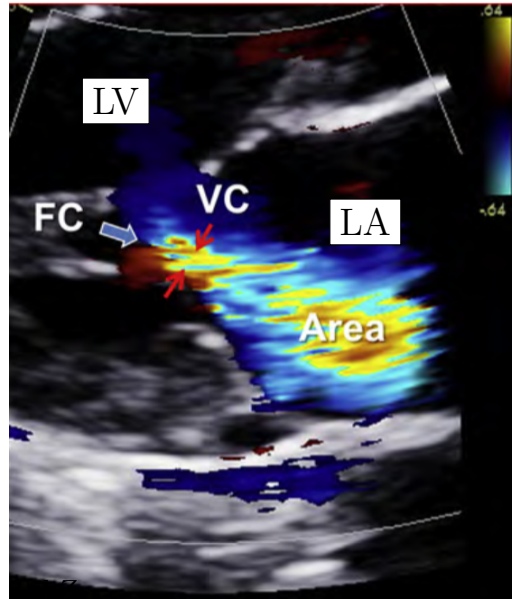


Figure 2.8: Left Ventricle (LV), left Atrium (LA), color jet area (Area), vena contracta (VC) and flow convergence (FC) recovered from a selected color-Doppler image, adapted by adding labels from [100]

The **size of the LA and LV** provide information regarding severity of the MR. In case of normal sized LA and LV severe MR can be excluded.

Visual examination of the **color jet area** is an easy applicable method to detect existence and qualitatively assess severity of MR depending on shape and spatial orientation of the jet area. Obviously, it is not suitable for quantitative evaluation. Further limitations are a dependency of the jet size on fluid mechanical properties of the blood flow (hemodynamics) making it hard to compare between different studies.

The **vena contracta (VC)** marks the narrowest section of the jet as it emerges from the orifice. The VC is a semi-quantitative measure allowing distinction between mild and severe MR. Limitations of this method are a strong dependency on the geometric shape of the orifice (three-dimensional echocardiography solves this problem) and that there is an underestimation in case of multiple regurgitant jets.

The **Flow convergence (FC)** from the center of the body to the regurgitant orifice (proximal) is another qualitative measure based on visual examination. The shape, location and duration of the flow convergence provide information on the severity of the disease and the position of the lesion responsible for the regurgitant jet. Disadvantages of the FC measurement are an underestimation of MR in case of crescent shaped orifices and an overestimation of MR if the jet not only appears during systole (holosystolic) as it is calculated from a single frame.

An overview of the qualitative grading parameters can be found in Table 2.1. In addition, color-Doppler echocardiography may provide information regarding the regurgitation's origination according to the mechanisms listed in Section 2.1.2.

Quantitative Evaluation Methods

A commonly used quantitative evaluation method for MR is the proximal isovelocity surface area (PISA) method, or flow convergence method [38, 100, 28]. This method is based on the conservation of mass, presuming that the flow through the regurgitant orifice must equal the flow through a isovelocity surface. PISA is conducted in the following steps, according to [100].

1. Color-Doppler imaging is performed. The Nyquist limit is adjusted to typically 30 – 40 m/s to determine the aliasing velocity V_a .
2. The distance from the point where V_a occurs to the VC is measured. This is defined as the PISA radius r (Fig. 2.7a). It is assumed, that if regurgitation exists, the blood flow in the LV converges in shape of concentric shells, where velocity increases and surface area decreases towards the orifice. Color flow mapping, via adjusting the Nyquist limit, provides the possibility to determine V_a and its respective surface area.

3. The regurgitant flow rate RFlow [ml] is calculated via

$$\text{RFlow} = 2\pi r^2 \cdot V_a. \quad (2.1)$$

4. CW-Doppler is conducted to determine the velocity time integral (VTI) and the maximum speed (V_{\max}), as in Figure 2.7b. Here, it is assumed, that the PISA radius occurs at the time when regurgitation velocity peaks.
5. The effective regurgitation orifice area (EROA) is calculated via

$$\text{EROA} = \frac{\text{RFlow}}{V_{\max}} \quad (2.2)$$

6. The regurgitant volume (RVol) is calculated via

$$\text{RVol} = \text{EROA} \cdot \text{VTI}. \quad (2.3)$$

Figure 2.9 from Zoghbi et al. [100] provides a schematic representation of the assumptions in connection with the flow convergence method.

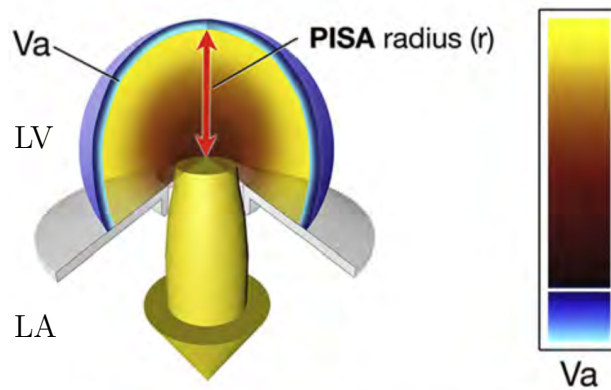


Figure 2.9: Schematic presentation of the flow convergence method and relevant parameters, adapted from [100]. V_a = aliasing velocity, PISA = proximal isovelocity surface area, LV = left ventricle, LA = left atrium.

Based on the qualitative and quantitative parameters obtained from the before mentioned methods, the MR severity is graded, according to Zoghbi et. al. and El Sabbagh et al. [100, 28] (Table 2.1).

Table 2.1: Selection of MR severity grading parameters as presented by [100, 28]

	Mild	Moderate	Severe
Qualitative			
Mitral valve morphology	None or mild leaflet abnormalities (mild thickening, calcifications, prolapse, tenting)	Moderate leaflet abnormality	Severe valve lesions (flail leaflets, ruptured papillary muscles, large perforations, severe tenting, poor leaflet coaptation)
LA and LV size	Usually normal	Normal or slightly dilated	Dilated
Color jet area	Small, central, narrow, short duration	Variable	Large central jet or wall-impinging eccentric jet of variable size
Flow convergence	Not visible, transient or small	Intermediate in size and duration	Large throughout the systole
Semi-quantitative			
VC [cm]	< 0.3	$0.31 - 0.69$	≥ 0.7
Quantitative			
EROA [cm ²]	< 0.20	$0.21 - 0.39$	≥ 0.4
RVol [ml]	< 30	$31 - 59$	≥ 60

Due to the various assumptions made for the flow convergence method, the significance is limited. Especially for non-circular orifices the assumption of flow convergence in shape of concentric shells does not hold true [65, 87, 28]. Furthermore, the method is only reliable for non-eccentric regurgitant jets. This is mainly due to the more complex flow situation in case of eccentric MR. For a reliable quantification the ultrasound beam has to be perfectly aligned with the main flow direction. This is difficult for eccentric regurgitation jets, which are often curved and may change direction during regurgitation [96, 73, 29, 37]. In addition eccentric jets tend to lay alongside the atrial wall and thus cannot entrain fluid on all sides of the jet, violating the assumptions for the flow convergence method [29, 91]. This phenomena is referred to as the "Coanda effect" [33]. The jet loses energy due to the wall impingement and appears to be smaller in TEE, as explained by Duncan et al. [27].

Another potential cause for the tendency of misdiagnosing eccentric MR is, that various causes can lead to it, e.g. ruptured chordae tendineae on one leaflet [15], which are not necessarily discovered by means of the flow convergence method. However, both, non-circular orifices and eccentric jets are common phenomena for MR patients [56, 15, 65, 91]. Furthermore, methods based on TEE are known to systematically underestimated the severity, due to the one-dimensional velocity measurement and are highly dependent on user proficiency. The two primary reasons are that physicians manually set measurement

points, creating a high level of dependence on their experience and subjective assessment, and that the transducer control is challenging. [31, 19, 3]

Incorrect diagnoses, due to errors in connection with the above mentioned methods, can potentially lead to misguided treatment decisions with severe consequence for the patient [99]. This motivates this study to contribute to the diagnosis of MR. By helping to understand the flow characteristics connected with MR, it is aimed to improve current diagnosis techniques. The scope of this thesis is to contribute to the quantification and flow characterisation of MR. Thus, the topics regarding the therapy of MR will be skipped here. Interested readers are encouraged to look in to Carpentier's Reconstructive Valve Surgery [15] and the guidelines for MR management from El Sabbagh et al. [28] or Vahanian et al. [87].

2.2 Fluid Mechanics

In addition to the biological and medical aspects, and for a better understanding of Mitral Regurgitation, it is necessary to have a closer look into a few basics of fluid mechanics. This section will briefly explain the relevant fundamentals of fluid mechanics (Section 2.2.1), as well as provide an overview of free jet streams (Section 2.2.2), which are the main phenomena under investigation. In Section 2.2.3, the concept of vortices will be introduced, as well as different methods for detecting them, which were utilized in this study.

2.2.1 Fundamentals of Fluid Mechanics

In this section the governing equations of fluid dynamics are presented and different relevant simplifications are discussed. Further elaboration can be found, for instance, in [79] and [81]. As blood is a special fluid a few simplification in terms of material properties are deduced before the governing equations will be derived.

Material Properties

For blood, the continuum hypothesis holds true, for as long as the solid blood cells are not separated from the liquid. Please, see [72] or [81] for a summary of the theory underlying the continuum hypothesis. Separation can occur in small arteries or vessels [22], which is beyond the scope of this work. Thus, blood is here treated as a homogeneous suspension of blood plasma and red blood cells.

A fluids internal resistance against a shear force is the dynamic viscosity μ [kg/(m·s)]. For Newtonian fluids the flow behavior follows Newtons law of viscosity (Eq. 2.4), where the viscous shear stress τ is proportional to the shear rate $\dot{\gamma}$.

$$\tau = -\mu \cdot \dot{\gamma} \tag{2.4}$$

In general, human blood is considered a non-Newtonian fluid, as its viscosity decreases under shear strain [5, 11]. Such behavior is called shear-thinning or pseudo-plastic. Figure 2.10 shows the behaviour of blood in comparison to other kind of fluids including Newtonian. Blood consists of ca. 55% plasma, ca. 45% red blood cells and <1% white blood cells [11]. For the blood plasma the assumption of constant viscosity holds true. The red blood cells are responsible for the non-Newtonian behaviour of blood. This is due to a reduction of cellular agglomeration from low to high shear rates, decreasing the viscosity [2, 11].

For quasi-steady flows, e.g. in large arteries, the Newtonian assumption of the bloods shear behavior is valid [30]. This is not the case for the flow in the heart chambers. The pulsation causes the blood flow in the LV to vary between near-zero velocity and peak

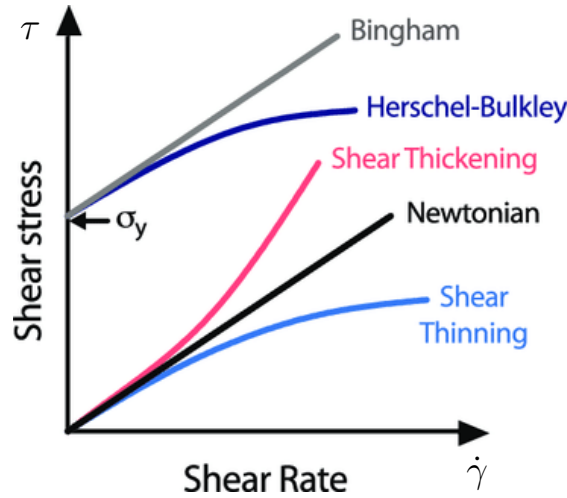


Figure 2.10: Shear stress τ as a function of shear rate $\dot{\gamma}$ for different kind of fluids. Pseudo-plastic shows the behavior of human blood. Adapted from [20].

values, of 6-7 m/s [100]. In addition, sudden changes in direction occur, particularly with MR, leading to an increase in velocity gradients, and hence shear rate.

However, Nordsletten et al. [67] argue that the shear response of blood can be viewed as approximately Newtonian. This is due to the summation of factors such as ventricular size, heart rate, and the invariance of red blood cells, which combine to make the assumption valid. Taking this into consideration, Long et al. [57] suggest that the Newtonian assumption remains applicable when blood is in motion. Nonetheless, non-Newtonian effects may arise during systole or diastole [57]. Out of the above mentioned reasons, blood will be considered as Newtonian in the following.

For a more comprehensive derivation of these assumptions, please refer to [22].

Governing Equations of Fluid Dynamics

The conservation equations required consist of conservation of mass, conservation of momentum and conservation of energy. In the part of the human heart studied, the temperature is assumed to be constant, so the energy equation can be neglected.

The continuity equation expresses the fact that mass is conserved, i.e. per unit volume, the change in mass due to density must equal the difference between mass flowing in and out per unit time. In Cartesian coordinates this yields,

$$\frac{\partial \rho}{\partial t} + \frac{\partial(\rho u_i)}{\partial x_i} = 0 \quad (2.5)$$

The conservation of momentum in index notation is given by

$$\rho \left(\frac{\partial u_i}{\partial t} + u_j \frac{\partial u_i}{\partial x_j} \right) = -\frac{\partial p}{\partial x_i} + \frac{\partial \tau_{ij}}{\partial x_j} + \rho f_i \quad (2.6)$$

According to Wang et al. [89], blood has a compressibility of $3.75 \cdot 10^{-10} \text{m}^2/\text{N}$. For the typical pressure changes during the cardiac cycle (Section 2.1.1), this results in density fluctuations of approximately $5 \cdot 10^{-4}\%$, making compressibility effects negligible [22].

For incompressible fluids, Equation 2.5 reduces to

$$\frac{\partial(u_i)}{\partial x_i} = 0. \quad (2.7)$$

Assuming constant temperature and small height differences in the considered region, in addition to the incompressibility, buoyancy effects can be neglected. Furthermore,

assuming no gravitational acceleration on the fluid, the volume forces f_i in Equation 2.6 reduce to zero.

By applying the aforementioned simplifications to the equation of momentum conservation, the Navier-Stokes equations (NSE) can be derived:

$$\rho \left(\frac{\partial u_i}{\partial t} + u_j \frac{\partial u_i}{\partial x_j} \right) = -\frac{\partial p}{\partial x_i} + \mu \left(\frac{\partial^2 u_i}{\partial x_j \partial x_j} \right) \quad (2.8)$$

The Equations 2.7 and 2.8 fully describe the blood flow in the considered part of the left human heart.

2.2.2 Free Jets

One solution of the NSE (in cylindrical coordinates) is an axisymmetric free jet.

Free jets are flows exiting a nozzle into a free area without the presence of any bounding wall. At the present the outflow is considered to be stationary and the surrounding fluid to be at rest. A free shear layer (or free boundary layer) forms between the fluid at rest and the out-flowing fluid. Due to viscosity and tangential shear forces the surrounding fluid gets accelerated and carried along at the edges of the jet. Thus, the jets volume flux increases linearly in axial direction with the distance from its origin. This effect is called entrainment. In addition, the jet itself gets decelerated, i.e. the mean velocity U_m decreases with x , due to the viscous forces in the mixing layer. [32, 79, 6, 97]

A scheme of the jet diffusion is given in Figure 2.11.

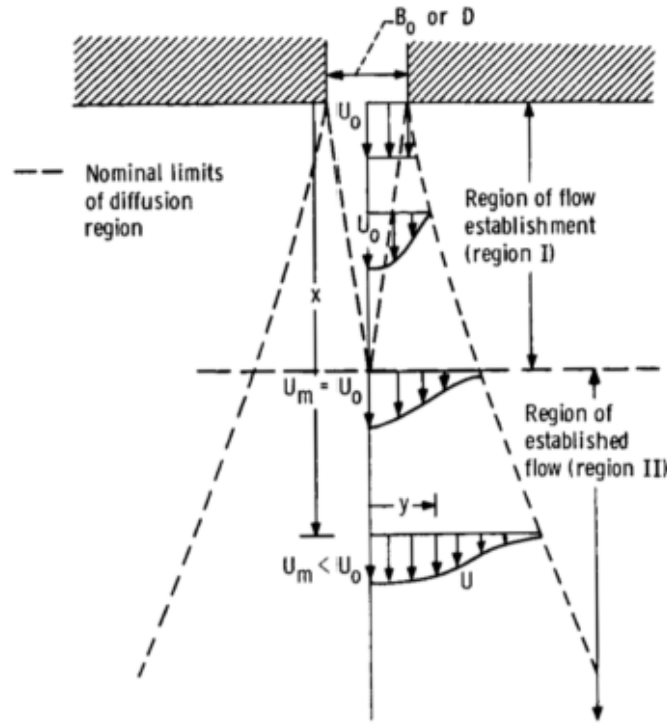


Figure 2.11: Schematic representation of broadening of the jets radial velocity profiles and the decrease of the mean velocity U_m along the axial direction, adopted from [32].

A free jet can be divided into two zones separated by transition zone according to [32] and [6].

At the outlet the fluid leaves the nozzle with an approximately flattened velocity profile with the magnitude U_0 . Behind the outlet, in the region of flow establishment (region I

in Fig. 2.11), also called the near field, a wedge formed core zone is formed. In the core the fluid properties and velocity are approximately constant. On the edges of the core the mixing layer forms. Here, the velocity of the jet decays due to entrainment of surrounding fluid. The width of the mixing layer increases downstream of the jet.

According to [97] and [6] the core length is between two and six orifice diameters D and the transition to the established flow (region II) happens in between $x = 6 - 10 D$.

The region of established flow, also known as far field, begins, where the core is fully dissipated. The radial velocity profiles in region two become self-similar [72]. The velocity decays rapidly in the far field [97].

Typical far field velocity profiles with respect to core velocity U_0 are shown in Figure 2.12. The decrease of the peak velocity and the spreading due to fluid entrainment can be observed.

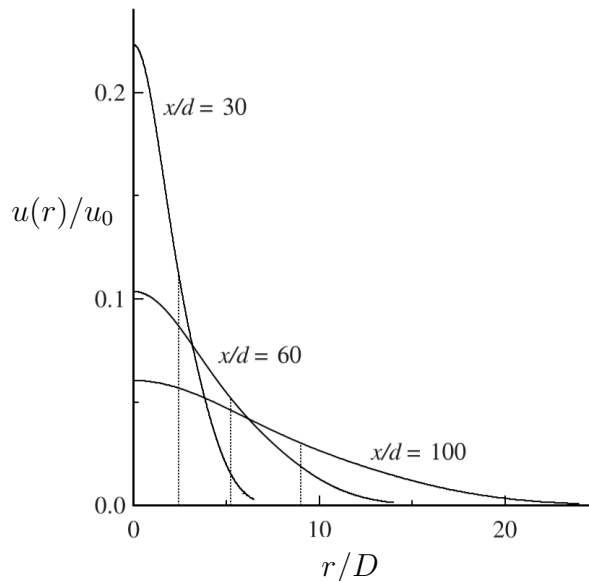


Figure 2.12: Radial profiles of axial velocity of a circular turbulent jet, adapted from [72]. $u(r)$ denotes the the axial velocity component and u_0 the outlet velocity of the jet.

Experimental investigations, given in [43], show that, in the self-similar region, two empirical constants can be observed: S for the spreading rate and B for the velocity decay. The half-width radius $r_{1/2}(x)$ of a jet is defined as the radial distance from the jet center where the velocity magnitude equals half the center line velocity $U_{\text{center}}(x)$ for a given distance x/D from the outlet.

According to [79] and [72], the half-width radius $r_{1/2}$ of the jet is proportional to the distance x with respect to the virtual origin of the jet x_0 , along the center line of the jet. This yields

$$r_{1/2} = S(x - x_0), \quad (2.9)$$

i.e. the jet spreads linearly. For the velocity decay along the center line, the following relationship is observed:

$$\frac{u_{\text{center}}(x)}{u_0} = \frac{B}{(x - x_0)/D} \quad (2.10)$$

The self-similar profile shape, the spreading rate S and the velocity decay constant B are all independent of the Reynolds number for turbulent free jets [72].

To understand the different jet cases observed in this study a few special cases for free jets and underlying fluid mechanical concepts are introduced in the following.

Turbulent Free Jets

A fundamental distinction feature for free jets is the flow regime [32]. For free jet flows the Reynolds number is defined based on the outflow velocity u_0 , the orifice diameter D and the dynamic viscosity ν [72]:

$$\text{Re} = \frac{u_0 \cdot D}{\nu} \quad (2.11)$$

According to [61] the critical Reynolds number for free jets is 1000. The following four main types are observed.

1. Dissipated-laminar jets ($\text{Re} \leq 300$)
2. Fully laminar jets ($300 < \text{Re} < 1000$)
3. Semi-turbulent jets ($1000 < \text{Re} < 3000$)
4. Fully turbulent jets ($\text{Re} \geq 3000$)

The above classification is observed for free jets issuing from circular openings into quiescent surrounding. However, according to [32] a similar zoning appears to be valid for slots with a critical Reynolds number of 2000, based on slot width.

Pulsating Free Jets

Pulsating flows exhibit characteristic distinctions to stationary flows. Those characteristics with focus on cardiovascular systems and pulsating free jets will be summarized in the following based on previous studies.

In fluid mechanics the dimensionless Strouhal number St is commonly used to describe oscillating flows. The St definition is based on the vortex shedding frequency f_v and yields

$$\text{St} = \frac{f_v \cdot L}{u}, \quad (2.12)$$

where L denotes the characteristic length scale and U the flow velocity [82, 90, 49]. For pulsating free jets the orifice diameter D can be used as characteristic length, the pulsation frequency f as f_v and the outlet velocity u_0 as u [39, 41].

Small Strouhal numbers of $\text{St} < 0.05$ can be an indication for heart diseases, as stated by Domenichini et al. [24].

For cardiovascular systems especially, the dimensionless quantity Wo , the so called Womersley number [92], is commonly used to model pulsatile blood flow [44, 78, 88]. It describes the pulsatile flow by relating transient inertial forces to the shear forces, and is defined as

$$\text{Wo}^2 = \frac{2\pi f \cdot L^2}{\nu}. \quad (2.13)$$

Figure 2.13 shows five exemplary radial velocity profiles with the characteristic saddle-backed shape for a Womersley flow in comparison to a parabolic and plug-like profile, calculated by San et. al [78]. In the human heart Wo values ranging from 20 to 30 are observed [68].

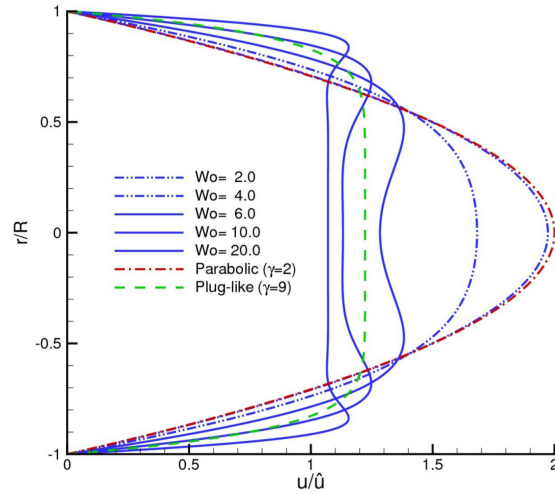


Figure 2.13: Five representative snapshots of the peak velocity profiles of the transient Womersley flow in comparison to a plug-like ($\gamma = 9$) and parabolic profile ($\gamma = 2$); adopted from [78].

Hirata et al. [39] studied the influence of amplitude and frequency for turbulent pulsating free jets by hot-wire anemometry, with similar characteristics like in the present study. An increased mixing was found based on the half-width radius and the total flow rate due to the pulsation. Yadav et al. [94] found a stronger spreading of the jet and shortening of the potential core length, alongside with the increased mixing, due to the pulsation. The increased entrainment of surrounding fluid compared to steady jets was identified as the causation of the observation. Choutapalli et al. [18] found increased entrainment and momentum flux for pulsating free jets alongside a characteristic starting vortex formation. The characteristic vortex formation in pulsed jets was also studied by Ma et al. [58] for similar material properties and flow conditions as in the present study. An increased entrainment and a modulation of the potential core and shear layer were found as consequences of the pulsation. The vortex dynamics in conjunction with free jets will be presented in Section 2.2.3.

Influence of the Orifice Characteristic

Factors like the shape of the orifice and its inlet/ outlet characteristic influence a free jet in terms of spreading, radial velocity distribution, axial velocity decay and vortex formation. This will be explained in the following.

In [63] different shapes like triangle, ellipses, stars and rectangles of different aspect ratios were analysed. Hussain et al. [42] studied excited and unexcited elliptical jets in comparison to circular and rectangular jets. Both found an increased entrainment and turbulence level for the non-axisymmetric jets, which increases spreading and velocity decay in the near field.

For high aspect ratios of the orifice Tsuchiya et al. [85], Marsters et al. [60] found saddle-backed lateral velocity profiles near the outlet similar to the ones presented in Figure 2.13. Saddle-backed lateral velocity profiles are as well found for turbulent plane jets depending on the inlet geometry and aspect ratio of the orifice by Deo et al. [23]. In summary, it is stated, that for longer inlet lengths compared to the orifice size, the velocity profiles tend towards a top-hat shaped profile, while for shorter inlet lengths the saddle-backed shape is more distinct.

Another influence factor on the outlet velocity profiles is provided by Quinn et al. [74]

and Vorous et al. [1]. For sharp edges of the outlet orifice saddle-backed velocity profiles are observed. This phenomena is known as the vena contracta effect. Streamlines are unable to change direction abruptly, resulting in a "contraction" of the flow slightly further downstream of the orifice [74, 50].

Jeffers et al. [45] experimentally found saddle-backed lateral outlet velocity profiles as well for circular openings for wall-impinging jets. Their results were additionally backed up by numerical investigation.

Figure 2.14 shows exemplary saddle-backed outlet velocity profiles for the different cases introduced above. Experimental results observed for large aspect ratio orifices are shown in Figure 2.14a and Figure 2.14b. Figure 2.14c shows the outlet velocity profiles found by [45] for different Reynolds numbers of wall-impinging jets and Figure 2.14d the results found by [74] for sharp-edged orifices.

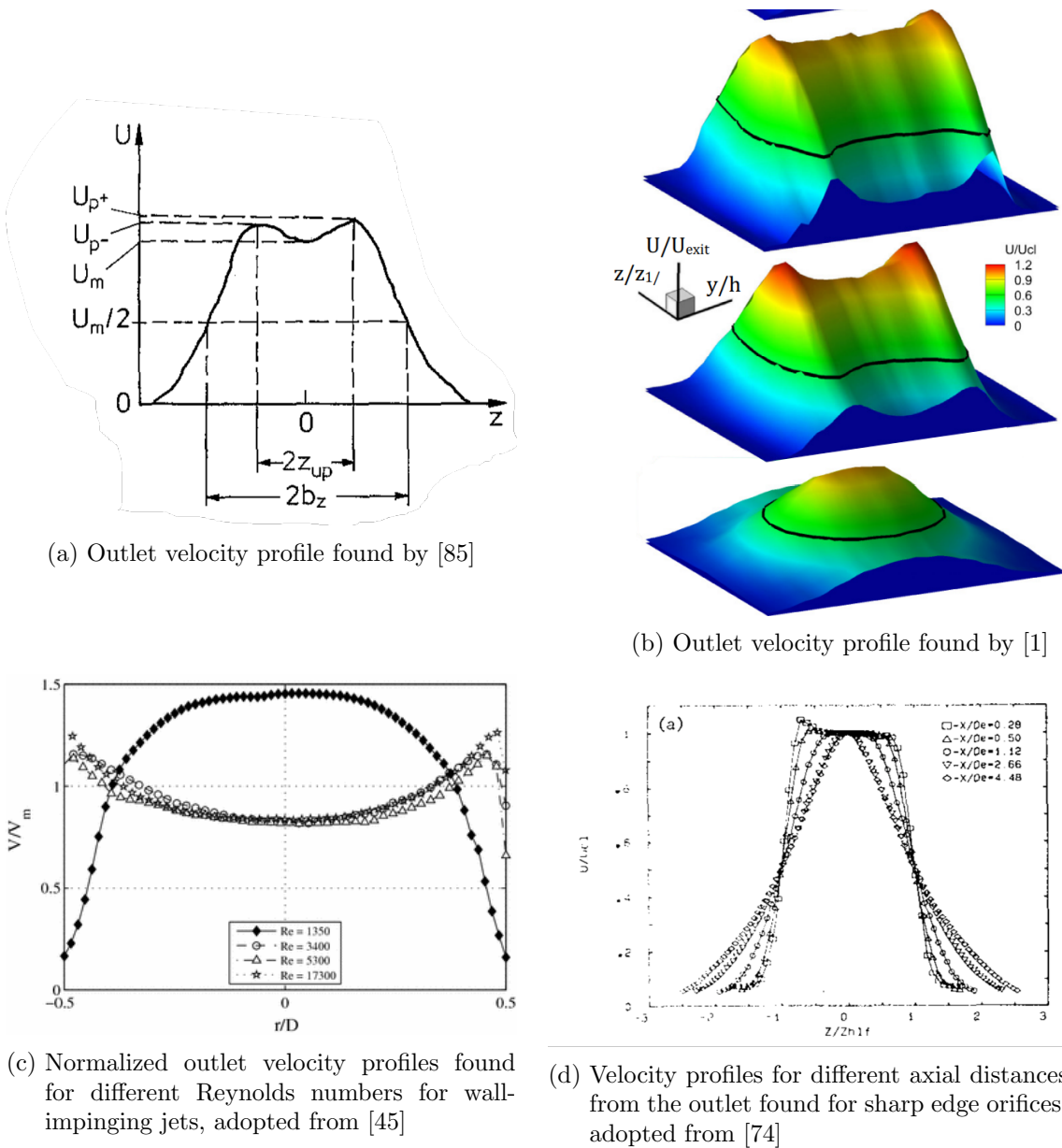


Figure 2.14: Saddle-backed outlet velocity profiles for different free jet cases observed by [85], [1], [45] and [74]

In terms of axial velocity development, [23] found that for short inlet lengths compared to the orifice height, the maximum center line velocity is reached at axial distance of approximately two times the orifice height, and not directly at the outlet. The black dots in Figure 2.15 mark a thin orifice plate with nearly zero inlet length. Quinn et al. [74] found similar results for thin plates with rectangular orifices.

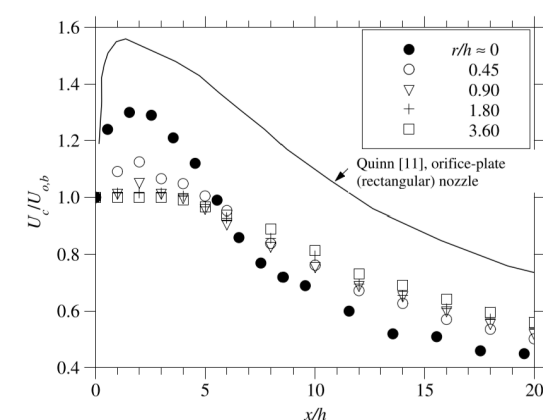


Figure 2.15: Axial development of the center line velocity for different inlet lengths compared to the orifice size, adopted from [23]. The black dots mark a thin orifice plate with with nearly zero inlet length.

2.2.3 Vortex Dynamics

In the human heart the vortex formation process is the dominant flow characteristic [22]. In terms of MR, the usual flow is highly disturbed by the back flowing jet and the vortices coming along with it. Detection and quantification of vortices in conjunction with the regurgitation jet therefore are of major interest. In the following, the basic equations of vortex dynamics will be introduced and the two vortex detection criteria utilized in this study presented.

The following derivations of fundamental equations are based on Wu et al. [93].

Considering the rate of change of a material line element $d\mathbf{x}$ for a fixed particle, yields

$$\frac{D}{Dt}(d\mathbf{x}) = d\mathbf{x}\nabla\mathbf{u} = d\mathbf{u}. \quad (2.14)$$

The rate of change thus equals the velocity difference $d\mathbf{u}$ at the two ends of the line element. The velocity gradient $\nabla\mathbf{u} = \partial u_i / \partial x_j$ can be divided into a symmetric and asymmetric part as follows:

$$\frac{\partial u_i}{\partial x_j} = D_{ij} + \Omega_{ij}. \quad (2.15)$$

D_{ij} describes the strain-rate tensor,

$$D_{ij} = \frac{1}{2} \left(\frac{\partial u_i}{\partial x_j} + \frac{\partial u_j}{\partial x_i} \right) \quad (2.16)$$

and Ω_{ij} the vorticity (or spin) tensor,

$$\Omega_{ij} = \frac{1}{2} \left(\frac{\partial u_i}{\partial x_j} - \frac{\partial u_j}{\partial x_i} \right) \quad (2.17)$$

with $D_{ij} = \vartheta$ and $\epsilon_{ijk}\Omega_{jk} = \omega_i$. The strain-rate tensor D_{ij} accounts for the amount of local folding and stretching, while Ω_{jk} measures the rotation of a fluid element. Furthermore, the vorticity ω can then be defined as

$$\omega_i = \epsilon_{ijk} \frac{\partial u_k}{\partial x_j}, \quad (2.18)$$

which is a basic concept of the vortex dynamics. If the curl is taken from the NSE for an incompressible, Newtonian fluid with conservative volume forces (Eq. 2.8) the vorticity transport equation (Eq. 2.19) can be derived. Thereto, a few vector identities are useful, as for instance described in Wu et al. [93].

$$\frac{D\omega_i}{Dt} = \frac{\partial \omega_i}{\partial t} + u_j \frac{\partial \omega_i}{\partial x_j} = \omega_j \frac{\partial u_i}{\partial x_j} + \frac{\partial^2 \omega_i}{\partial x_j \partial x_j} \quad (2.19)$$

Free Jet Vortex Dynamics

In terms of vortex dynamics two main phenomena occur with free jets. First, when the jet is ejected from the orifice, a leading vortex (or starting vortex) is generated [8, 6, 16, 58]. Second, in the shear layer between the moving fluid of the jet and the nearly at-rest surrounding fluid Kelvin-Helmholtz instabilities can be found [6, 16]. This occurs as follows: Small disturbances in the shear layer generate waves. The fluid has to move faster on the wave peaks and valleys causing a pressure gradient (Bernoulli). Thus, the wave amplitudes tend to grow and eventually roll up to vortices due to the different velocities in the shear layer. [7, 26, 69, 21]

Figure 2.16 schematically displays the process of Kelvin-Helmholtz instabilities.

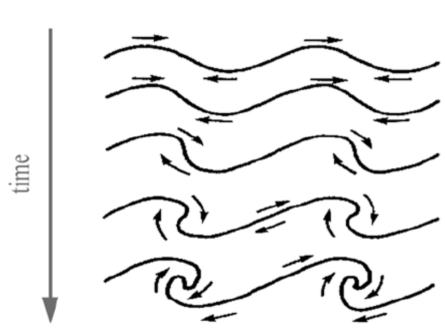


Figure 2.16: Schematic representation of the chronological vortex roll-up in a Kelvin-Helmholtz instability, adapted from [35].

If a vortex exceeds a critical vortex diameter it decays into turbulences [64, 16, 6, 21, 36]. Figure 2.17 shows the vortex roll-up and decay for an axisymmetric jet boundary layer.

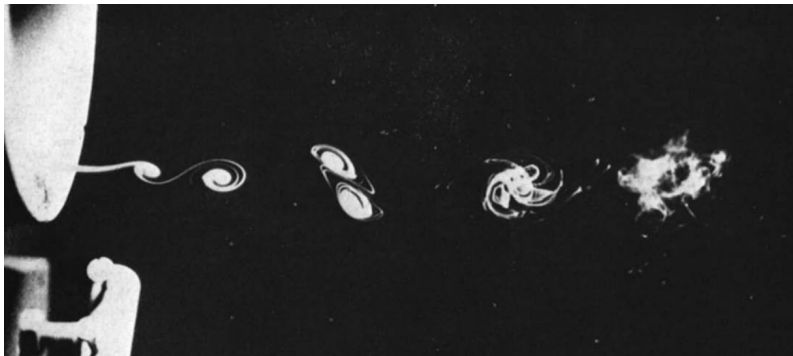


Figure 2.17: Vortex roll-up and decay in an axisymmetric jet boundary layer visualized by smoke, adapted from [64].

Vortex Detection Methods

Although no universal definition of a vortex exists up to now, there are meaningful approaches in indicating vortices in fluid flows [36, 54]. To do so, two detection criteria will be used in this study. In the following the theoretical background of the criteria will be provided.

The Q -criterion is based on the velocity gradient tensor and detects vortices based on the motion of a fluid element, i.e. if the rotation of a fluid element (Eq. 2.17) exceeds the dilatation (Eq. 2.16) a vortex is indicated. Mathematically, Hunt et al. [40] define Q based on the second invariant of the velocity gradient.

$$Q = \frac{\partial u_i}{\partial x_j} \frac{\partial u_j}{\partial x_i} \quad (2.20)$$

Using the separation of the velocity gradient tensor (Eq. 2.15), vortices are indicated for

$$Q = \Omega_{ij}\Omega_{ij} - D_{ij}D_{ij} > 0. \quad (2.21)$$

Further adjustments to the Q -criterion have been introduced by Chong et al. [17] and Zhou et al. [98] increasing its robustness and applicability. A downside of the Q -criterion and related approaches, is that it is gradient-based, which can be problematic for experimental data [54].

The Γ_1 -criterion, as introduced by Graftieaux et al. [34], identifies vortices by using the streamline topography. Thus, it eliminates the need for velocity gradients. A vortex core is identified based on the average angle of the local velocity field relative to a reference point. A point in a velocity vector field belongs to a vortex core, if the magnitude of $\sin(\Theta_M)$ on average approximately equals 1. The sign of Γ_1 denotes the sense of rotation of the vortex. [54]

Γ_1 is calculated as follows:

$$\Gamma_1(P) = \frac{1}{S} \int_{M \in S} \sin(\Theta_M) dS \quad (2.22)$$

Figure 2.18 schematically shows the geometrical relations used for the calculation.

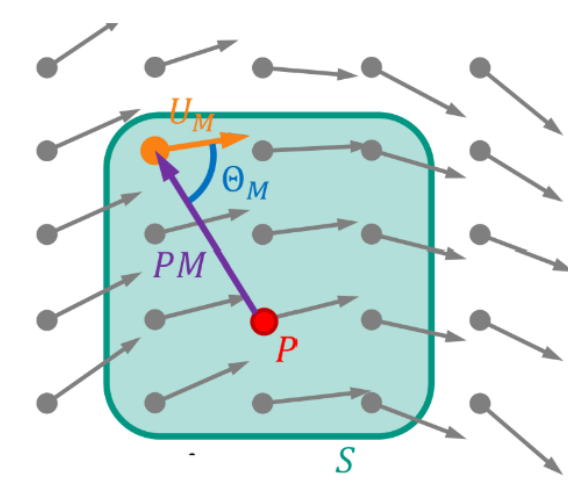


Figure 2.18: Schematic representation of the angle Θ_M of the local velocity field S relative to a reference point P , as used for the calculation of the Γ_1 -criterion [54]. U_M denotes an exemplary velocity vector in the flow field and PM the vector connecting vector with the reference point P .

Usually Γ_1 performs better than Q on experimental data as no gradients are used, but the computational costs are higher [54].

Both, the Q - and Γ_1 -criterion belong to the Eulerian approaches, as they evaluate the flow based on instantaneous velocity information. The downside of Eulerian approaches is, that it is impossible to draw conclusions regarding the development of the flow over time or identify cause-effect relations between the vortical structures detected [54, 22].

An approach eliminating those disadvantages would be the evaluation of the so called Finite Time Lyapunov Exponent (FTLE), which belongs to the Lagrangian approaches. Unfortunately, performing FTLE exceeds the time limitations of this thesis. FTLE evaluations for pulsatile free jets can for example be found in the publication of Ma et al. [58]. Regarding the hemodynamics, FTLE can be found in the PhD thesis of Daub [22], applied for numerical studies of the hemodynamics near the MV.

2.3 Particle Image Velocimetry

Particle image velocimetry (PIV) is a non-intrusive measurement technique that offers immediate velocity information for the entire flow field within the measurement zone. The succeeding PIV theory is derived from [84] and [75].

The working principle of PIV is based on measuring the correlated displacement of a particle ensembles in a certain observation plane. The added tracer particles are made visible via a thin light sheet generated by a pulsating laser. The light scattered by the particles is recorded onto subsequent images by means of a digital camera. Via cross-correlation of the recorded particle-images the displacement of the particles between two subsequent images can be recovered. Hence, the velocity of the flow is calculated by dividing through the optical magnification factor and the time delay between two successive light pulses.

In contrary to single point methods like hot wire anemometry (HWA) or laser Doppler anemometry (LDA), PIV is able to recover a two dimensional velocity vector field. The recovery of instantaneous flow fields enables the derivation of related properties like the instantaneous velocity gradient tensor and identification of coherent flow structures or topological bifurcations.

2.3.1 Experimental Setup for PIV

The experimental setup for PIV experiment consists of three main components: the particle supply, the particle illumination and the the particle imaging. A schematic PIV setup is given in Figure 2.19.

Particle supply: The upstream added tracer particles must be adequately small ensuring they do not influence the flows fluid mechanical properties and perfectly follow the flow. Furthermore, to facilitate high quality PIV recordings and thus, a reliable quantitative evaluation, a medium particle density and homogeneous distribution of particles in the flow is essential.

Particle illumination: The duration of illumination needs to be short ensuring that the distance travelled by particle-images during illumination is significantly smaller than the size of the particle-image itself. Otherwise motion blur occurs and streaks are visible on the recording rather than dots.

In addition, the intensity of the light source must be high enough so that light scattered by particles is detectable with a digital camera. Double-head Nd:YAG lasers with a wave length of 532 nm, pulse energies between 10 mJ and 1 J and a pulse duration of 5 – 15 ns meet those requirements and are therefore commonly used in PIV experiments.

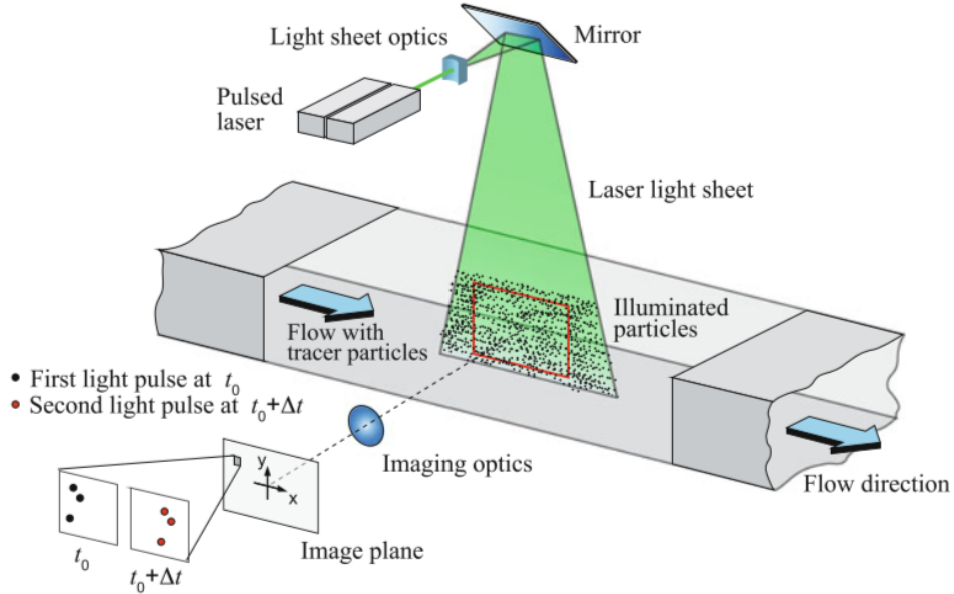


Figure 2.19: Experimental setup for planar 2C-2D PIV measurements: Tracer particles are illuminated by a laser light sheet and recorded by a high-speed camera. Via the displacement of particle images and the time delay between two subsequent images the velocity field of the flow is determined. Adopted from [75].

The laser beam with circular cross-section is transformed into a thin light sheet by a combination of cylindrical and spherical lenses.

Particle imaging: When recording small particles the effect of diffraction limited imaging, referring to the theoretical limit of resolution of an optical system, needs to be taken in to account. When light passes through a circular aperture, like in a camera, it gets refracted and interferes in such way, that a circular pattern of alternating bright and dark rings forms, describing the point spread function of an ideal optical system. The central maximum of this intensity function is called Airy disc and the rings around the peak Airy rings. For a given imaging configuration, the diameter of the Airy disk d_{diff} represents the smallest possible particle image that can be obtained. However, this minimal diameter is only relevant for PIV if very small particles are recorded at small magnifications. For larger particles/ larger magnifications the effects of geometric imaging become more dominant.

The image of a particle is the convolution of the point spread function with the geometric image of the particle. Considering a perfect lens and the point spread function approximated by the Airy function, the particle image diameter can be calculated via the following formula

$$d_{\tau} = \sqrt{(Md_p)^2 + d_{\text{diff}}^2} \quad (2.23)$$

where M is the magnification factor, defined as the ration between the distance from the image plane to lens z_0 and the distance from the lens to the object plane Z_0 (see Fig. 2.20).

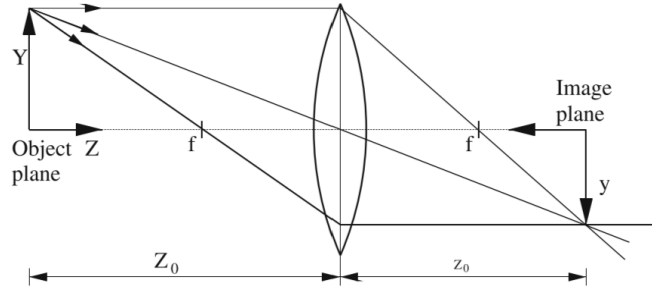


Figure 2.20: Geometric image reconstruction adopted from [75].

Regarding image recording, it is noteworthy that the accuracy of the recorded intensity distribution depends on the image depth of the camera sensor, typically between 8- and 16-bit since each pixel has a digital signal.

Different recording techniques exist in PIV. For this study, the Double-frame/ single exposure technique has been chosen since it is the method of choice as per Raffel [75] and is commonly used nowadays. In this technique, a separate image is captured for each of the two successive laser pulses. Therefore, it inherently preserves the temporal order of images and hence, information on the direction of displacement.

To recover velocity information in physical coordinates (rather than pixel coordinates), calibration must be performed before evaluation.

2.3.2 Evaluation of PIV Recordings

At the beginning of evaluation, which is schematically depicted in Figure 2.21, PIV recordings are divided into so-called interrogation areas.

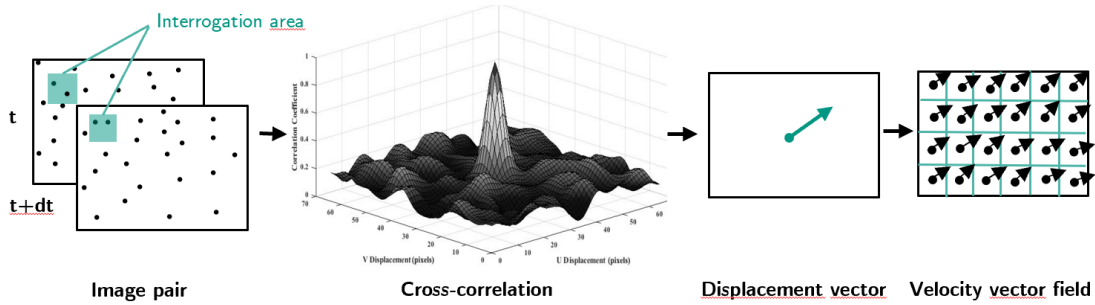


Figure 2.21: Schematic representation of PIV evaluation procedure

For the double-frame/ single exposure method, a cross-correlation algorithm is used to extract the velocity information. For the mathematical application of the cross-correlation algorithm, it is assumed, that the displacement D is constant for all particles in one interrogation area. Hence, the particle location \mathbf{X}'_i in the second image at $t' = t + \Delta t$ for a 2D recording is given by

$$\mathbf{X}'_i = \mathbf{X}_i + \mathbf{D} = \begin{pmatrix} X_i + D_X \\ Y_i + D_Y \end{pmatrix}. \quad (2.24)$$

Assuming that particles are located close to the optical axes, the perspective projection simplifies to

$$\mathbf{d} = \begin{pmatrix} MD_X \\ MD_Y \end{pmatrix}, \quad (2.25)$$

where d represents the particle image displacement in the image plane. Skipping a few mathematical transformations, Raffel [75] describes in detail, the cross-correlation function yields

$$R_{II}(s, \mathbf{\Gamma}, \mathbf{D}) = \frac{1}{a_I} \sum_{i,j} V_0(\mathbf{X}_i) V_0(\mathbf{X}_i + \mathbf{D}) \int_{a_I} \tau(x - x_i) \tau(x - x_j + s - d) dx. \quad (2.26)$$

s is the separation vector, $\mathbf{\Gamma}$ the particle ensemble, a_I the analysed field, $V_0(\mathbf{X}_i)$ the transfer function for the light intensity and τ the point spread function.

The $i \neq j$ terms represent the correlation of different particles in the two images obtained from the successive exposures and thus randomly distributed noise. These terms can be further distinguished into $R_C(s, \mathbf{\Gamma}, \mathbf{D})$, which accounts for the convolution of the mean light intensities, and $R_F(s, \mathbf{\Gamma}, \mathbf{D})$, which is the fluctuating noise component.

The $i = j$ terms represent the correlation of particle-images from the first exposure with particle-images from the second exposure ($R_D(s, \mathbf{\Gamma}, \mathbf{D})$).

Following this distinction, the correlation can be decomposed into three parts:

$$R_{II}(s, \mathbf{\Gamma}, \mathbf{D}) = R_C(s, \mathbf{\Gamma}, \mathbf{D}) + R_F(s, \mathbf{\Gamma}, \mathbf{D}) + R_D(s, \mathbf{\Gamma}, \mathbf{D}). \quad (2.27)$$

The displacement correlation peak reaches its maximum for $s = d$, which represents the average in-plane displacement for a given particle distribution in a flow. Thereby, the velocity components U and V can be calculated using the known time interval between exposures (pulse delay).

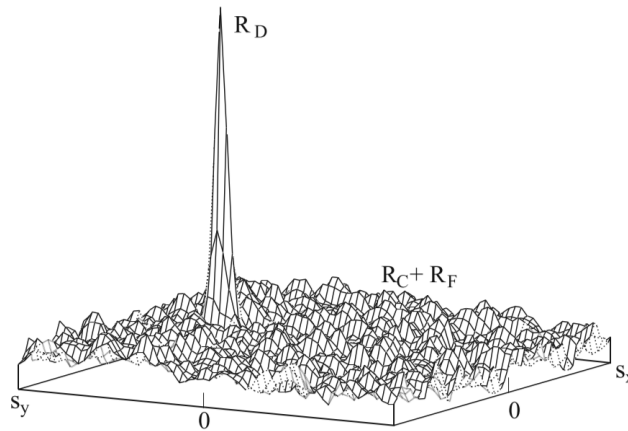


Figure 2.22: Composition of peaks in the cross-correlation function, adopted from [75]

As the input data is discretized, the correlation values only exist for integral values, resulting in an uncertainty of plus/ minus half a pixel. However, the correlation values are statistical measures, making **sub-pixel accuracy** possible with PIV data. This is done following three steps outlined by Raffel [75]:

1. Scan correlation plane to find the correlation peak R_D .
2. Extract adjoining correlation values.
3. Apply a three-point estimator, generally a Gaussian curve, using three points in each direction to find the peak.

The optimal particle image size was found to be between 2-3 px [75, 84]. If the particle image is too small, an effect called peak locking arises, where a particle is only represented

by one pixel. This only allows for integral multiples of displacement, thus reducing accuracy.

Loss of pairs occurs when the algorithm used to process PIV images fails to accurately correlate particle pairs between consecutive image frames. The primary cause behind this is the large displacement of the particle between the two laser light pulses, which makes accurate tracking impossible. Loss of correlation resulting from a particle moving outside the field of view (FOV) is called in-plane loss, while loss resulting from movement perpendicular to the light sheet is called out-of-plane loss. Other factors that can lead to loss of pairs include noise, blurring or distortion, and particle aggregation or clustering.

To account for the loss of pairs, the evaluation is conducted using a **multi-step window shifting** method, wherein the first evaluation determines the shift by which the window is moved in the second evaluation. In each step the interrogated area is reduced, known as multi-grid interrogation [84, 75].

For the determination of the **optimal time delay** between two images or laser pulses, two different uncertainties have to be taken into account. On the one hand, the absolute position uncertainty remains constant for a given setup. The relative position uncertainty is small for large pulse delays due to the large particle displacement. On the other hand, the estimated path between two particle positions deteriorates with increasing pulse delay due to the finite difference approximation. Figure 2.23 shows this relationship.

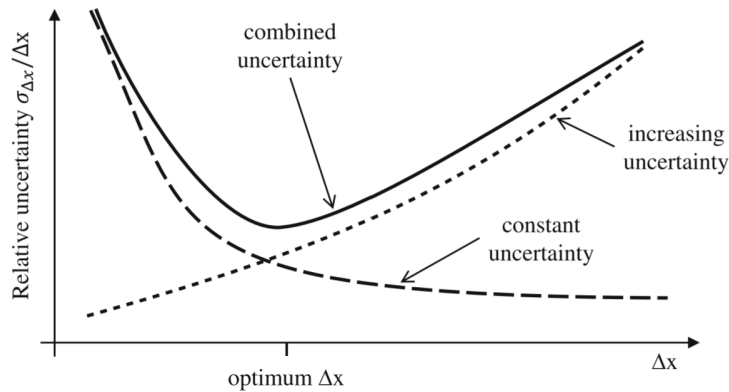


Figure 2.23: Relative uncertainty for PIV measurements depending on pulse delay adopted from [75].

In addition, as the interval between laser pulses increases, the probability of particle loss increases. The best trade-off was found for particle displacements of 6-10 pixels between the two exposures [75].

In terms of **data validation**, false displacement vectors need to be detected and replaced. As visual inspection is not feasible for large PIV measurements, false vectors need to be detected by inspection of the quality of the correlation signal or the local coherence of the vector field, i.e. comparison of each vector with the measured displacement in neighbouring analysis fields. Robust PIV evaluations should consist of less than 5% false vectors [75]. By means of current PIV evaluation software, detected vectors can be replaced by the second highest correlation peak or interpolated from the neighbouring values.

2.4 State of the Art Research

In this section an overview shall be given regarding hitherto existing experimental fluid mechanical studies on MR, that are relevant for the present work.

Billy et al. [12] reconstructed the three-dimensional flow in a two-chamber left heart model by means of 2D PIV in two different sets of perpendicular planes. The main objective was to characterize the three-dimensional flow upstream of a insufficient MV. Furthermore the magnitude of the color Doppler distortion was estimated.

Sonntag et al. [80] performed similar investigations as in this study. The authors conducted PIV experiments on Mitral regurgitation phantoms (MROPs) and compared the results with US and numerical simulations. The main difference to this work is, that only generic orifice shapes were investigated and no pulsatile flow used. As described in Section 2.2.2 pulsation alters the fluid mechanical characteristics significantly.

Providing the three-dimensional velocity information for heart flows, Büsen et al. [13] conducted Stereo PIV measurements in multiple planes in an aorta model. Through this, quasi 3D velocity data could be recovered, yet not in the region of MR.

Jeyhani et al. [46] investigated the flow patterns after a MV repair by means of PIV and color-Doppler US. However, the influence on the flow in the LV was studied, not the regurgitant jet in the LA.

The flow characteristics behind mechanical valves (prostheses) have been studied by Manning et al. [59] and Kini et al. [51]. Both analysed the regurgitant flow in the LV using PIV. However, the flow characteristics after mechanical heart valve replacement significantly differs from the cases in this study. The main difference is, that two jets are emerging from mechanical valves due to the working principle of the prostheses. Hence, the significance of a comparison with this work is limited.

Raghav et al. [76] provide an experimental assessment of PIV measurements of flow fields in connection with heart valve prostheses. The best practice recommendations were used as a guideline for the experimental setup of this study.

Levi et al. [56] systematically analysed the eccentricity of MR jets on patients with indication of wall myocardial infarction. The findings in terms of eccentricity of the jet were used to design the eccentric jet producing MV for this study, which will be further described in the next chapter.

3. Experimental Setup and Procedure

The experimental setup employed for this study consists of two main parts: First, the heart simulator generating the data (3.1) and second, the measurement instrumentation capturing the data (3.2). In the following those two parts will be described and the measurement procedure will be explained in detail.

3.1 The Heart Simulator

The test rig consists of two main components. A 3D printed model of the heart's left part (Form 3B, Formlabs GmbH, Germany; layer thickness 50 μm), and a cardiac piston pump (SuperPump Pulsatile Pump, ViVitro Labs, Inc., Canada).

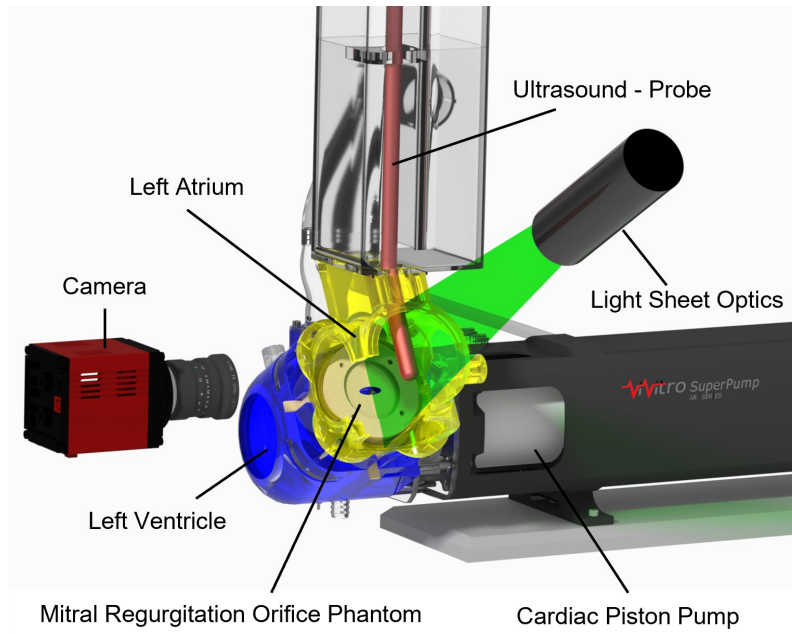


Figure 3.1: Model of the test setup including the heart simulator designed by Karl [48] (submitted), the PIV setup and an ultra sound probe used for the training and studies of physicians.

The 3D model of the left heart was designed by Karl [48] (submitted). The MROPs and patient-specific MV models are inserted between the left atrium (yellow part in Fig. 3.1) and the left ventricle (blue part in Fig. 3.1) instead of a MV.

The MROPs are simulating a closed but insufficient MV, i.e. there are no leaflets that can open and close, but a fixed orifice shape. Thus, the phase of the cardiac cycle investigated is mid-systole, where the ventricle contracts and pushes the blood through the aorta towards the body circulation. For insufficient MVs or the here deployed MROPs, the blood partly flows into the atrium (which is the actual focus of investigation). As the ventricle is manufactured out of rigid material the contraction is simulated by a forward movement of the pump piston. To refill the left ventricle during diastole (where the piston of the pump is moving backwards), the aortic valve is removed enabling a bidirectional flow in the aorta. So, the "cardiac cycle" simulated here is in fact no circulation, but an alternation between regurgitation through the MROP and a refill of the ventricle from the reservoir (grey part in Fig. 3.1) via the aorta. As this study aims to investigate the formation of the regurgitation jet, this is not problematic. Fig. 3.2 shows the assembled artificial heart on the test rig.

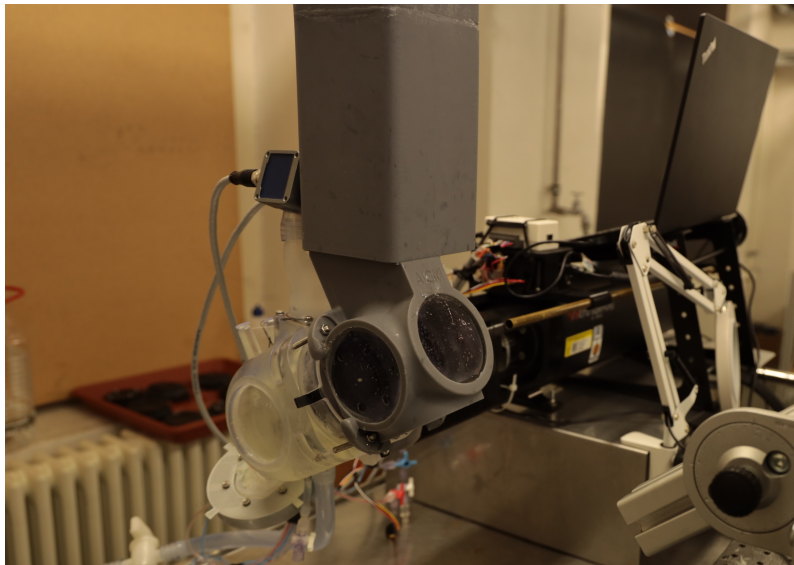


Figure 3.2: The artificial heart on the test rig at ISTM in Karlsruhe, photographed by Robin Leister.

In terms of fluid, 70% water is mixed with 30% glycerol generating a so called blood mimicking fluid with similar fluid mechanical properties to human blood at body temperature.

The cardiac piston pump mimicking a realistic heart beat with a frequency f of 80 bpm is connected to the left ventricle. The left ventricular pressure was set to 120 mmHg for all measurements, by adjusting the stroke volume StrokeVol of the pump. The setting of the StrokeVol determines the piston's travel distance. The output signal of the pump corresponding to the trajectory of the piston is shown for four heart beats with 80 bpm in Figure 3.3. The signal was recorded via a digital I/O device (NI USB-6501, National Instruments Corp., United States of America). Depending on the StrokeVol and heart rate f the course of the graph is scaled maintaining a realistic trajectory.

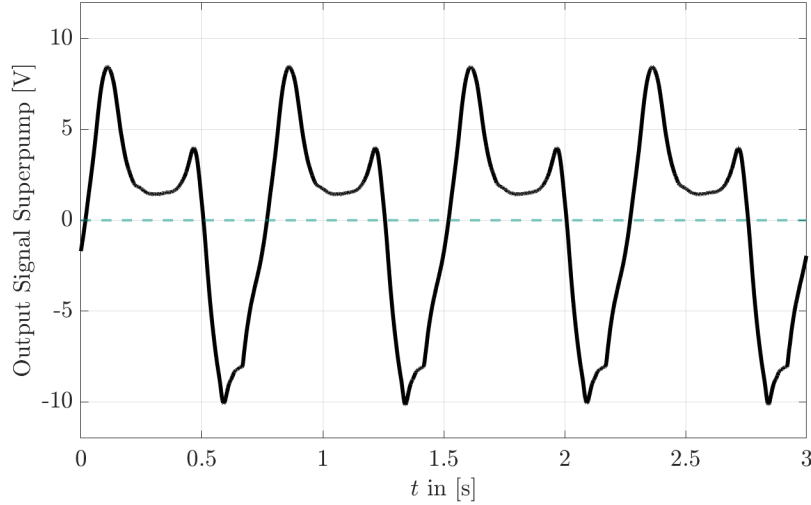


Figure 3.3: Output signal of the ViVitro Labs Superpump for $f = 80$ bpm and StrokeVol = 115 ml; 4 period cycles.

The temporal accuracy of the pump was determined by recording the output signal for a period of 10 min at 80 bpm equalling 800 heart beats, and calculating the temporal drift. Figure 3.4 shows the first 750 ms (periodic time T of one heart beat at $f = 80$ bpm) of the recording as a black solid line and the last 750 ms as a dotted green line.

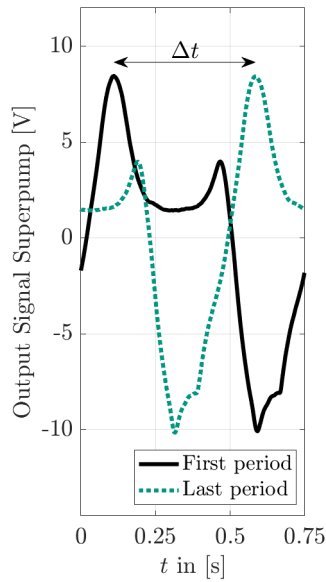


Figure 3.4: First and last period cycle of a 10 minute at $f = 80$ bpm and StrokeVol = 115 ml recording of the ViVitro Labs cardiac piston pump used in the experiments. Δt indicates the the temporal deviation after 800 heart beats.

The temporal drift after 10 minutes of recording is $\Delta t = 474$ ms corresponding to a deviation of 5.925 ms per beat, which equals a temporal inaccuracy of 0.7%. This implicates that for accurate phase-resolved PIV measurements a additional trigger signal for the laser and the camera is necessary.

In the course of this study five different MROPs have been analysed. An approach of increasing complexity was chosen starting with 3 generic orifice shapes, followed by an eccentric jet-producing MROP and a patient-specific MV.

In terms of **generic MROPs** a **pinhole**, a pointed oval (hereafter referred to as **slot**) and a **drop** shaped opening in different dimensions have been manufactured out of a 0.5 mm polyvinyl chloride (PVC) film (Outside Living Industries Deutschland GmbH, Bocholt, Germany) using a laser cutter (Neje Master 2S Plus 30W, LKXSWZQ, optical power 7.5 W, $\lambda = 450$ nm). The pinhole was chosen as the simplest possible MROP, while the slot and drop are more realistic MV defect shapes (according to Jun. Prof. Dr. Sandy Engelhardt, Ruprecht-Karls-Universität Heidelberg). In addition, the slot and drop enable evaluation of asymmetric effects. Three sizes were selected for each geometry to accommodate different MR classifications. Table 3.1 presents the dimensions of the generic MROPs.

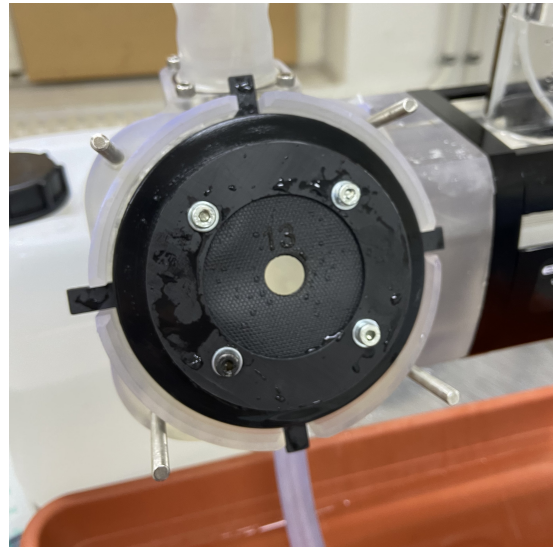
Table 3.1: Sizes of regurgitation phantom orifices.

MROP shape	Width [mm]	Height [mm]	Area [mm ²]
Pinhole S	4.7	-	17.1
Pinhole M	8.7	-	58.8
Pinhole L	12.2	-	116.7
Slot S	3.3	11.1	27.0
Slot M	4.5	14.0	44.8
Slot L	7.3	22.9	115.1
Drop S	4.3	9.7	27.1
Drop M	6.5	13.7	52.1
Drop L	13.1	27.0	169.5

Fig. 3.5a shows the the laser cut films for the three shapes and the sizes S, M and L respectively. To install the MROPs in the heart simulator the film was glued and screwed onto a mount, which was placed between the LV and LA, as depicted in Fig. 3.5b.



(a) Photograph of the polyvinyl chloride film cutted MROPs in the sizes S, M and L.



(b) Installed pinhole M in the heart simulator without the left atrium.

Figure 3.5: Overview of the laser-cutted MROP films and a photograph of the installed pinhole M Mitral regurgitation orifice phantom in the heart simulator.

The sizes of the orifices were determined using a technique called background illuminated imaging. Therefore, the films were digitalized using a scanner. Binarization of the images ensured the area of white pixels corresponded to the orifice area of the MROP. Subsequently, height and width were calculated accordingly.

The **eccentric jet-producing MROP**, also referred to as **EccJet**, was manufactured using 3D printing technology (Form 3B, Formlabs GmbH, Germany; 50 μm layer thickness). Consequently, it differs from the other three geometries in terms of its rigidity. The hole angle was established at 30° in relation to the center line of a straight jet.

Levi et al. [56] define the jet angle as the angle between the annulus plane and the jet center line. Thus, the 30° angle of the EccJet correspond to a jet angle of 60° as per their definition. According to the studies of Levi et al. [56] jets with angles of 46° to 64° towards the annulus plane are considered as eccentric jets. Jet angles exceeding 64° are considered as non-eccentric. Hence, the chosen 30° corresponds to an eccentric jet.

To ensure the correct deflection of flow and the subsequent generation of an eccentric jet, the MROP's thickness was increased to 12 mm, which allows the flow to evolve.

The **patient-specific Mitral valve**, hereafter referred to as **PatSpec**, was developed during a Master's thesis at the Institute for Applied Materials (IAM), KIT, by C. S. Bergt [10]. To accurately reproduce the material, mechanical, and haptic properties, an insufficient MV of a real patient was 3D scanned and fabricated from various materials with the overall goal of reproducing the material, mechanical, and haptic properties of a human MV. Figures 3.6b illustrate the PatSpec mounted onto the heart simulator. Notably, the PatSpec exhibits distinct differences from the generic MROPs, such as its opening and closing during the pump cycle and a non-uniform orifice. Furthermore, the PatSpec includes artificial chordae tendineae, similar to the ones found in natural MVs. By adjusting the tension on the leaflets via the artificial chords (Fig. 3.6c), it is possible to prevent them from swinging beyond the annulus plane into the LA during systole.

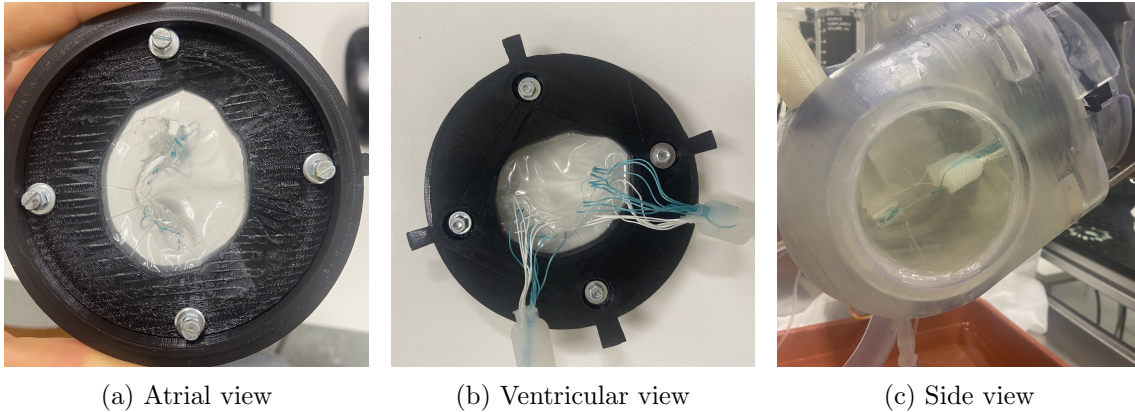


Figure 3.6: Atrial and ventricular view of the patient-specific Mitral valve and a side view into the left ventricle of the heart simulator showing the artificial chords.

3.2 PIV Setup and Procedure

The PIV setup utilized in this study is in general based on the theory described in Chapter 2.3. The PIV method used is called 2D2C, meaning that two velocity components (u and v) in a two-dimensional plane (x - y -plane) are recovered [75]. The laser light sheet generated by the light sheet optics, as described in Chapter 2.3.1, marks the plane in which the velocity components are measured. Figure 3.7 shows the test rig with installed PIV

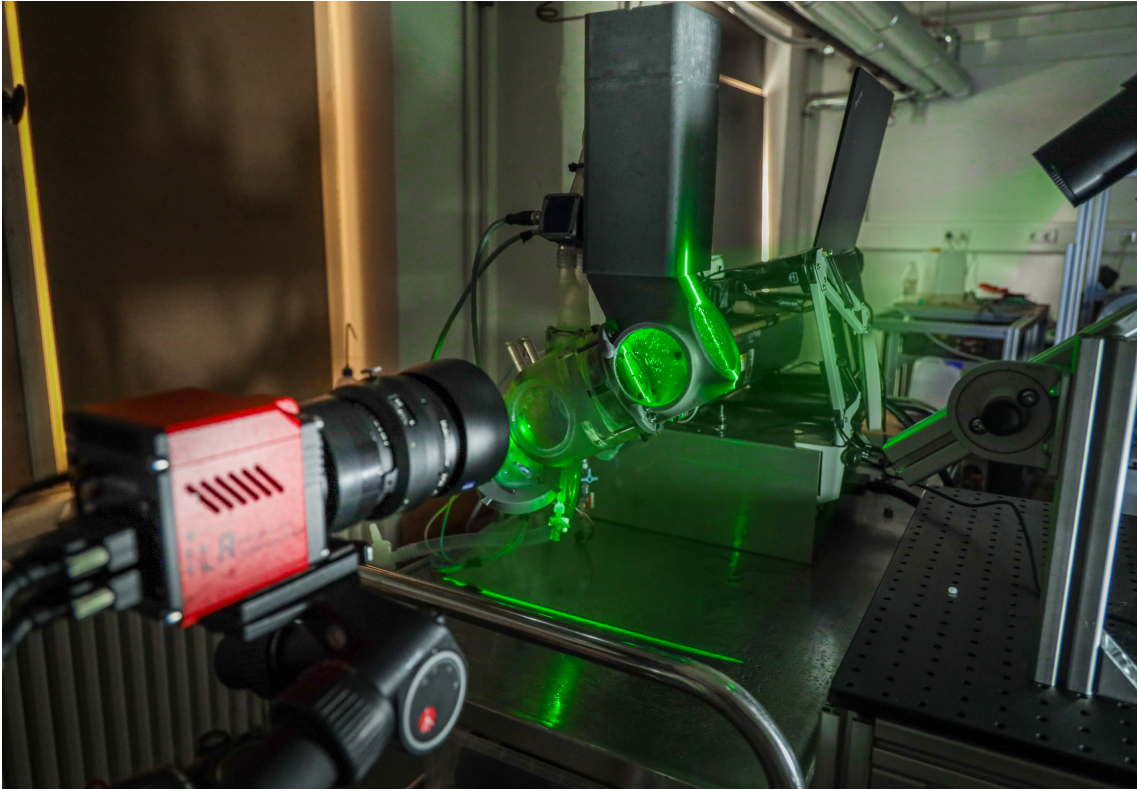


Figure 3.7: The heart simulator with the PIV setup in the ISTM lab, photographed by R. Leister.

measurement setup including the switched-on laser. The optical accesses for the camera and the laser light sheet are given by two atrial windows - one oppositely to the Mitral valve serving as an access for the laser light sheet and one parallel to the light sheet for the camera.

A double-pulsed *Quantel Evergreen* Nd:YAG laser with an energy of 210 mJ and a wavelength of $\lambda = 532$ nm serves as the illumination source. The pulse delay is adjusted between 80 and 100 μs depending on the flow velocity to achieve an optimal particle displacement (as described in Chapter 2.3.2). In terms of seeding, Polyamid particles of $d_p = 20$ μm were added to the blood mimicking fluid corresponding to a particle response time of $\tau_p = 33$ μs . Regarding particle imaging, an *ILA.PIV.sCMOS* camera (16 bit dynamic range, 6.5 μm pixel size) equipped with a 50 mm *Zeiss Makro Planar* lens was used. A magnification of $M = 0.2$ (reproduction scale $s^{xy} = 35.48$ $\mu\text{m}/\text{px}$) results from the described setup with a FOV size of 85×72 mm^2 .

Two methods were used to record the measurement data. First, **phase-averaged** recordings of the flow were conducted. Here, a total of 1000 double-frame images were acquired at a frequency of 15 Hz and then averaged (for each geometry). Those measurement were mainly conducted to calculate the regurgitation volume RVol, which then can be compared to the RVol measured by physicians via TEE. The results of those investigations were incorporated in a to be submitted paper by R. Leister and R. Karl ("Comparison of Transesophageal Echocardiography and Particle Image Velocimetry to quantify Mitral regurgitation in an high-fidelity Environment" [47]) and are not the focus of this thesis. Second, **phase-resolved** measurements were made by dividing the heartbeat into 42 to 55 different phases (depending on the MROP and length of the relevant phases). The signal output from the cardiac piston pump was therefore used as the trigger signal for the laser and the camera and was shifted as desired for each phase. The period during which the regurgitant jet originates and develops (systole) was sampled at time intervals up to 2 μs .

Conversely, during diastole, the irrelevant region was sampled at significantly coarser time steps of around 100 ms. For every phase, 40 image pairs were acquired and then averaged. The measurement protocol is provided in Figure A.1 in Appendix A of this thesis.

For the non-axis-symmetric MROPs, i.e. slot and drop, the laser sheet was traversed in five to nine planes in the z direction. The corresponding offsets for each plane range from 1-3 mm, depending on orifice width. PatSpec MV measurements were taken at seven planes, ranging from $z = -15$ mm to $z = +15$ mm. Although the 2D2C-PIV method only allows the recovery of two-dimensional velocity information, the traversing of the laser sheet provides an understanding of the three-dimensional shape of the jet. This is especially interesting as the Ultra sound measurements carried out by the physicians *in-vivo* only provide one-dimensional velocity information in one plane (2D1C), as shown in Fig. 2.7a.

The software *PIVview* (PIVTEC GmbH, Göttingen, Germany) was employed to post-process the image pairs based on the theory outlined in Chapter 2.3.2. The resultant velocity vector field was subsequently analysed using custom scripts in *MatLab*[®] (MathWorks, United States of America). Spatial analyses were conducted using phase-averaged recordings, if not stated differently. The temporal analysis of the velocity fields was conducted based on phase-resolved measurements. To identify vortices, single image pairs from the phase-resolved measurements were evaluated additionally to detect small-scale effects. The outcomes of this analysis will be presented and discussed in the next chapter.

4. Results and Discussion

The findings outlined in this chapter are categorised into three sections: The section about the generic MROP results (Section 4.1), the section concerning the eccentric jet producing MV (Section 4.2), and the section on the patient-specific Mitral valve (Section 4.3).

For each of the PIV experiments described in Chapter 3 The velocity vector fields generated were analysed and the relevant findings are presented respectively. The analysis adheres to the order of the fluid mechanical theory as outlined in Chapter 2.2:

Each of the following three sections (Section 4.1, Section 4.2, Section 4.3) provides a general description of the flow and an analysis of the temporal parameters of the free jet, as outlined in Chapter 2.2.2. This permits a discussion of the developmental aspects of the regurgitant jet. Additionally, the velocity distribution is spatially analysed, allowing for a discussion of the jet's spreading. Subsequently, for each Mitral regurgitation phantoms and the PatSpec, the results of the vortex detection will be presented, based on the theory outlined in Chapter 2.2.3.

4.1 Generic Mitral Regurgitation Orifice Phantoms

In this chapter, the discussion centres around the results of the PIV experiments conducted on the generic MROPs including the pinhole, the slot, and the drop. Although measurements and analyses have been performed on MROPs of various sizes (please refer to table 3.1 and the measurement protocol A.1), only the most relevant results are presented due to space limitations.

A first overview of the general flow situation for the three MROPs measured via phase-resolved PIV is given in Table 4.1. For the dimensionless quantities, as defined in Chapter 2.2.2, the larger dimension was used as the characteristic length L (diameter D for the pinhole and the height for the slot and drop). Re and St were calculated based on the maximum velocity recovered at the outlet $u_{\text{mag},0,\text{max}}$ and the kinematic viscosity of the blood mimic, $\nu = 3.3 \cdot 10^{-6} \text{ m}^2/\text{s}$.

Table 4.1: Comparison of relevant parameters calculated from the phase-resolved PIV measurements for three orifice shapes.

	Pinhole L	Slot L	Drop L
L in [mm]	12.2	22.9	27
$u_{\text{mag,max}}$ in [m/s]	4.10	4.05	3.73
Re [-]	12382	23435	19818
Wo [-]	19.44	36.49	43.02
St [-]	0.0051	0.0091	0.0149
$ \omega_{\text{max}} $ in [1/s]	3.72	3.52	2.51
$ Q_{\text{max}} $ in [1/s ²]	0.88	0.88	0.49

For the three shapes similar maximum velocity magnitudes ranging from $u_{\text{mag,max}} = 3.73$ m/s to 4.1 m/s are observed. The Reynolds numbers for all MROPs indicate a fully turbulent flow, when the maximum velocity is present at the outlet [61]. However, due to the pulsation, phases with near zero flow velocity are present. This implies phases with laminar flow exist as well. Thus, a transition of laminar to turbulent happens during regurgitation. A vortex dynamical interpretation of the depicted quantities will be given in Section 4.1.3.

4.1.1 Temporal Velocity Distribution

In this section, an overview of the jet development will be given. In addition, the velocity distribution of the regurgitant jet will be displayed for each shape to provide a broad understanding of the flow situation at hand. Following this, the radial profiles of the axial velocity component for different distances from the orifice will be presented. Furthermore, the discussion will include the decrease of axial center line velocity. The velocity graphs found, will be discussed regarding the expected outcomes based on the free jet theory. The radius and half-width radius will be analysed for the pinhole shape, while for the non-axis symmetric orifice shapes (i.e., the slot and drop), an overview of the three-dimensional shape will be provided.

The findings will be compared to the theory on free jets (Chapter 2.2.2). The corresponding hypotheses will be stated before new results are presented and then discussed using the plots generated by means of the developed post-processing methods.

Based on the output signal of the cardiac piston pump, mimicking the human heart beat, the regurgitant jet is expected to emerge and dissipate in each cycle period $T = 0.75$ s = 750 ms.

Figure 4.1 shows the velocity magnitude $u_{\text{mag}} = \sqrt{u^2 + v^2}$ distribution of selected phases of the regurgitant jet development for the pinhole L.

The trigger signal of the cardiac pump is emitted when the regurgitation jet already emerges, i.e. there is already a detectable axial velocity at $t = 0$ s. To visualize the whole sequence of the jet development from emergence to dissipation for the second heart beat are shown below.

To enhance analysis of the experimental data, all velocity matrices were rotated by approximately 30° enabling the visualization of a horizontal jet. White areas, correspond to zero and low, blue areas to medium, and red areas to high velocity magnitudes.

The maximum velocity magnitude $u_{\text{mag,max}}$ for the pinhole L equals 4.1 m/s at $t = 0.770$ s. It is observed that the whole development and dissipation of the jet occurs within approximately 170 ms.

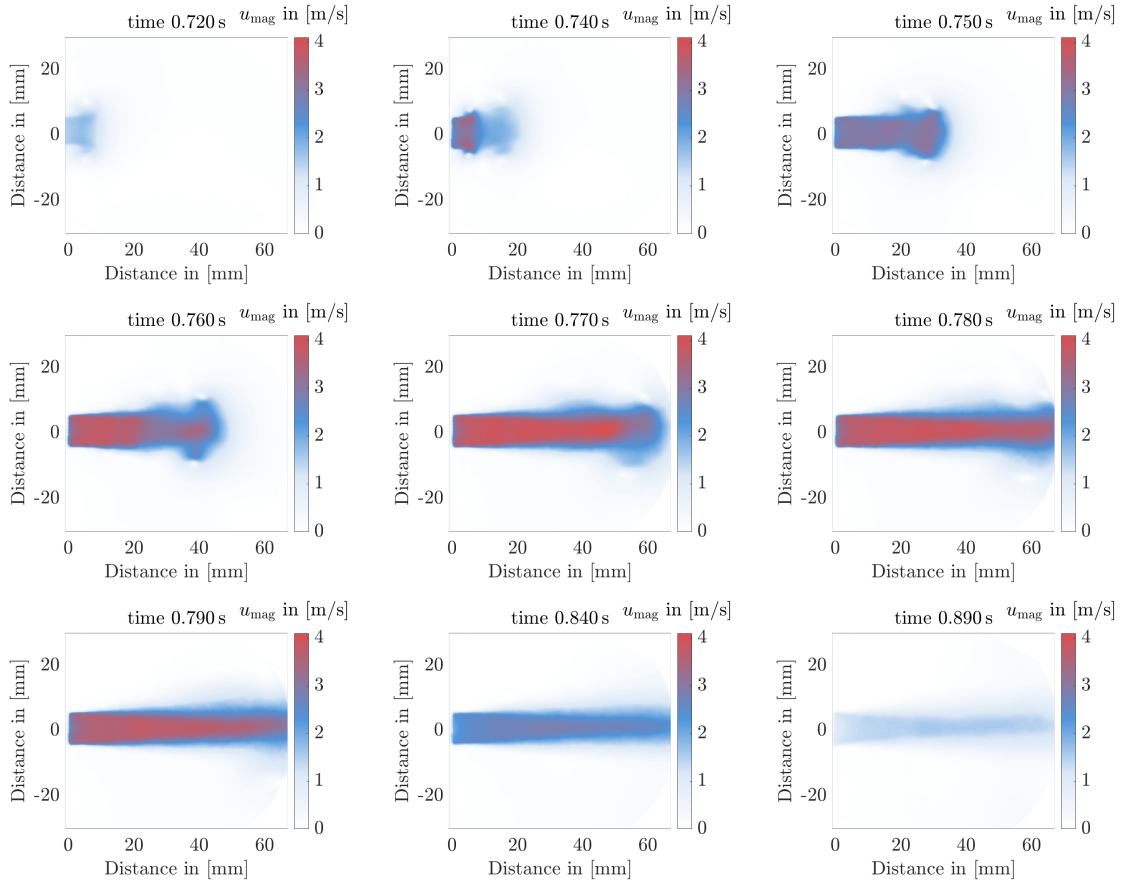


Figure 4.1: Velocity magnitude u_{mag} fields for selected phases during regurgitation; pinhole L Mitral regurgitation orifice phantom.

Figure 4.2 shows the temporal course of the outlet velocity $u_0(y) = u(x/D = 0, y)$ for the pinhole L by means of radial profiles of the axial velocity at $x/D = 0$ for different phases.

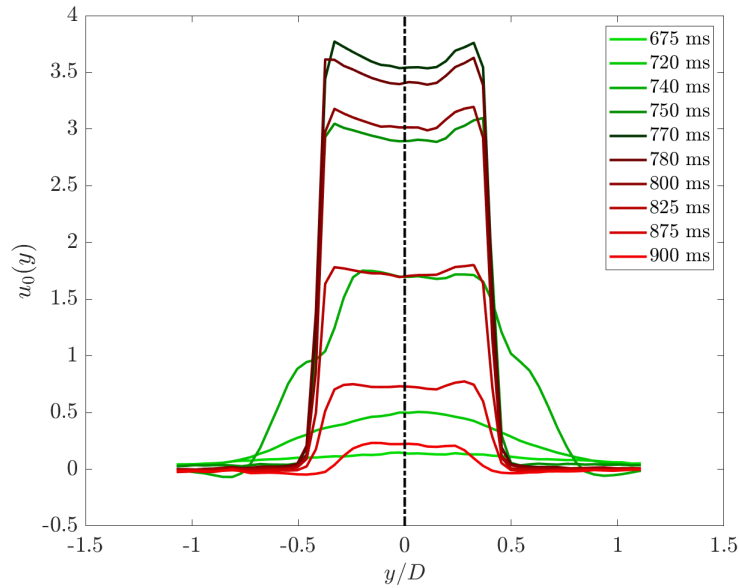


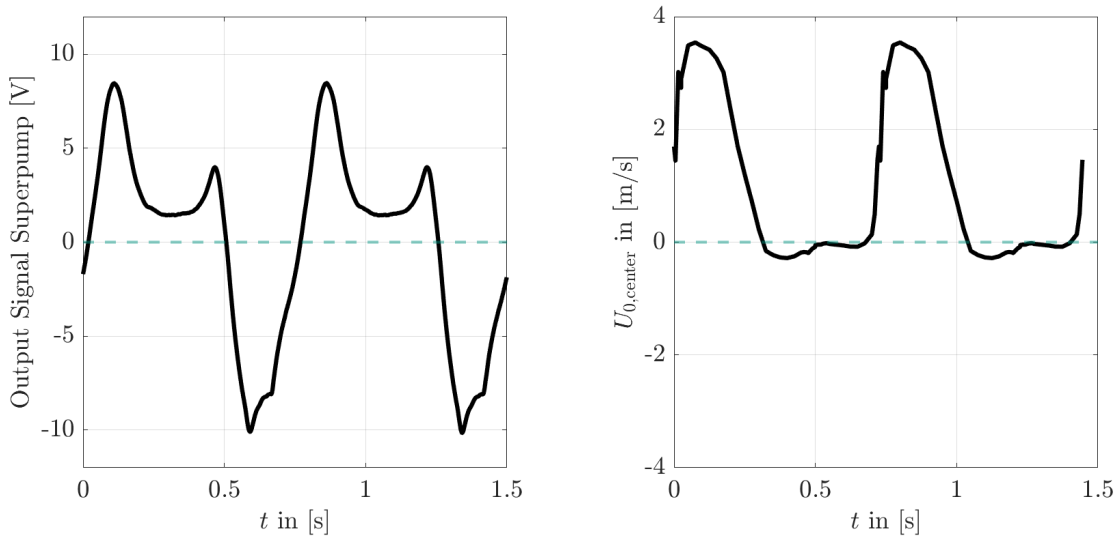
Figure 4.2: Temporal course of the outlet velocity $u_0(y)$ for the Pinhole L. Green lines = phases with increasing velocity, red lines = phases with decreasing velocity.

The green lines are chosen for the phases of increasing velocity, while red marks the velocity decrease phases. The shape of the particular velocity profiles will be discussed in further detail later on (see Section 4.1.2).

The graph in Figure 4.3b shows the center line velocity of the regurgitant jet at the outlet ($u_{0,\text{center}}$) for two heart beats, next to the output signal of the cardiac piston pump (Figure 4.3a) corresponding to the travel distance of the pumps piston.

As expected the flow velocity rises as the piston of the pump moves forward. However, the velocity-time graph in Figure 4.3b does not show the same curve as the output signal-time graph of the pump in Figure 4.3a. The second (smaller) peak clearly noticeable in the output signal-time graph (at $t = 0.45$ s and $t = 1.2$ s respectively) is not represented in the velocity response of the regurgitant jet, but rather one bulky peak is visible.

Yet, in the rise of the velocity-time graph, two small peaks are observable before the maximum velocity $u_{0,\text{center,max}}$ is reached. The first one at $t = 0$ s and $u_{0,\text{center}} = 1.7$ m/s is most likely due to the system inherent inaccuracy of the pump, i.e. due to the slight temporal deviation from the assumed frequency of 1.33 Hz (equaling 80 bpm). The system inherent inaccuracy of the pump is further investigated in Chapter 3.1.



(a) Output signal cardiac piston pump over time t (b) Outlet velocity in the center of the jet $u_{0,\text{center}}$ over time t

Figure 4.3: Temporal flow velocity response of pinhole L to the piston travel distance of the cardiac piston pump represented by the output signal.

The second peak at $t = 0.05$ s and $u_{0,\text{center}} = 2.9$ m/s, just before the maximum $u_{0,\text{center,max}}$ is reached, seems to be characteristic. It is observed for all generic MROPs. An potential explanation could be the "wobbling" of the PVC film. Figure 4.4 shows two consecutive PIV images of the experiments Pinhole L. In the second image a slight deformation of the film around the orifice is noticeable that could cause the slight decrease in outflow velocity.

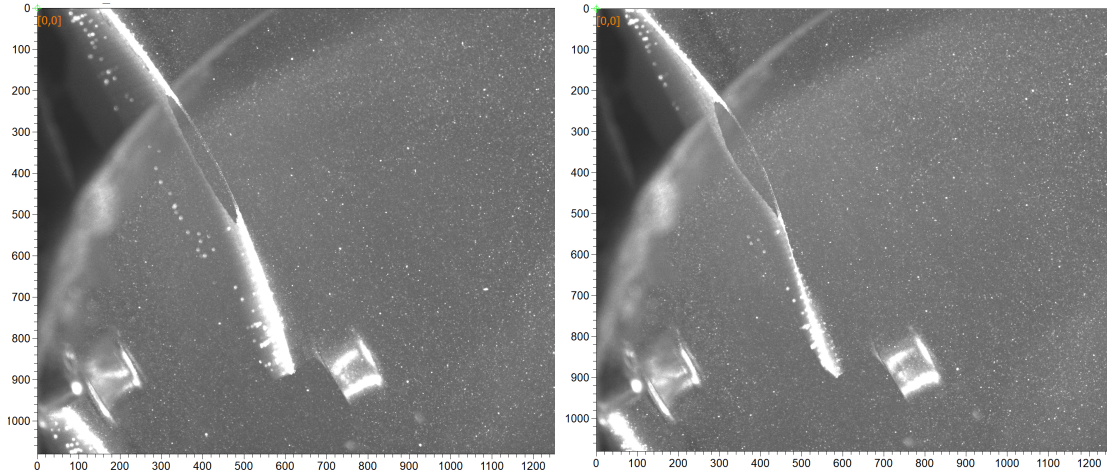
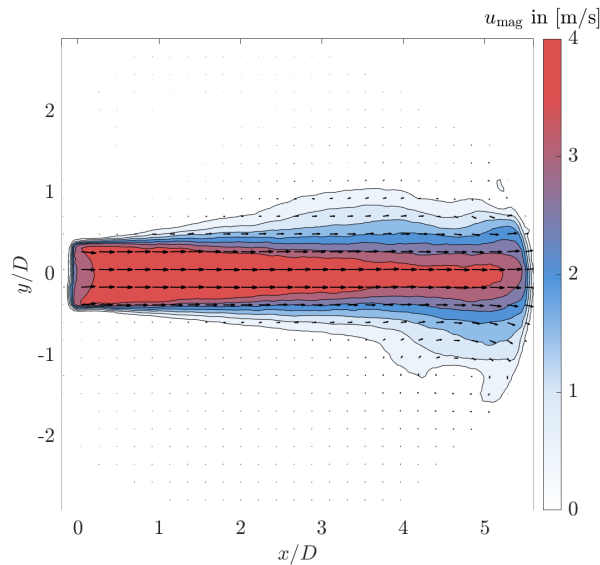


Figure 4.4: Consecutive PIV images in pixel-coordinates of Pinhole L showing the "wobbling" of the PVC film out the orifice during regurgitation.

4.1.2 Spatial Velocity Distribution

For stationary free jets, the potential core is expected to be observed up to distances from the orifice of $x/D = 2$ to 4 [72, 79, 97]. A triangular shape would be anticipated in the z -plane for both the pinhole and slot, whereas an asymmetrical distribution would be anticipated for the drop.

Figure 4.5 illustrates the velocity distribution of the three MROP shapes at a fully developed state of the pulsating free jet. The time that the jet reached full development was identified by finding the highest mean velocity in the flow field. For comparability with existing literature, the axes have been normalised to the orifice diameter. For non-circular orifices, the height was used as D (see Table 3.1).



(a) Pinhole L at $t = 0.03$ s

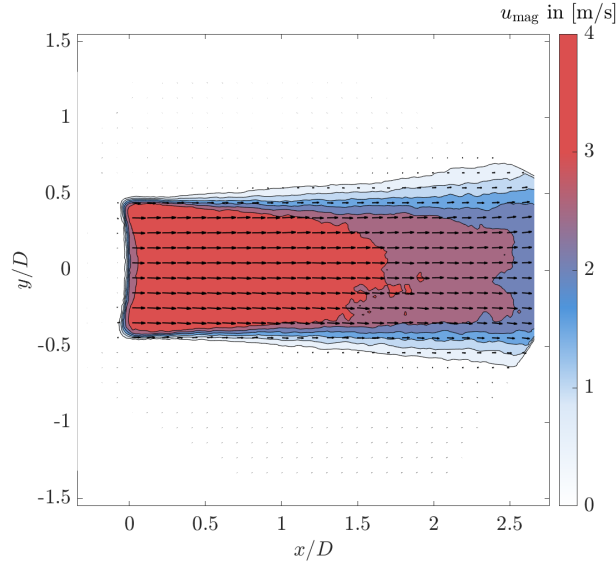
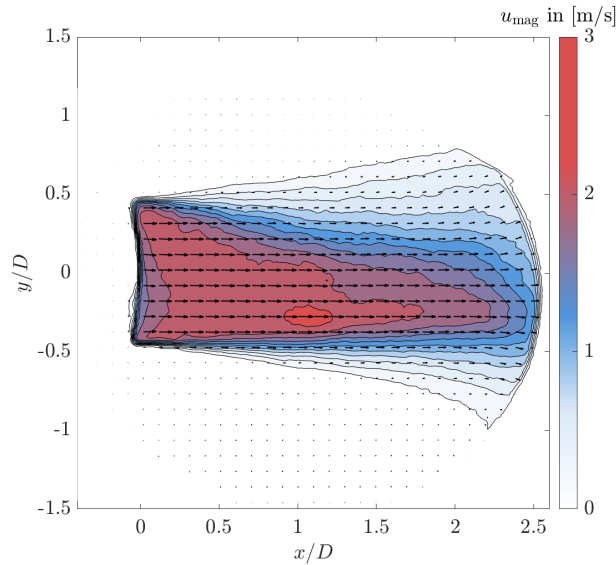
(b) Slot L at $t = 0.08$ s(c) Drop L at $t = 0.05$ s

Figure 4.5: Velocity magnitude u_{mag} distribution of three different orifice shapes at a fully developed state of the regurgitant jet.

Figure 4.5a shows a triangular potential core for the pinhole. A more bulky shape for the slot is shown in figure 4.5b. The potential core for the slot and the drop does not entirely fill the atrium. One possible explanation for this is the larger opening area (refer to Table 3.1) and the constant peak pressure in the ventricle ($p_{\text{ventricle}} = 120$ mmHg), which makes the jet less concentrated. Thus, the high-velocity regurgitation jet does not extend to the right side of the FOV, before the pump piston's movement direction reverses at $t = 0.2$ s and the force driving the regurgitation vanishes.

The results of the drop exhibits the anticipated asymmetrical, yet triangular shape of the potential core, with elevated values towards negative y/D positions corresponding to the location of the drop's circular end.

In the following the spatial velocity distribution for the three generic MROPs will be investigated in detail. Therefore, radial profiles in different distances from the orifice will be

presented. For stationary free jets, according to the theory, top-hat shaped velocity profiles near the outlet would be expected [72, 97, 32, 58]. For pulsating free jets, as in the case at hand, top-hat shaped and parabolic outlet velocity profiles are expected [58, 63, 39]. For high-aspect ratio orifices (drop and slot), and sharp edges saddle-backed outlet profiles are expected [23, 85, 74, 1, 60].

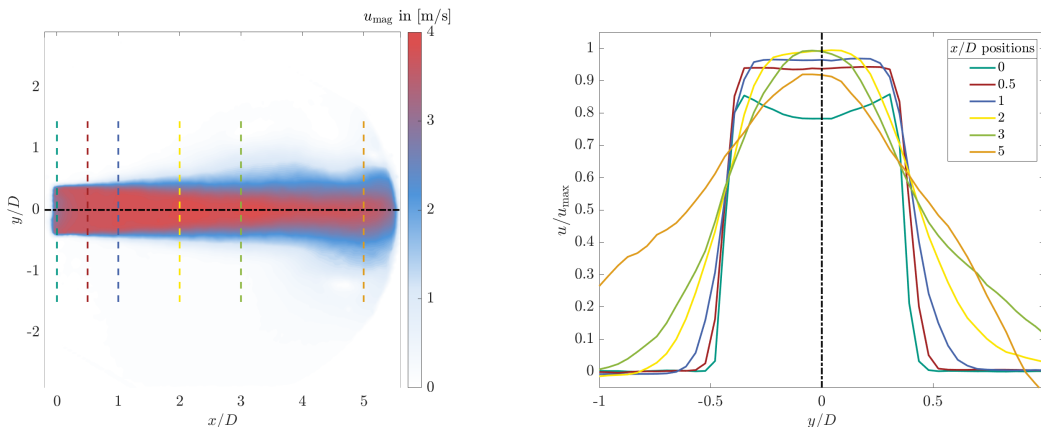
The maximum axial velocity u_{\max} is expected to be found close to the outlet for free jets, i.e. near $x/D = 0$ on the center line of the regurgitant jet. For thin plates, with nearly zero inlet length, u_{\max} is expected to be found further away from the orifice, due to the vena contracta effect [23, 74]. In addition, the findings regarding the potential core from Fig. 4.5 can be verified by means of the radial profiles of axial velocity in the following.

In Figure 4.6a the positions are marked on which the axial velocity component u of the jet will be analysed. The corresponding outcomes are exhibited in Figure 4.6b beside. A saddle-backed outlet velocity profile at $x/D = 0$ is observed. According to the theory, two potential explanations exist. First, the thin film of the generic MROPs exhibit sharp edges and nearly zero inlet length. The vena contracta effect observed for such geometries, leads to saddle-backed outlet profiles [74, 23]. In addition, the atrial wall opposite the MROP could influence the velocity, as outlined by Jeffers et al. [45].

In agreement with the theory (see Chapter 2.2.2), the velocity at the outlet is only around 80% of u_{\max} and the maximum is reached around $x/D = 2$.

From the outlet, the saddle-backed radial profiles progresses downstream to a top-hat shape at 0.5 times the orifice diameter D before it changes shape again around $x/D = 2$. The self-similar profiles found for $x/D > 2$ are characteristic of free jets [72, 97, 39, 74, 63, 32]. The alteration in shape is accompanied by a reduction in center line velocity and broadening of the radial profile, i.e. a radial spreading of the axial velocity. These effects are due to the entrainment of quiescent surrounding fluid, as explained in the fundamentals of this work (Chapter 2.2.2).

Furthermore, it is evident from Figure 4.6b that the velocity close to the center of the jet is within 95% of u_{\max} for $x/D = 0.5$ to 3, supporting the theory of the potential core of free jets, which indicates that its end is located between 2 to 4 times D [72, 97, 32].



(a) Axial x/D positions at which the radial profiles of the axial velocity will be investigated. (b) Radial profiles of axial velocity for different x/D positions.

Figure 4.6: Exemplary visualization of x/D position where radial distribution of the axial velocity is analysed and results for the pinhole shape, fully developed state, $t = 0.03$ s.

Figure 4.7 demonstrates the radial velocity profiles of the slot and drop, with dimensionless axial positions adjusted to account for larger orifice sizes. Similar to the pinhole, a saddle-backed profile can be observed for both, the slot and drop, at the outlet. Additionally, both shapes exhibit an initial rise in maximum velocity as the top-hat shaped profile develops. Subsequently, velocity decreases and the jet begins to spread in lateral direction. Compared to the pinhole, the spread is less pronounced, notably for the slot. For the drop, as expected, a asymmetric velocity distribution appears in Fig. 4.5c, particularly beyond axial distances of 0.5 times D .

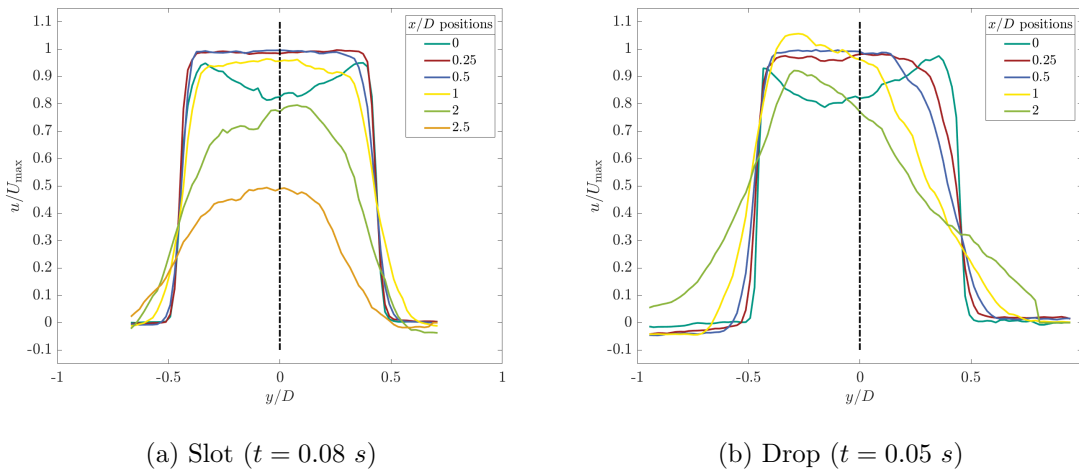


Figure 4.7: Radial distribution of the axial velocity for different x/D positions for slot and drop shaped orifices, fully developed state.

In the following, the center line velocity $u_{\text{center}}(x)$ for the fully developed phase of the circular jet, originating from the pinhole, will be investigated. The slot shows similar results to the pinhole, while the center line velocity of the drop is not representative due to its asymmetric radial velocity distributions and no clear definition of the center. Hence, only the results of pinhole shaped orifices provide relevant information and will be discussed here. Based on the theory in Chapter 2.2.2 the hypothesis is, that $u_{\max}(x)$ is reached at $x/D \approx 2$, as already stated by [74] and [23]. Furthermore, a linear decrease of $u_{\max}(x)$ for $x/D > 2$ is expected, in accordance with [72, 23] and [32].

Figure 4.8 shows the normalized center line velocity $u_{\text{center}}(x)$ for $t = 0.03$ s. As already observed in the analysis of the radial velocity profiles, u_{\max} is not reached directly at the outlet, but further downstream at $x/D = 2.1$ showing conformity with [74] and [23]. A potential explanation for this phenomena is the vena contracta effect described by [74] and [50].

The second peak observable further downstream at $x/D = 3$ suits the temporal development of the velocity measured at the outlet (see Fig. 4.3b), where two consecutive peaks are observable as well.

To examine the decay of $u_{\text{center}}(x)$, a straight line was fitted to the graph (least square approach) from the point, where u_{\max} is reached, using the method of least squares. It remains uncertain whether the assumption of a linear velocity decay is valid due to the relatively short axial distances observable in the LA.

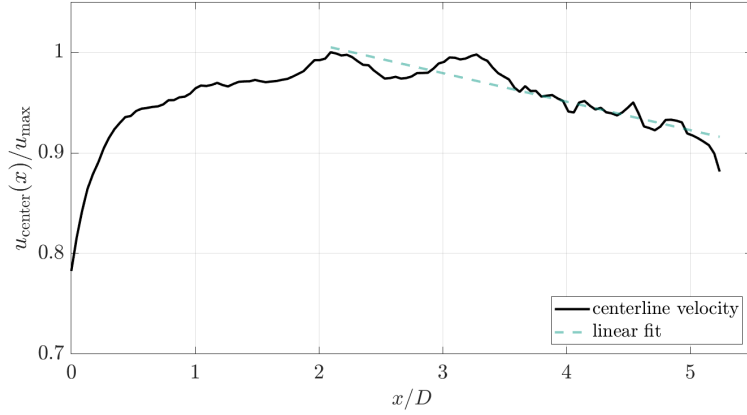


Figure 4.8: Center line velocity $u_{\text{center}}(x)$ for the fully developed state of the regurgitant jet originating from pinhole L; normalised for the maximum velocity in x -direction u_{max} .

Smaller orifice diameters, as for for the pinhole S and M facilitate the investigation of larger x/D values. Figure 4.9 is shown to verify the hypothesis of linear decreasing center line velocity in the far field, as stated, for example, in [72], [97] and [32].

In the time frame of this thesis phase-resolved measurements could be conducted for only one size of each shape. Thus, phase-averaged data is used for this comparison. As before, the linear fits start at the respective u_{max} for each MROP. The linear fits show greater significance for larger spans of x/D values.

Different slopes of the linear fits are observed in the plot. To investigate whether this is due to the relative length scale on the x -axis or is a consequence of some other cause, the same curves are plotted on the absolute axial scale in Figure 4.10. For pinholes S and M, similar velocity decreases are observed on the absolute axial scale. For pinhole L the relative velocity decrease is smaller, i.e. a higher velocity is carried further downstream until $x = 73$ mm. The proximity to the potential core, which is defined based on the orifice size, could explain the rather small velocity decrease in this region. At $x \geq 74$ mm the velocity decreases rapidly, which can be explained by the fluid being dammed up by the atrial wall.

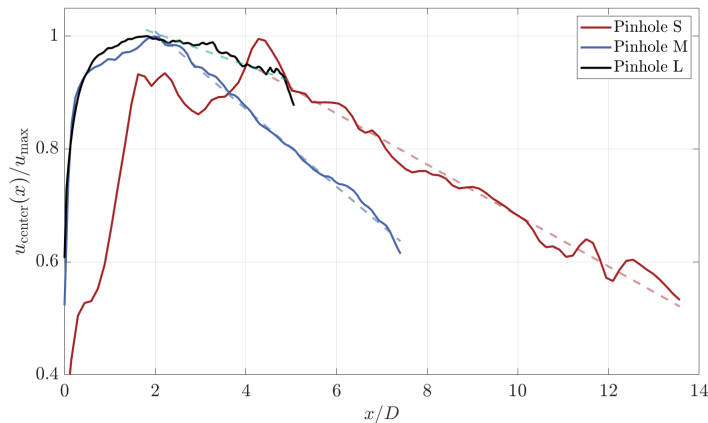


Figure 4.9: Center line velocities $u_{\text{center}}(x)$ for the fully developed phase of the regurgitant jet originating from pinholes S, M and L; all normalised for the respective maximum velocity in x -direction u_{max} .

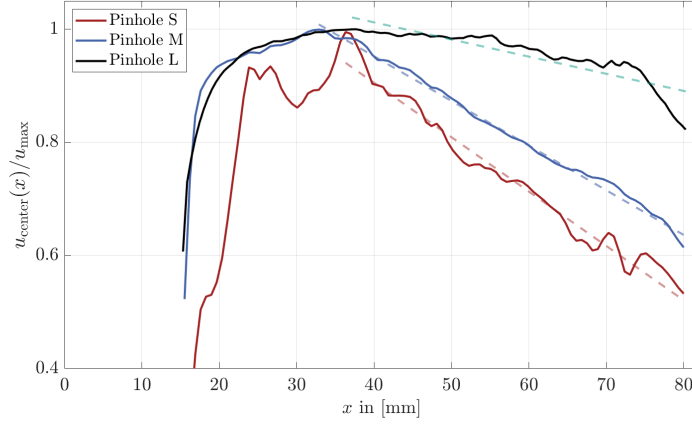


Figure 4.10: Center line velocities $u_{\text{center}}(x)$ for the fully developed phase of the regurgitant jet originating from pinholes S, M and L on an absolute axial coordinate scale; all normalised for the respective maximum velocity in x -direction u_{max} .

Subsequent the shape of the regurgitant jets originating from the generic MROPs will be discussed, based on the fundamental formulas introduced in Chapter 2.2.2. For stationary circular turbulent jets it is expected that the half width radius $r_{1/2}$, defined as the point, where the axial velocity $u(x)$ exceeds 50% of the center line velocity $u_{\text{center}}(x)$, is constant within the potential core. Downstream of the potential core a linear increase of $r_{1/2}$ is expected, as stated by Pope [72] and Schlichting [79].

Figure 4.11 shows the contour plot of the velocity distribution for pinhole L and S including the graph of the radius $r(x)$ and half-width radius $r_{1/2}(x)$. The radius was defined as the point where $u(x)$ falls under 20% of the center line velocity $u_{\text{center}}(x)$ for a given axial distance x . This provides a general visualisation of the spreading of the jet. The half-width radius was calculated in alignment with the definition in Chapter 2.2.2. The plots have been generated based on averaged PIV recordings. Due to the limited size of the LA large x/D values cannot be analysed for large orifices. For the medical purpose of this thesis this is no restriction, as the flow characteristics of the regurgitant jet *in the heart simulator* are of interest. Nevertheless, for the fluid mechanical purpose, the linearity of the spreading was analysed for pinhole S (Fig. 4.11b), where larger x/D values are possible.

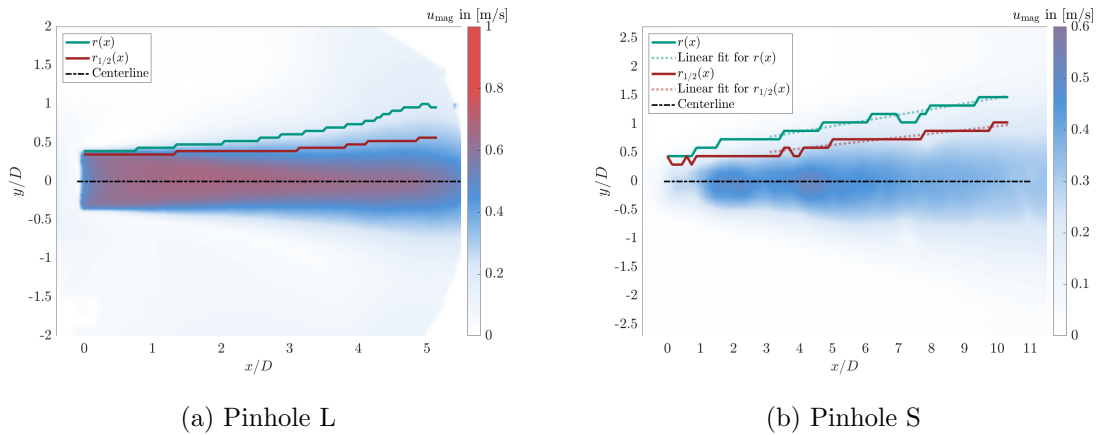


Figure 4.11: Radius $r(x)$ and half-width radius $r_{1/2}(x)$ for two pinholes. The velocity magnitude u_{mag} calculation is based on phase-averaged PIV recordings.

A linear increase of $r_{1/2}(x)$ can be observed for pinhole S. However, the spatial resolution of the recordings is too low to make reliable statements. Furthermore, $r_{1/2}(x)$ is defined for stationary free jets, leaving this interpretation questionable. As this particular characterisation of the flow is not specifically relevant for the medical problem at hand, no further investigation was conducted in that regard.

For the drop and slot the three-dimensional shape was analysed using the traversed PIV recordings. Figure 4.12 shows exemplary slices through the three-dimensional two-component (3D2D) velocity vector field of the two MROPs.

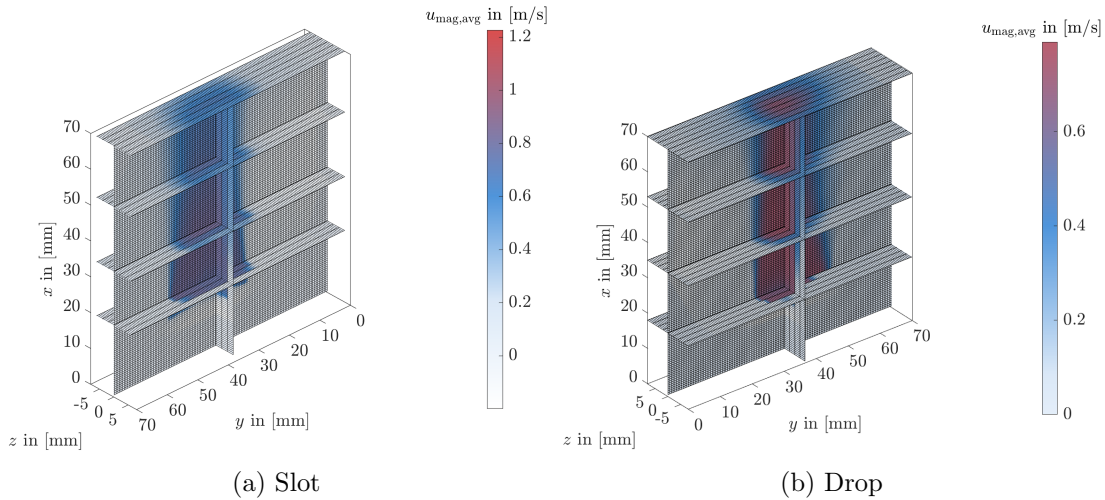


Figure 4.12: Exemplary slices through the 3 dimensional 2 component velocity vector field of the slot and drop; calculated with phase-averaged PIV recordings.

For non-circular orifice shapes the development of a circular jet is expected downstream. Figures 4.13 and 4.14 show the spreading of the jets in the x -planes at different axial positions x/D . It is obvious that the resolution in the x -plane was too coarse to adequately display the pointed oval shape of the slot and the shape of the drop. Nevertheless, the development towards a circular jet can be observed for both MROPs, with a slightly clearer results for the drop.

It is assumed, that similar to the outflow, the inflow into the orifice also represents the shape of the orifice. Thus, the flow convergence is not hemispheric, as assumed in the calculations of the PISA method [100]. Supposedly, with increasing distance from the orifice the convergence tends to get hemispheric, if a similar behaviour as for the outflow is assumed. Therefore, decreasing the Nyquist limit and thus, V_a would decrease the error of the assumption made in that regard, due to the increased PISA radius. Further validation of this assumption is recommended, e.g. by conducting PIV experiments of the flow convergence in the LV.

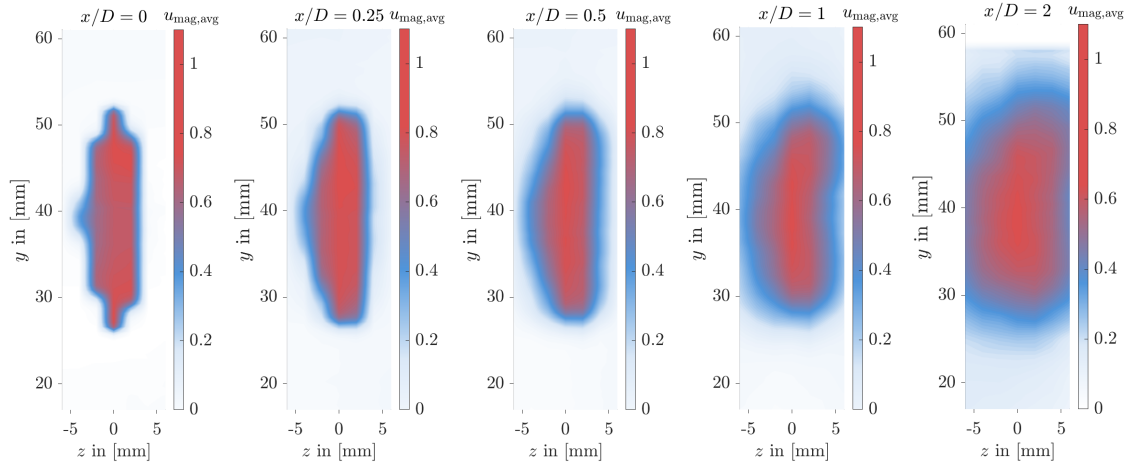


Figure 4.13: Three dimensional spreading of the free jet originating from the slot; visualized via the velocity distribution in the x -planes at different axial positions x/D . The velocity magnitude $u_{\text{mag,avg}}$ is given in [m/s] and is calculated based on time-averaged PIV recordings.

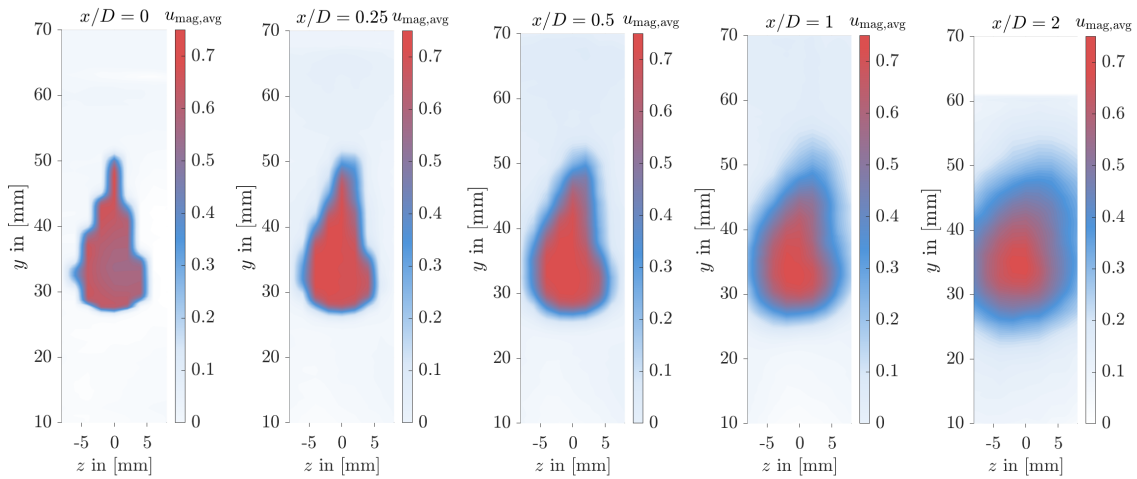


Figure 4.14: Three dimensional spreading of the free jet originating from the drop; visualized via the velocity distribution in the x -planes at different axial positions x/D . The velocity magnitude $u_{\text{mag,avg}}$ is given in [m/s] and is calculated based on time-averaged PIV recordings.

4.1.3 Vortex Detection

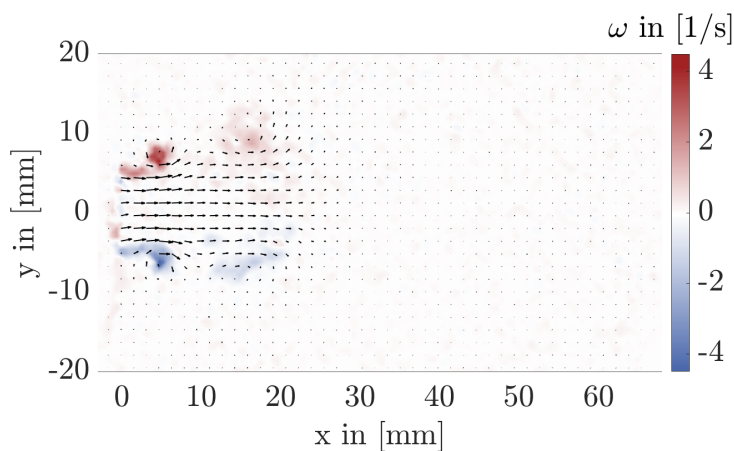
This section outlines the findings from the flow analysis of vortices for the generic MROPs. The focus is on examining the feasibility of detecting vortices on the measured data, the analysis of the vortex formation near the outlet and the decay of vortex structures near the LA wall. The analysis of the starting vortex represents an important step towards understanding the characteristics of regurgitant jets, while the vorticity decay towards the end of the LA could allow an estimation of the flow's effect on the muscular wall.

The starting vortex ring is expected to travel along the regurgitant jet front, with smaller scale vortical structures (Kelvin-Helmholtz instabilities) at the jet barriers upstream (see Chapter 2.2.3). Three-dimensional vortex rings are represented as vortex pairs in a 2D flow field. This is achieved through an analysis of the vorticity ω of the flow field and the application of the vortex detection criteria Q and Γ_1 , as introduced in Chapter 2.2.3. Single PIV image pairs were utilised to detect vortices without any prior in-phase or between-phase averaging. This technique enables the immediate observation of vortical structures within the flow field, including small-scale effects. As the instabilities within the boundary layer, which are fundamental for vortex roll-up (refer to Fig. 2.16), are not located identically in each frame, averaging would result in their loss.

Pinhole L, with its regurgitant jet filling out the entire atrium, provides the best initial overview of vortex progression during regurgitation. The slot yields comparable outcomes, whereas the drop reveals less distinct boundaries in the ω distribution, owing to its lack of rotational symmetry. Due to space restrictions, and limited relevant new findings for the slot and drop, only the ω distribution of pinhole L is presented in Figure 4.15.

As the regurgitant jet starts to emerge close to the end of each period cycle ($T = 750$ ms) and progress into the subsequent one, two period cycles were recorded. This allows the coherent visualization of the vortex development during regurgitation.

At 740 ms, the jet emerges from the orifice, with high ω values on both sides of the jet. Positive omega denotes counter clockwise rotation (red sections), while negative values indicate clockwise rotation (blue sections). It is observable, that the starting vortex separates from the MROP film and moves with the jet in the x -direction. Upstream of the starting vortex, elevated vorticity is visible in the shear layer of the free jet, as anticipated (see Chapter 2.2.3). At the 780 millisecond mark, the jet collides with the LA wall and a more evenly distributed vorticity in the FOV is observed. It is hypothesized, that the initial vortex dissipates upon impact with the wall, resulting in a more disturbed flow situation.



(a) $t = 740$ ms

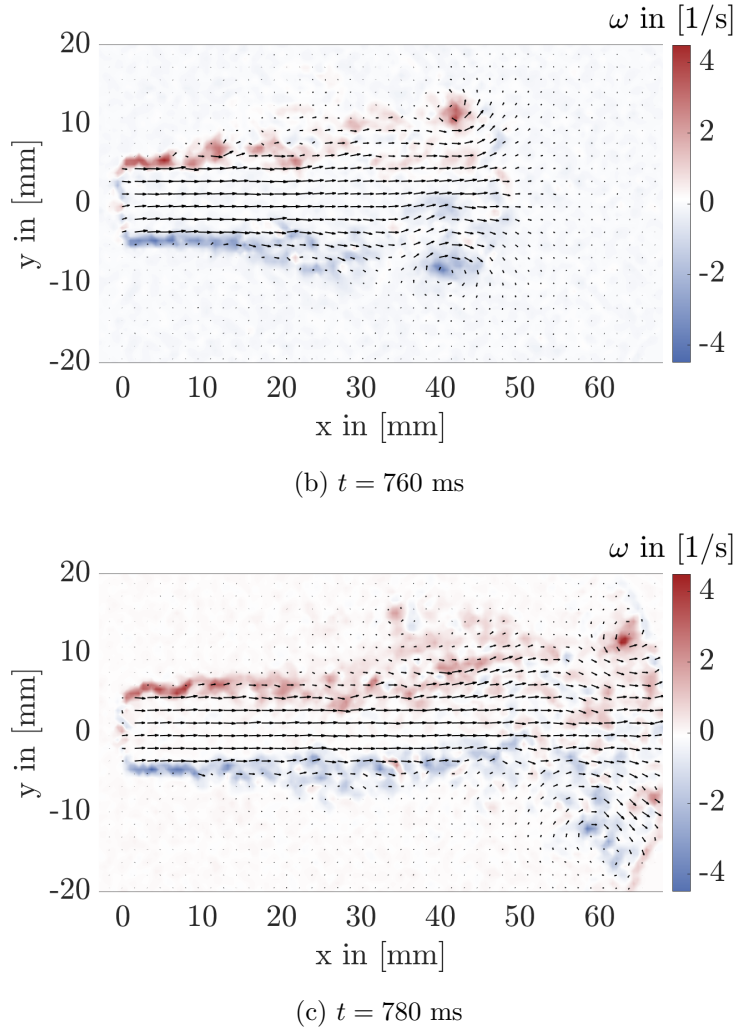


Figure 4.15: Vorticity ω distribution for three different phases for pinhole L.

As vorticity does not necessarily indicate the presence of vortices [54], the following phases will be analysed using the Q -criterion.

Figure 4.16a displays the emergence of the jet, clearly illustrating the core of the starting vortex ring, represented by the two red dots. As regurgitation progresses, the Q -criterion detects axial movement of the vortex core in positive x -direction. As already estimated, based on the vorticity distributions, Kelvin-Helmholtz instabilities can be observed via increased Q magnitude in the shear layer upstream of the starting vortex.

The usual alternating pattern of positive and negative Q values is noticeable. At $t = 780$ ms (Fig. 4.16c), when the vortex collides with the atrium wall, solely a sharp core in the upper section of the shear layer is identified by the Q -criterion. This implies that the lower portion of the vortex has already decayed due to the collision with the wall. Comparable findings can be noticed for the slot and drop, but are skipped here due to the lack of new relevant information.

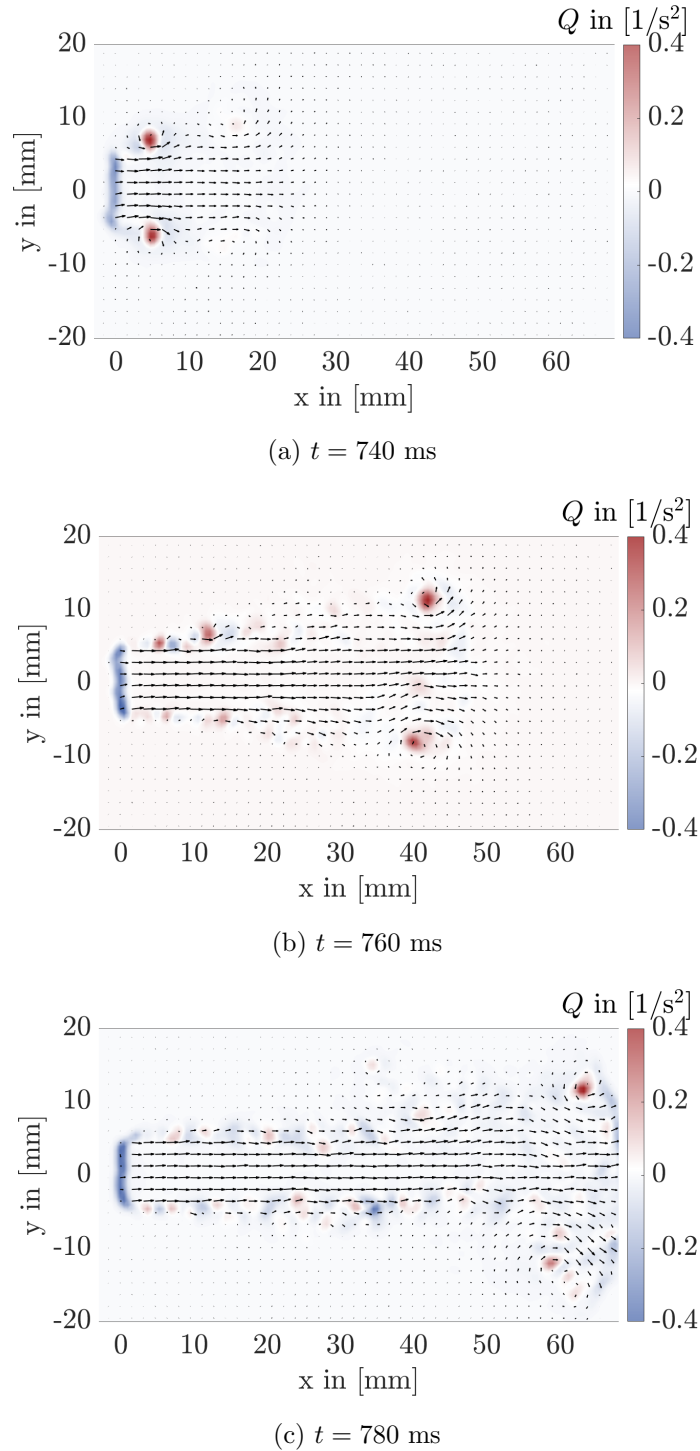


Figure 4.16: Vortex detection by means of the Q -criterion for three different phases during regurgitation for pinhole L.

The Γ_1 -criterion, identifies vortices based on the streamline topography, in contrast to gradient-based Q -criterion. To implement the Γ_1 -criterion, a script from Fernando Zigunov (2019) was adapted in MatLab with minor code modifications. The analysis region size was set to 8 px. Figure 4.17 displays the results at $t = 770$ ms and compares them to the Q -criterion results.

It is apparent that both detection criteria are effective for the experimental data. The Q -criterion possesses greater sensitivity for detecting vortex cores, while Γ_1 identifies less

intense vortical structures within the jet's surrounding region. The starting vortex is confirmed as the strongest vortical structure in the flow field according to both criteria, with the detected position coinciding.

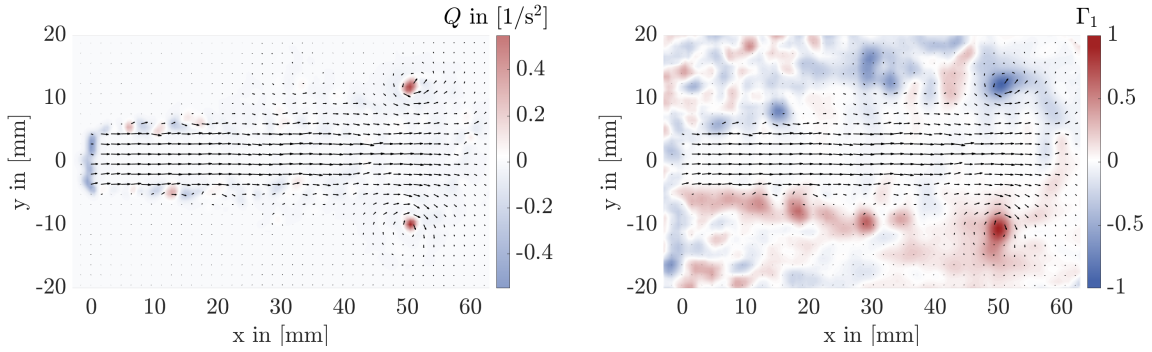


Figure 4.17: Vortex detection by means of the Q - and Γ_1 -criterion for for pinhole L at $t = 770$ ms.

To further study the formation, growth and dissipation of the starting vortex, phase-resolved measurements with $\Delta t = 2$ ms between the phases were performed for slot L. The aim of this investigation is to quantify the vorticity of the vortex as a function of the distance travelled. Especially relevant is the amount of remaining vorticity when the vortex impinges on the atrial wall, as this could lead to pathological regional muscular hypertrophy (abnormal and unhealthy growth of the muscular wall) according to Jun. Prof. Dr. Sandy Engelhardt (Ruprecht-Karls-Universität Heidelberg).

Figure 4.18 offers an overview of the development of vortical structures using Γ_1 for various phases of the slot L experiments. Please note, that due to space constraints, not all phases are displayed here.

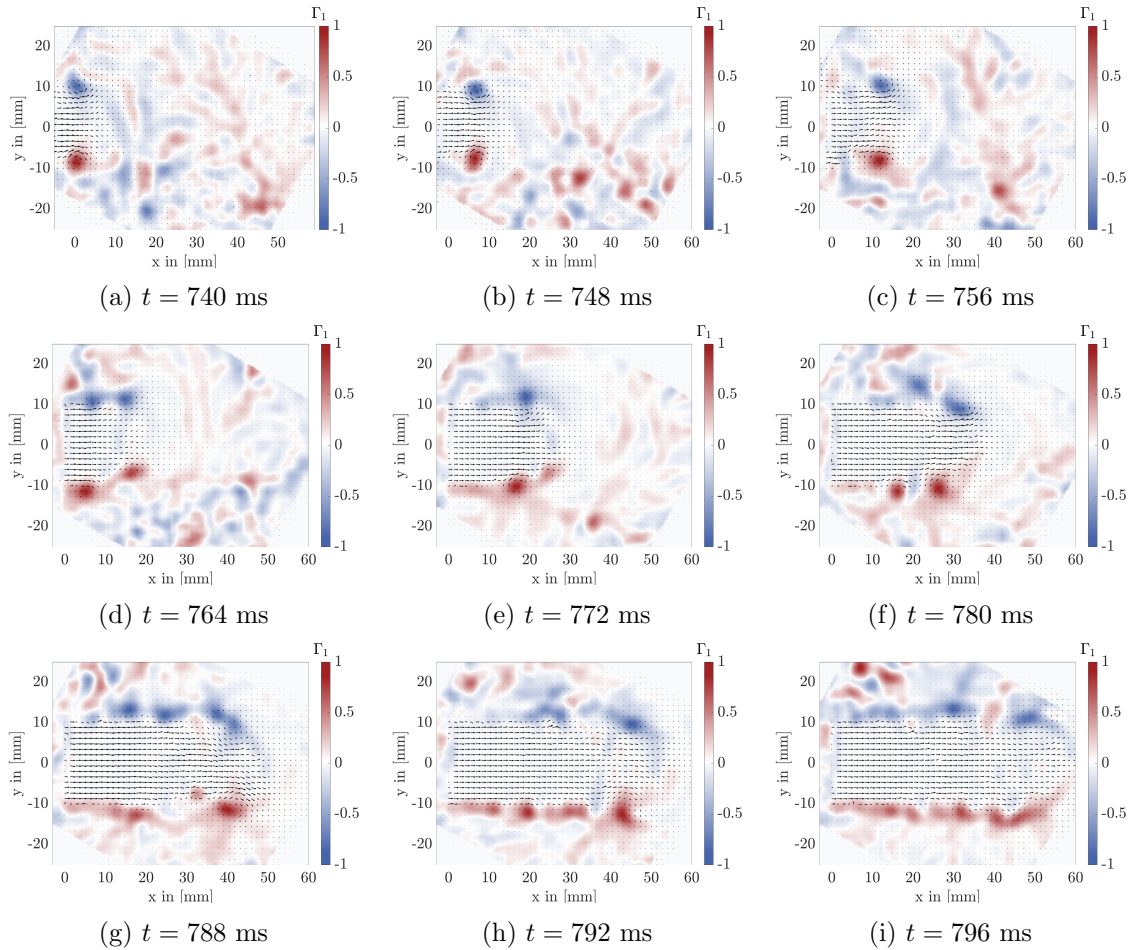


Figure 4.18: Vortex detection by means of Γ_1 for 9 phases of the regurgitant jet of slot L, separated by $\Delta t = 4$ ms each.

In the first row of figures, from $t = 748$ ms until $t = 756$ ms, a vortex pair forms and separates from the PVC film. This is considered as the starting vortex ring. At $t = 764$ ms, a second vortex pair can be identified via the Γ_1 criterion. In both successive figures, the second vortex pair is visible, although it is less perceptible at $t = 772$ ms. According to the Q -criterion, no second vortex pair can be detected during the corresponding time phases, stating the improved performance of Γ_1 over Q for the present case.

The graph of the motion of the cardiac piston pump (3.3) could be an indication of the double vortex ring formation, as it does not show a sinusoidal curve, but a more complex curve. Furthermore, multiple starting vortex ring formation for pulsating free jets is also found in Chang et al. [16]. The number of and distance between them, depends on the Reynolds and Strouhal numbers, according to [16]. To evaluate the vortex formation in detail and to draw medical conclusions about the potential damage caused by the two vortex rings, high speed PIV is recommended.

Figure 4.19 shows the outlet velocity at the centre of slot L during the phase when the regurgitant jet is present. The regurgitation time $(\Delta t)_{\text{reg}}$, i.e. the phase in which $u_{0, \text{center}}$ is rising, is 100 ms long (gradient based calculation). A saddle in the velocity profile is observed at $t = 766$ ms just before $u_{0, \text{center}}$ reaches its maximum of 3.6 m/s. This additional peak may be caused by vortex formation, as some of the jet's kinetic energy is used to roll up the boundary layer, reducing the axial exit velocity at this point. A similar behaviour has already been discussed in the section on the temporal velocity distribution for the pinhole (see Fig. 4.3b).

As explained for the pinhole (see explanation of Fig. 4.3), the first smaller saddle at

$u_{0,\text{center}} = 1.4 \text{ m/s}$ is most likely due to the previously mentioned inaccuracy of the pump, as it is at the exact spot where two period cycles are merged, and the saddle is not visible in the output signal of the pump (see Chapter 3.1).

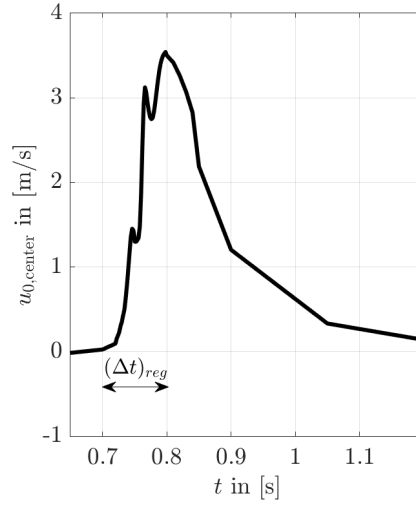


Figure 4.19: Outlet velocity in the center $u_{0,\text{center}}$ of slot L during regurgitation.

Figure 4.20 illustrates the maximum magnitude of vorticity $|\omega_{\text{max}}|$ plotted over two period cycles (red dotted line). Furthermore, the x -position of the strongest vortex was identified and plotted as a blue solid line adjacent to it. Figure 4.21 presents the same graphs as Figure 4.20 but depicts a zoomed-in view to enhance visibility of the phenomena during regurgitation.

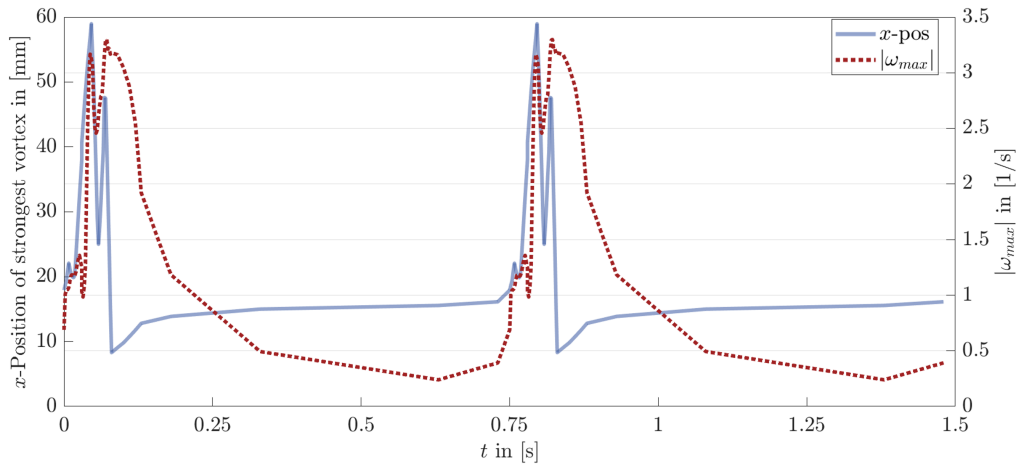


Figure 4.20: x -position ($x\text{-pos}$) of the strongest vortex detected by means of Γ_1 (blue solid line) and maximum vorticity magnitude $|\omega_{\text{max}}|$ (red dotted line) for two period cycles (slot L).

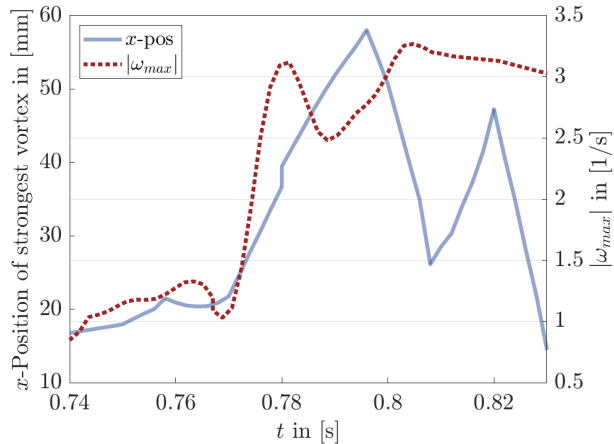


Figure 4.21: x -position (x -pos) of the strongest vortex detected by means of Γ_1 (blue solid line) and maximum vorticity magnitude $|\omega_{max}|$ (red dotted line) over the time t for 10 ms during regurgitation (slot L).

As anticipated, based on 4.18, the initial vortex displays the highest intensity during regurgitation and moves from the point of origin towards the atrial wall at $x = 60$ mm. The vorticity grows with the distance travelled by the initial vortex, which might be explained by the additional supply of fast-flowing fluid through the orifice increasing the circulation. When the vortex collides with the wall at 795 ms (x -position = 60 mm), the vorticity rapidly decreases, and consequently, the vortex dissipates, as evident in 4.18.

Interestingly, $|\omega_{max}|$ (and also the x -position) then increases again, at $t = 807$ ms. A plausible reasoning for this behavior could be that once the starting vortex dissipates, the subsequent vortex becomes the strongest. The second vortex does not impact the wall, as its x -position only reaches 48 mm. Therefore, it dissipates prematurely, likely due to insufficient fluid supply to the regurgitant jet (pump piston reverses).

Surprisingly, then the second vortex exhibits a greater maximum vorticity magnitude $|\omega_{max}|$ than the initial vortex. The increased vorticity may be explained by the velocity time curve near the outlet (see fig. 4.19). As explained above, the velocity rises again after the saddle at $t = 766$ ms. This behaviour may result in the formation of the two vortex pairs, with the second having increased vorticity, as the fluid accelerates to its peak value of $u_{0,center,max} = 3.6$ m/s at $t = 796$ ms.

To gain a thorough understanding of the phenomena described, more detailed measurements exceeding the temporal and local resolution achievable within the time frame of this thesis are required.

4.2 Eccentric Jet Producing Mitral Regurgitation Phantom

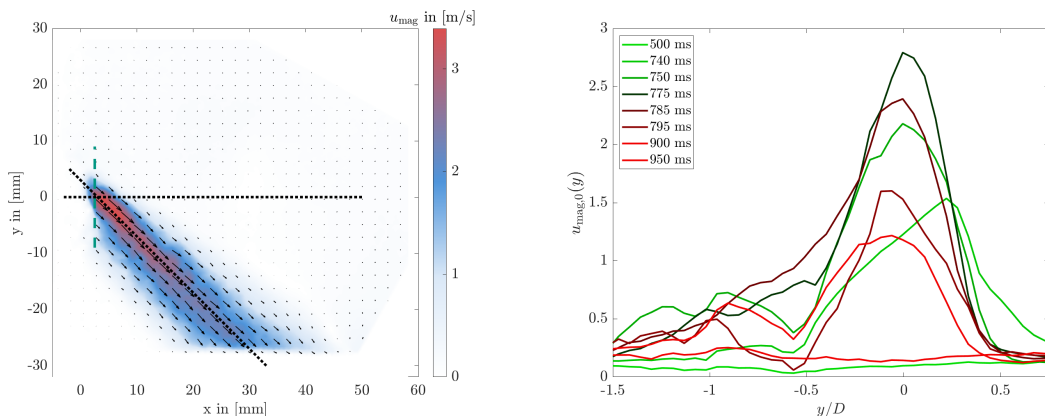
In this section, the analyses conducted on the generic MROPs will be applied to a more specific flow situation. The eccentric jet producing MV, known as EccJet, also falls under the category of MROPs as it simulates a closed MV with an insufficiency. The primary objective of this section is to provide a comprehensive and logical understanding of the flow structures in the pulsating free jet originating from the EccJet, rather than drawing comparisons with fundamental literature. As the significance of US measurements is very limited for eccentric jets, the understanding of this flow situation is especially relevant for the medical purpose of this thesis [96, 73, 29].

The section will proceed by first analysing the temporal and spatial velocity distributions, followed by the presentation of the vortex detection results.

4.2.1 Temporal Velocity Distribution

It is expected that the temporal course of the velocity magnitude, u_{mag} , will exhibit comparable curves to the pinhole MROP, but rotated by 30° . This hypothesis shall be examined in the following.

Figure 4.22a provides an overview of the u_{mag} distribution of the EccJet during regurgitation with the center line of the eccentric jet compared to the horizontal line. The eccentricity of 30° corresponds to the angle between the two dotted black lines.



(a) Velocity magnitude u_{mag} distribution at $t = 785$ ms for the eccentric jet producing Mitral valve phantom. (b) Temporal development of the velocity magnitude $u_{\text{mag},0}(y)$ at the outlet during regurgitation.

Figure 4.22: Overview of the velocity distribution of the eccentric jet producing Mitral valve phantom and temporal development of the velocity magnitude at the outlet ($u_{\text{mag},0}(y)$).

The radial outlet velocity $u_{\text{mag},0}(y)$ profiles are shown in Figure 4.22b. The green dashed line in Figure 4.22a indicates the position, where the profiles are determined.

The profiles exhibit similarities with the pinhole results in Section 4.1.1, whereby the increase (green curves) and decrease (red curves) of $u_{\text{mag},0}$, along with the spreading of the profiles, are evident. However, the profiles of the rigid EccJet lack the saddle-backed shape identified in MROPs made from 0.5 mm thin PVC film (generic MROPs). This discovery aligns with the literature where saddle-backed profiles are linked to the sharp edges and little inlet lengths of orifices [74, 23]. The absence of a wall perpendicular to the main flow direction could as well influence the shape of the velocity profiles, as found by Jeffers et al. [45] and Yao et al. [95].

Figure 4.23 shows the outlet velocity magnitude $u_{\text{mag},0,\text{center}}$, determined at the point where the green dashed line and the black dotted line in 4.22a intersect.

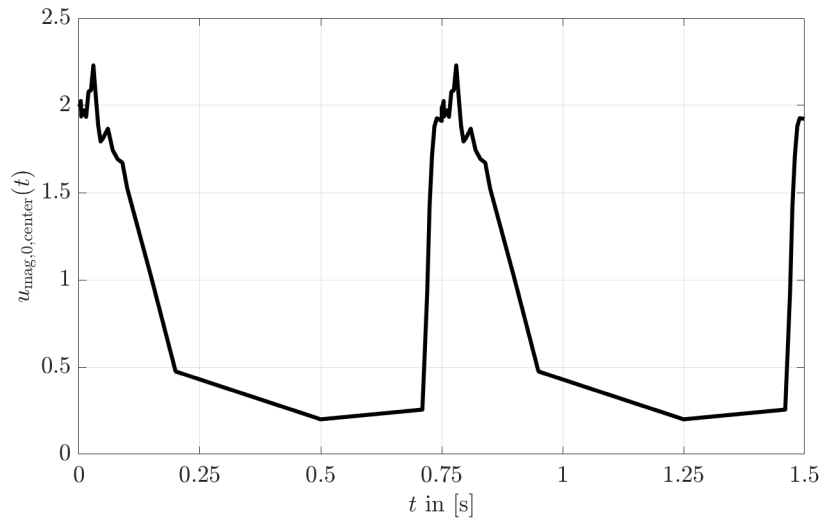


Figure 4.23: Outlet velocity magnitude $u_{\text{mag},0,\text{center}}$ for two period cycles for the eccentric jet producing Mitral valve phantom.

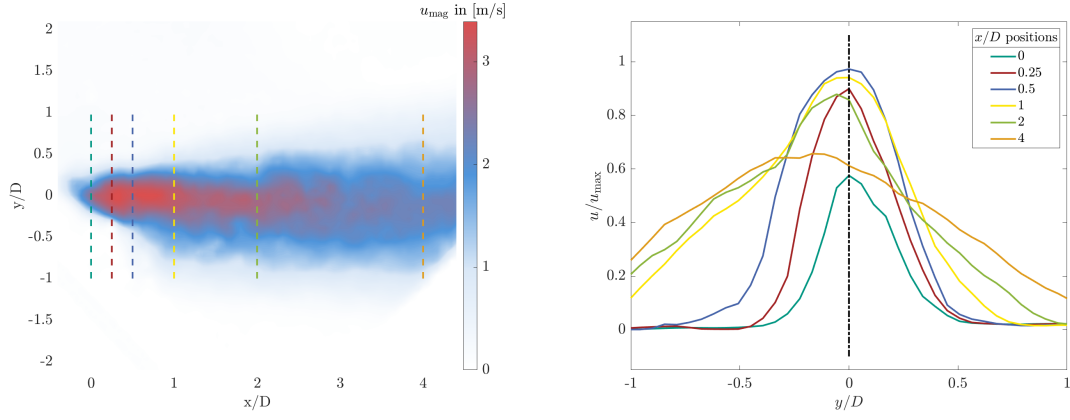
As expected, the graph looks similar to the one for the pinhole or slot presented in 4.1.1, showing a strong increase in the velocity magnitude during the time of regurgitation $(\Delta t)_{\text{reg}}$, followed by a decrease and small velocity magnitudes for the rest of the period cycle. Nevertheless, the two clear saddles apparent for generic MROPs cannot be definitively identified here (refer to 4.19). It can be deduced that the material of the MROP rather than the pump characteristics is responsible for the saddle-shaped velocity versus time curve. To confirm this hypothesis, experiments with higher temporal and spatial resolution near the outlet are required.

4.2.2 Spatial Velocity Distribution

For the analysis of the spatial velocity distribution, the EccJet is rotated by 30° to create a horizontal regurgitation jet. This enables to determine whether the jet from the EccJet differs from the one from the pinhole in more than just the flow direction.

Figure 4.24a displays the rotated jet in its fully developed state ($t = 785$ ms) along with the axial positions where radial velocity magnitude profiles are derived. The appropriate colour-coded velocity profiles are displayed on the right.

The radial velocity profiles illustrated in figure 4.24b demonstrate a decline in maximum velocity and jet spread resulting from the entrainment of the quiescent fluid in the LA of the heart simulator. The almost constant peak of the radial profiles between $x/D = 0.25$ and $x/D = 2$ is consistent with the potential core of the free jets theory [72, 32, 97].



(a) Velocity magnitude u_{mag} with positions where the velocity profiles are determined. (b) Radial velocity magnitude u_{mag} profiles in different axial distances from the orifice.

Figure 4.24: Spatial distribution of the velocity magnitude for the eccentric jet producing valve for the fully developed state of the regurgitant jet ($t = 785$ ms) rotated by 30° .

A notable difference between the radial profiles obtained for the EccJet and the generic MROPs lies in the shape of the profiles, which is evident when analysing the temporal development of the velocity near the outlet (refer to Chapter 4.2). The results from the EccJet demonstrate almost Gaussian curves instead of saddle-backed profiles, as previously observed by [39], [18] and [58] for pulsating free jets and by [72], [32] and [63] for stationary free jets. Their findings can be validated by the results of this thesis.

Figure 4.25 presents a three-dimensional overview of the regurgitant jet from the EccJet experiments. As expected, the jet spreading looks similar to the observations made for the pinholes. Since no new findings have been made in comparison with the pinholes, the three-dimensional spreading will not be discussed in further detail.

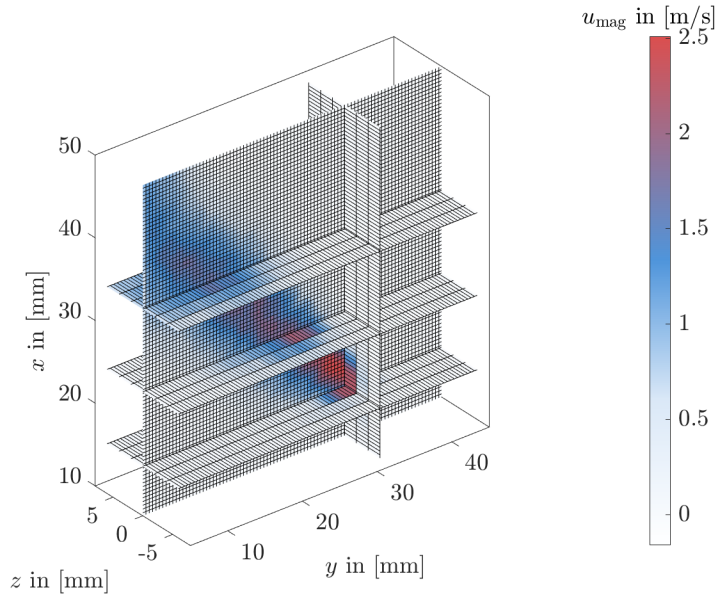


Figure 4.25: Overview of the three-dimensional velocity magnitude u_{mag} distribution for the eccentric jet producing Mitral valve at a fully developed state

4.2.3 Vortex Detection

In terms of vortex detection, the analysis of the EccJet aims to objectively identify variations in vortex formation and behaviour due to the eccentricity. Especially, the effects of the jet's proximity to the atrial wall are medically relevant and therefore, presented and discussed [91, 33]. Furthermore the performance of the vortex detection criteria Q and Γ_1 are compared.

Figure 4.26 shows the vorticity ω , and the vortex detection via the Q - and Γ_1 -criterion at the initial ($t = 720$ ms), and final ($t = 810$ ms) stages of the regurgitation.

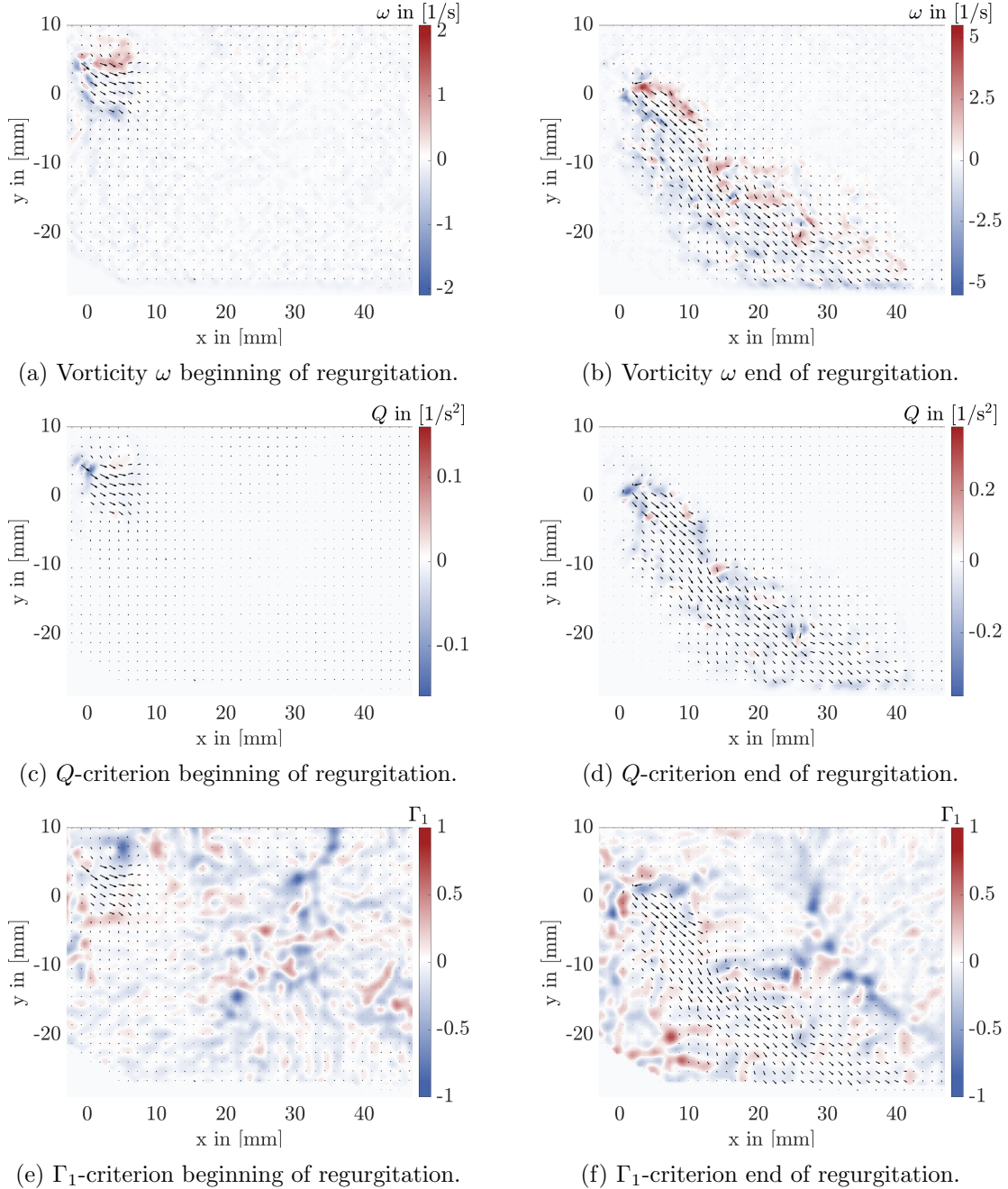


Figure 4.26: Vorticity and vortex detection by means of the Q - and Γ_1 -criterion for the eccentric jet producing Mitral valve phantom. The left side shows the time of emergence of the jet ($t = 720$ ms), while the right side shows the end of regurgitation ($t = 810$ ms).

The vorticity plots presented in Figures 4.26b and 4.26a illustrate elevated ω levels at the jet boundaries. The outcomes exhibit similar observations to the generic MROPs, but rotated by the jet angle. The Q -criterion also detects vortices in the respective regions. However, in contrast to the generic MROPs, a clear distinction between the upper and lower boundary layer is observable: While on the lower side almost no vortices are detected by means of Q , various vortex cores can be observed on the upper side (Fig. 4.26d). It seems, that the proximity of the atrial wall hinders the vortex formation in this region. The patterns for ω and Q are comparable as they identify vortices predominantly at the jet boundaries. Conversely, Γ_1 does not detect any distinct vortices in the respective regions, but rather, a greatly unsteady flow is observed in the region without any regurgitant jet. Significantly, Γ_1 finds vortical structures in the lower boundary layer at the end of regurgitation, where Q levels are low.

A clear starting vortex, as observed for the generic MROPs, is not visible for the EccJet. A potential explanation is, that the PVC film's flexibility and missing inlet length of the generic MROPs enhances vortex formation. In addition, the proximity of the wall on the lower side could prevent the formation of a distinctive starting vortex ring.

To further investigate the effect of the eccentricity and the atrial wall on the vortex formation, MROPs with different eccentricities could be observed. Through that the vortex formation could be analysed dependent on the proximity to the wall.

4.3 Patient-specific Mitral Valve

The results of the most complex and realistic Mitral valve - the patient-specific Mitral valve PatSpec - are presented and discussed in this section. The PatSpec not only generates an eccentric jet, but also exhibits a more realistic opening shape attributed to the crescent shape and flexibility of the leaflets.

The medical relevance of comparing with standard fluid mechanic literature is doubtful due to the complex orifice geometry and flow situation. Therefore, examining typical free jet parameters would have limited usefulness. Instead, the emphasis is on a general understanding of the flow dynamics, including the detection of vortex structures. Similar to previous sections, this section analyses, presents, and discusses the temporal and spatial velocity distributions, along with the three-dimensional spread of the regurgitant jet and vortices.

This section provides evidence for the feasibility of the measurement and evaluation technique for patient-specific mitral valves with the heart simulator. It also offers an overview of the characteristics of a realistic regurgitant flow exceeding the information obtainable from US experiments [100, 3].

Hypotheses suggest that the most disrupted flow situation is expected when compared to previous results, due to the following characteristics of the PatSpec:

- The artificial leaflets exhibit high flexibility.
- There is a crescent-shaped opening between the leaflets.
- The bidirectional flow is enhanced due to the functioning opening-and-closing mechanism.
- The exact height, width and area of the opening causing the regurgitation are unknown.

Visual estimates indicate that the opening during regurgitation is approximately 30 mm wide and 10 mm high, resembling a half-moon shape. This would result in the orifice being the largest of all tested, leading to the lowest assumed velocity magnitudes (as a result of setting the same peak pressure in the LV for all measurements). In addition, due to the shape and opening mechanism of the leaflets, a non-circular and non-straight jet is expected. These hypotheses will be investigated as part of the flow characterisation in the following sections.

Table 4.2 compares some relevant parameters for the EccJet and the PatSpec to provide a first overview of the flow characteristic. The dimensionless quantities, as defined in Chapter 2.2.2, were calculated similar to the MROPs. For the calculation of Wo , St and Re the PatSpec's estimated width serves as the characteristic length L .

Table 4.2: Comparison of relevant parameters calculated from the phase-resolved PIV measurements in the z -plane $z = 0$ of the eccentric jet producing and patient-specific Mitral valve.

	EccJet	PatSpec
L in [mm]	8	30
$u_{\text{mag,max}}$ in [m/s]	3.45	1.57
Re [-]	8362	14260
Wo [-]	12.75	47.80
St [-]	0.0031	0.0255
$ \omega_{\text{max}} $ in [1/s]	5.1	3.4
$ Q_{\text{max}} $ in [1/s ²]	0.38	0.25

As anticipated, the maximum velocity magnitude $u_{\text{mag,max}} = 1.56$ m/s recorded is notably lower (i.e., less than half) in the case of the PatSpec compared to that in generic MROPs and EccJet (compare Table 4.1 for the values of the generic MROPs).

Regarding Re , turbulent flow according to [61] is implied. The presence of phases exhibiting nearly zero velocity magnitude (see 4.28) suggests the existence of laminar flow situations as well. As a result, transition occurs during regurgitation.

Although the PatSpec exhibits the highest Strouhal number amongst all experiments, the finding that $St = 0.0255 < 0.05$ strongly indicates a heart disease, as reported by Domenichini et al. [24].

4.3.1 Temporal Velocity Distribution

First, a visual overview of the flow situation will be presented. Figure 4.27 shows the development of the PatSpec's regurgitant jet in twelve phases ($z = 0$ plane).

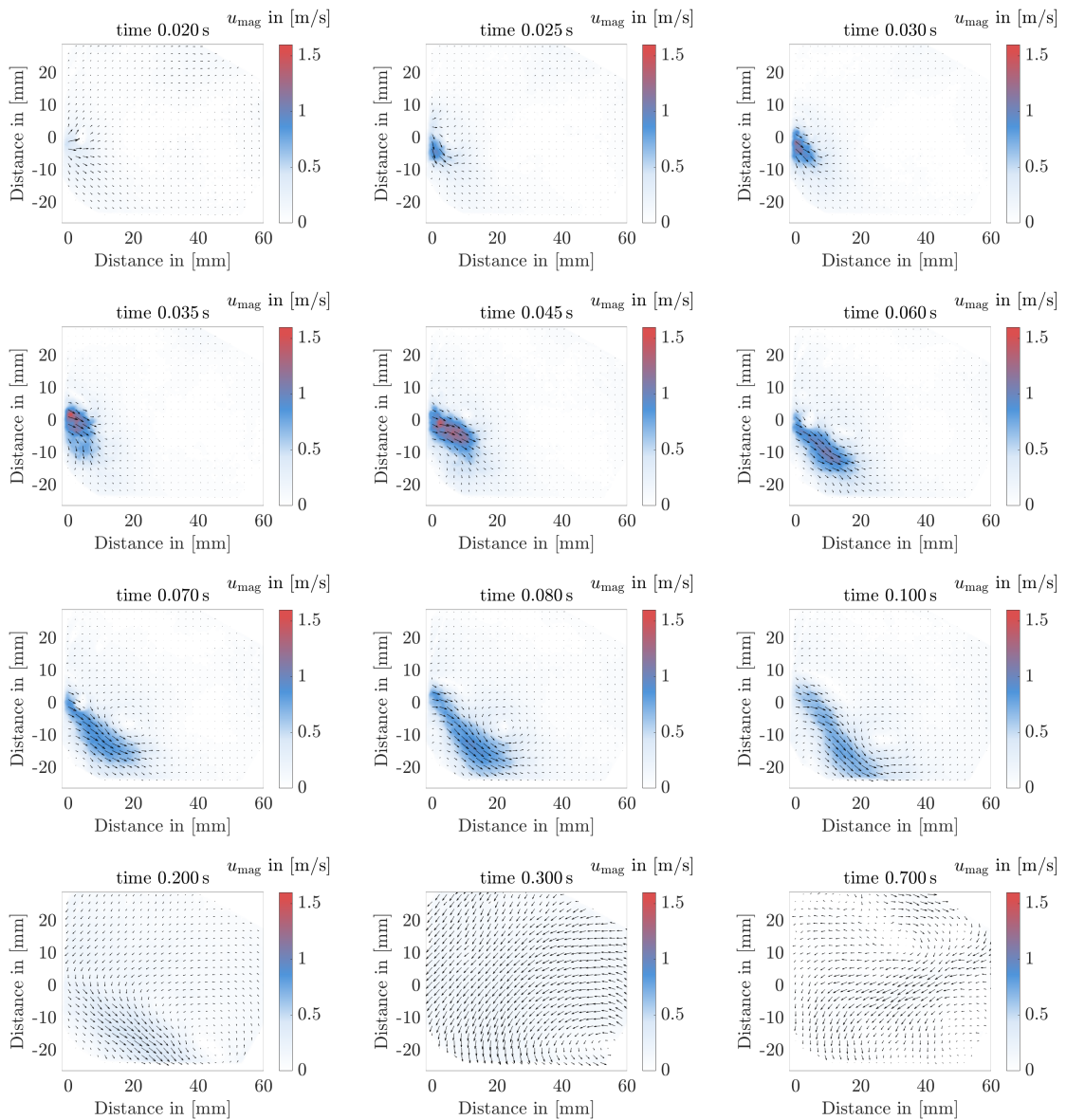


Figure 4.27: Velocity fields for selected phases of the cardiac cycle for the patient-specific Mitral valve in the $z = 0$ plane.

As anticipated, an eccentric jet can be observed. The duration of the outflow is comparable to previous findings, which can also be seen in figure 4.28. The maximum Reynolds number based on the orifice width, $Re_{\max} = 14260$, confirms the turbulent appearance of the flow. At $t = 0.300$ s the main flow direction is rotated by 90° . As the PatSpec features a opening an closing mechanism, this normal diastolic flow towards the LV is visible here as well.

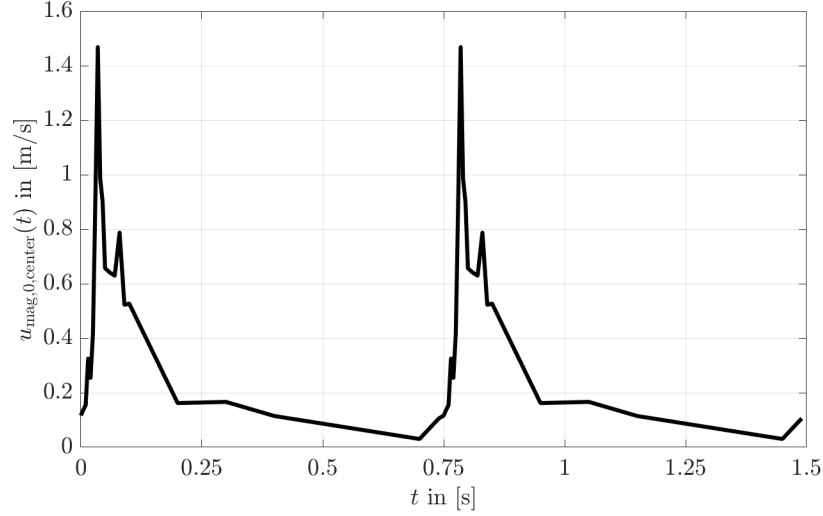
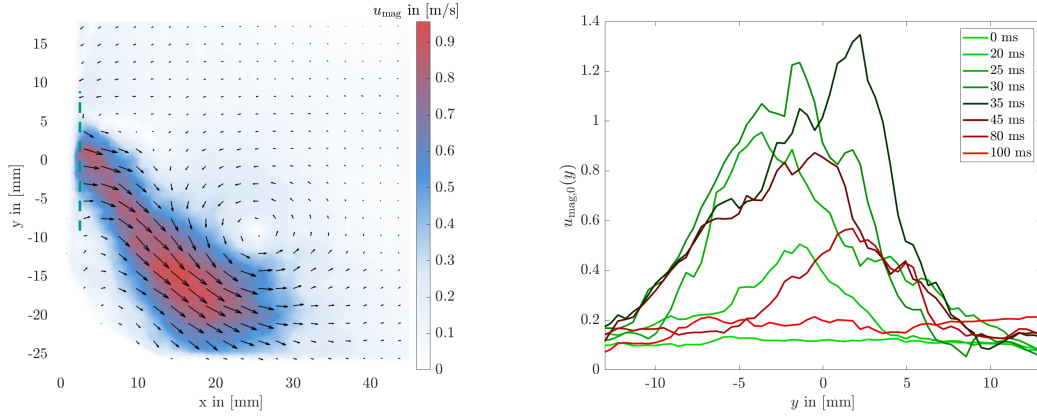


Figure 4.28: Outlet velocity magnitude $u_{\text{mag},0,\text{center}}$ for two period cycles for the patient-specific Mitral valve ($z = 0$ plane).

The flow velocity's temporal course at the outlet for two period cycles is shown in Figure 4.28. The graph displays the magnitude of the velocity $u_{\text{mag},0,\text{center}}$ rather than the x component $u_{0,\text{center}}$ to account for the non-horizontal main flow direction.

The graph demonstrates the anticipated increase and decrease of flow velocity during regurgitation, with two distinct peaks observed, the first one being higher than the second. A more bulky curve was observed for all other MROPs. Notably, the $u_{\text{mag},0,\text{center}}-t$ -graph of the PatSpec aligns much better with the output signal of the cardiac piston pump (refer to Figure 4.3a) than with the generic geometries.

The flow situation for the PatSpec is more disturbed, as evident from the vertical velocity magnitude graphs near its outlet, shown in Figure 4.29b. The graph displays eight phases that depict the increase and decrease of $u_{\text{mag},0}$. Since the dimensions of the orifice during regurgitation cannot be determined accurately, the graph is given in absolute values. Figure 4.29a presents u_{mag} in the $z = 0$ plane for $t = 80$ ms. The green dashed line illustrates the position where $u_{\text{mag},0}(y)$ is determined.



(a) Velocity magnitude u_{mag} at $t = 80$ ms including the location of the $u_{\text{mag},0}$ determination (green dashed line). (b) Temporal development of the velocity magnitude $u_{\text{mag},0}(y)$ at the outlet during regurgitation.

Figure 4.29: Overview of the velocity magnitude $u_{\text{mag},0}$ of the patient-specific Mitral valve and temporal development of the velocity magnitude at the outlet ($u_{\text{mag},0}(y)$), both for the $z = 0$ plane.

As expected, the jagged curves indicate a more disturbed flow compared to the results of the MROPs. In addition, another feature that confirms the unsteadiness of the PatSpec flow is the fluctuation of the y -position of the peak of each curve, which was not observed to the same extent for the generic MROPs. This also indicates a change in jet direction, i.e. the angle of eccentricity during regurgitation.

4.3.2 Spatial Velocity Distribution

In this section, the study aims to verify the hypothesis of a non-circular shape of the jet and provide a summary of the three-dimensional flow situation.

For the PatSpec, the laser light sheet was traversed six times to obtain seven different z -planes located at $z = -15, -10, -5, 0, +5, +10$ and $z = +15$ mm. The u_{mag} of the regurgitant jet's fully developed state at $t = 70$ ms are displayed individually for each of the seven z -planes in Figure 4.30.

The plots reveal the following observations:

- The velocity magnitude u_{mag} varies between the z -planes. There is an increase in u_{mag} for $z < 0$, while a decrease in u_{mag} is noticeable for $z > 0$.
- The jet is barely noticeable for $z = +15$ mm, whereas the greatest velocity magnitudes can be seen for $z = -10$ mm and $z = -15$ mm.
- For $z = -5$ mm, the jet appears to be straight and off-center, similar to the results for EccJet. However, for $z < -5$ mm, it appears to lay alongside the LA wall resulting in a more curved flow.
- The position of the outlet y_{outlet} changes with z , i.e. $y_{\text{outlet}}(z) \neq \text{constant}$.

4.3. Patient-specific Mitral Valve

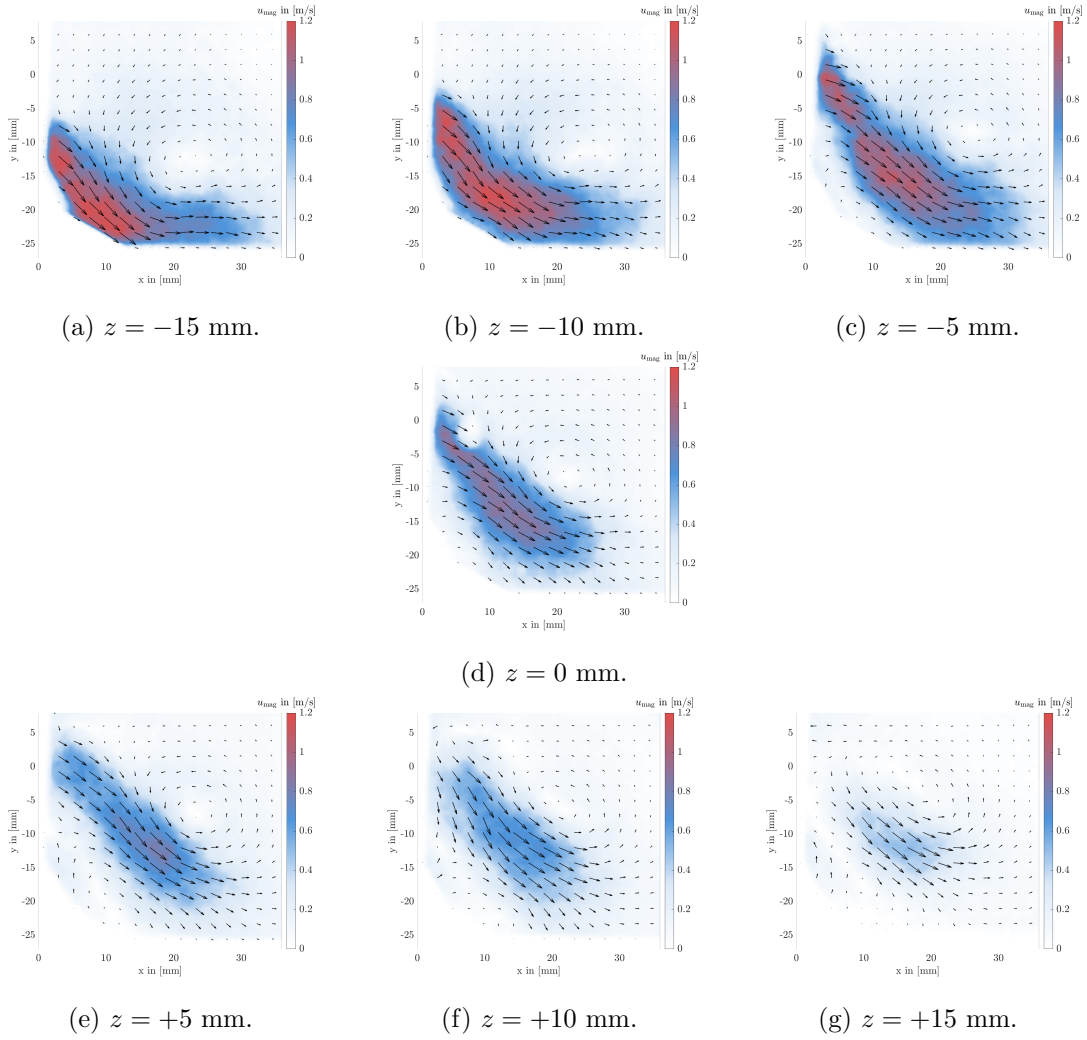


Figure 4.30: Velocity magnitude $u_{\text{mag},0}$ of the patient-specific Mitral valve in different z -planes for $t = 70$ ms.

As there is no noticeable decrease in u_{mag} at $z = -15$ mm, it is assumed, that the opening is wider than the initially estimated 30 mm. Further measurements, with the light sheet traversed to $z < -15$ mm, would be necessary to determine the opening's actual size during regurgitation. The curved flow of eccentric jets along the wall is also found in scientific publications for patient-specific regurgitant jets, e.g. [56, 15, 65, 33, 91] and is referred to as wall-hugging.

The varying y -position of the outflow supports the hypothesis of a complex orifice geometry due to the crescent shape and flexibility of the leaflets.

When examining u_{mag} for the seven z -planes at a earlier point in time, e.g. at $t = 60$ ms, notably lower u_{mag} values are observed for $z = +15$ mm. An exemplary result for $t = 60$ ms and $z = +15$ mm is depicted in Figure 4.31.

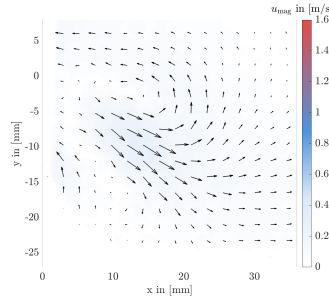


Figure 4.31: Velocity magnitude $u_{\text{mag},0}$ of the patient-specific Mitral valve for $z = +15$ mm and $t = 60$ ms.

This behaviour can be explained in two possible ways:

1. The velocity development of the jet exhibits a wave-like pattern as supported by the $u_{\text{mag}}-t$ -graph featuring two peaks (Fig. 4.28). The same wave-like course is apparent for $z = -5$ mm and $t = 70$ ms (Figure 4.30c) via a subtle shift in colour from red to blue to red along the effective center line of the jet.
2. The flow has a significant z velocity component (w), and is turned around inside the jet. The third velocity component w cannot be recovered with the 3D2C PIV setup employed in this study. Stereo PIV experiments would be necessary to retrieve such information, which is a potential next step for future experiments.

Both potential explanations suggest that the regurgitant flow of patient-specific MV is complex and highly unsteady.

Figure 4.32 provides a closer analysis of the velocity distribution in the outlet plane ($x = 0$ plane) for $t = 70$ ms. Here, the height of the surface plot visualizes the velocity magnitude in addition to the color bar.

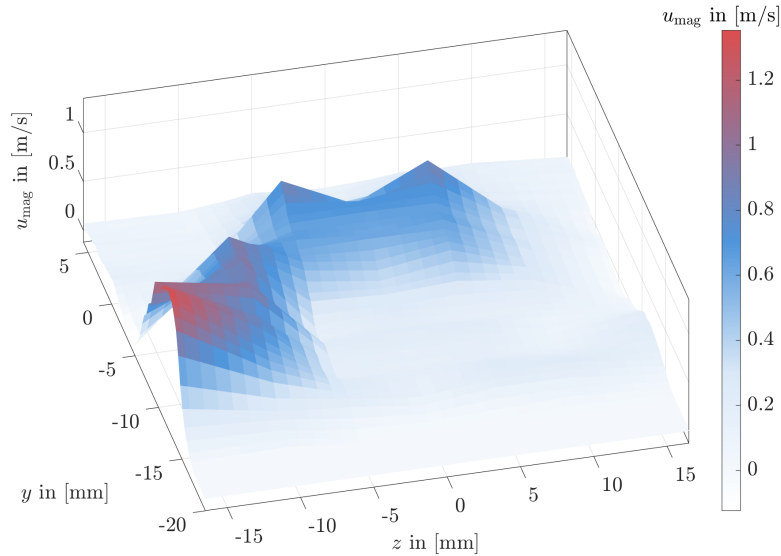


Figure 4.32: Velocity magnitude u_{mag} in the outlet plane of the patient-specific Mitral valve at $t = 70$ ms. The height of the surface plot visualizes the magnitude of the velocity in addition to the color bar.

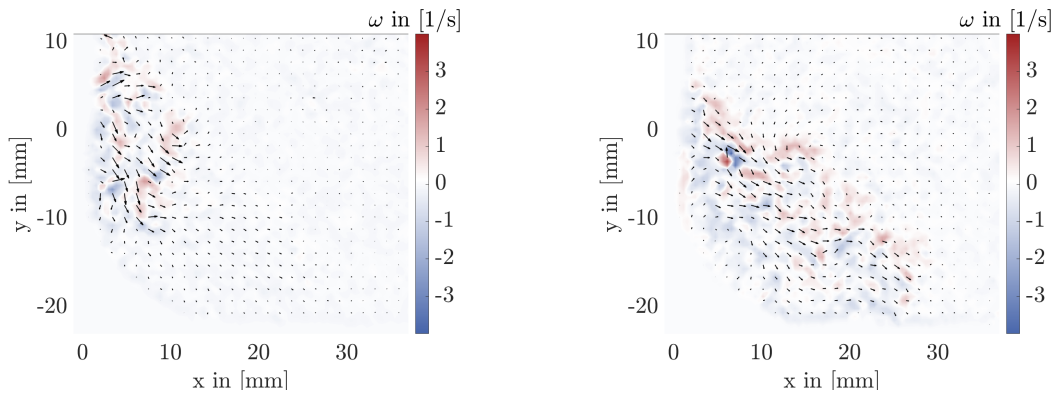
The values between the z positions, that were used in the traversed PIV measurements, are linearly interpolated. The velocity magnitude distribution observable in Figure 4.32 indicates the complex shape of the opening between the anterior and posterior leaflet. Furthermore, the observations made from Figure 4.30 can be confirmed: The highest u_{mag} values are observed for $z = -15$ mm and almost no flow velocities are detected for $z \geq 10$ mm. Although, the leaflets show a half-moon like shape, the u_{mag} distribution in the outlet plane does not show such a shape. This indicates that the closing of the PatSpec during systole works better for $z > 0$ than for $z < 0$. From a medical point of view, a potential conclusion is, that elongated chordae tendineae on one side of the MV could lead to the irregular closing of the leaflets.

4.3.3 Vortex Detection

In the following section, the vortex detection criteria Q and Γ_1 are applied to the PatSpec in addition to the vorticity analysis. Again, single image pairs are analysed first to preserve small scale effects that may be lost during in-phase averaging.

The display of the vorticity distribution shall provide a general overview of the flow situation, which can be compared to previous results in Sections 4.1.3 and 4.2.3. The Q and Γ_1 plots are provided to detect vortices in the flow. The discussion centers around the differences in vortex formation for a patient-specific case, compared to the generic ones. In addition, the quality and sensitivity of the vortex detection via Q and Γ_1 can be compared. As previously discovered by means of the velocity analysis, the PatSpec exhibits a highly unsteady flow situation. The vortex analysis aims to verify this observations. Furthermore, it is expected to detect that small-scale vortical structures in the flow field, whilst a precise detection of the starting vortex is uncertain due to the proximity of the jet to the atrial wall and the unsteady flow.

An overview of the vortex dynamical analysis is presented in Figure 4.33, showing the vorticity ω , the Q - and Γ_1 -criterion for the start and end of the regurgitation, respectively.



(a) Vorticity ω beginning of regurgitation.

(b) Vorticity ω end of regurgitation.

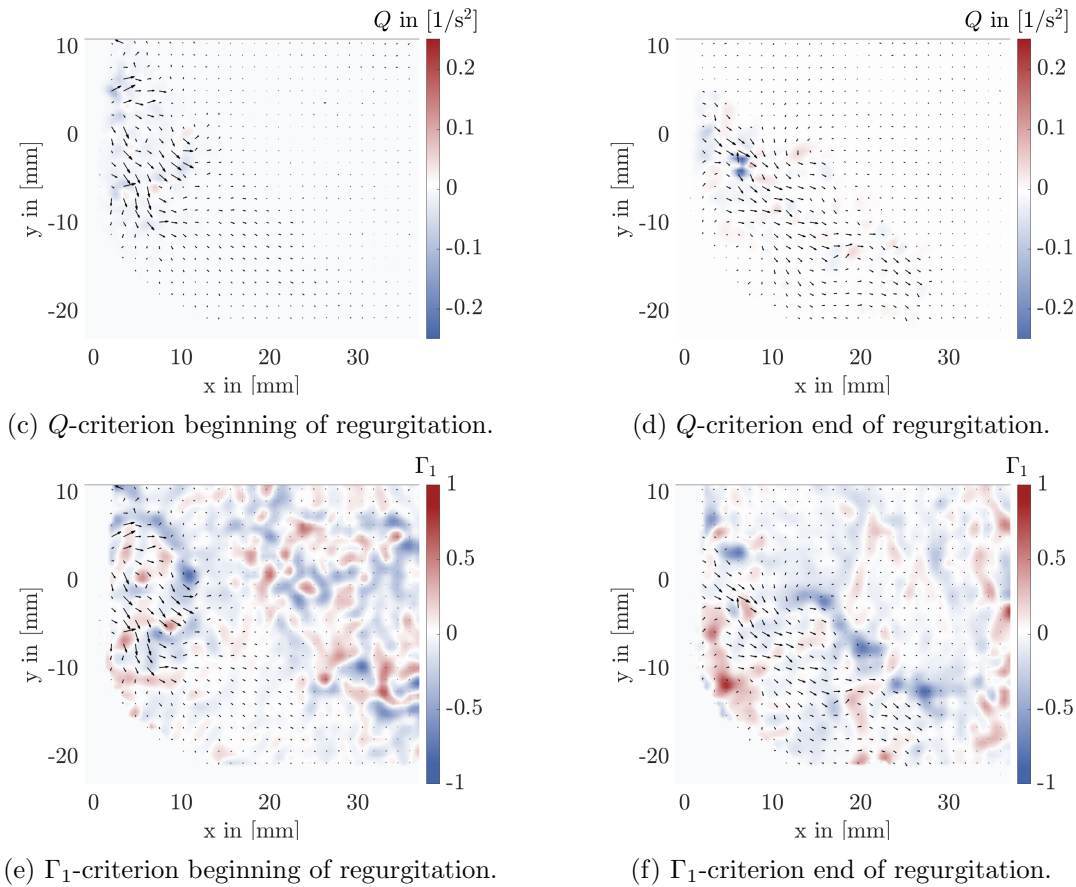


Figure 4.33: Vorticity and vortex detection by means of the Q - and Γ_1 -criterion for the patient-specific Mitral valve. The left side shows the time of emergence of the jet ($t = 30$ ms), while the right side shows the end of regurgitation ($t = 70$ ms), both for $z = 0$.

The distribution of the vorticity ω shows comparable pattern to those obtained for the EccJet, while vorticity magnitudes are slightly lower. Due to the larger opening area of the PatSpec the velocity magnitude is lower (see 4.2), compared to the other MVs investigated. As the vorticity and velocity are linked via the cross product (please refer to the definition of the vorticity Eq. 2.18), lower velocity magnitudes lead to lower ω values for similar flow situations. Contrary to the results of the generic MROPs and the EccJet, the vorticity is more distributed over the whole jet region. This indicates a disturbed flow situation not only in the boundary layer, but also inside the jet.

The Q -criterion does not detect a clear starting vortex for the beginning of the regurgitation. At the end of regurgitation, vortex cores are detected along the jet, but not necessarily in the regions of the expected shear layer, as for the generic MROPs. This supports the thesis of an increased unsteadiness inside the jet flow.

The Γ_1 -criterion identifies vortices at the beginning of the regurgitation. Nonetheless, a definite starting vortex cannot be determined via the single image pair evaluation. Furthermore, multiple vortical structures are identified in the surrounding region of the jet, similar to the findings for the EccJet. From this, it can be concluded that the flow state within the jet is more disturbed and unsteady than in previous measurements, and the flow state outside is also significantly disturbed during regurgitation. In addition to the more disturbed jet, the amplified bidirectional flow of the PatSpec could potentially account for this finding.

At the end of regurgitation (Fig. 4.33f) less vortices are identified by means of Γ_1 in the

surrounding region of the jet. As Γ_1 is a relative measure, it can be concluded, that at the beginning of regurgitation, the intensity of the vortical structures inside the jet do not exceed the ones in the surrounding regions. Thus, vortical structures in the jet and in the surrounding regions are equally visible. At the end of the regurgitation, however, the Γ_1 values in the boundary layer of the jet exceed those in the surrounding region and are therefore clearly visible. Thus, the vortices in the boundary layer are the dominant phenomena at the end of the regurgitation.

Particularly visible are the blue regions on the upper side of the jet, indicating counterclockwise rotating areas within the flow field. On the lower side of the jet, the red areas, which indicate clockwise rotating parts, are visible only at the beginning of the jet. This may be due to the proximity of the wall leading to the dissipation of vortical structures in that region. In addition, the limited fluid entrainment potential due to the wall-hugging could hamper the vortex roll-up (as there is less surrounding fluid on that side).

While for the previously analysed generic cases, Q seemed to perform better in terms of vortex detection, Γ_1 provides clearer results for the PatSpec. A potential explanation for the different performance of two criteria is the unsteadiness of the flow situation. The Q -criterion is based on velocity gradient calculation (see Chapter 2.2.3), which can be difficult for noisy or unsteady experimental data, like observed for the PatSpec. In contrast, the calculation of Γ_1 does not depend on gradients making it more robust.

Based on the velocity plots for the PatSpec, the flow situation for $z < 0$ suggests a large-scale vortex on the upper side of the jet (see Fig. 4.30, which potentially is a consequence of the eccentric jet flow). In the following this observation is further investigated by applying the vortex detection criteria on the flow fields for the same time step $t = 70$ ms and the $z = -5$ mm plane. Figure 4.34 compares the Γ_1 results of a single image pair evaluation with the ones for a in-phase averaged evaluation of 40 image pairs for the same time and z -location.

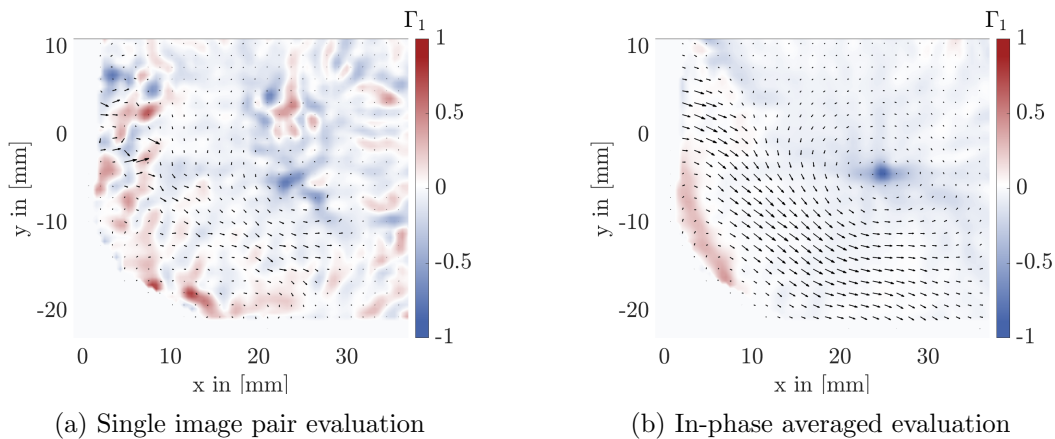


Figure 4.34: Comparison of the Γ_1 application on the flow field for $t = 70$ ms and $z = -5$ mm for (a) a single image pair and (b) 40 in-phase averaged image pairs.

The single image pair evaluation shows similar results as for the $z = 0$ plane in 4.33f: The flow situation is unsteady with various small-scale vortices detectable inside the jet and on the boundaries. The large-scale vortex, which is assumed based on the velocity plots (see Figs 4.30(a)-(c)) cannot be detected distinctively.

In contrast, the Γ_1 -criterion applied to the evaluation of the in-phase averaged image pairs clearly shows the expected counterclockwise vortex on the upper side of the jet. On the lower boundary layer side of the jet, clockwise rotating structures are detected along the

atrial wall. Due to averaging, the appearance is blurred and no distinct vortex core can be identified. It is clear from figure 4.34b that the unsteadiness and small scale structure disappear due to the in-phase averaging and only the dominant fluid mechanical phenomena are detectable.

In conclusion, for similar future investigations with disturbed and unsteady flow situations it is recommended, to work with single image pairs in case the small-scale vortices are of interest and use in-phase averaged evaluations to characterize the predominant large-scale phenomena in the flow.

Thus, the investigation of the starting vortex formation and development for the PatSpec is presented with in-phase averaged PIV evaluations. The results of the Γ_1 -criterion for six time steps in the $z = 0$ plane are presented in Figure 4.35 below.

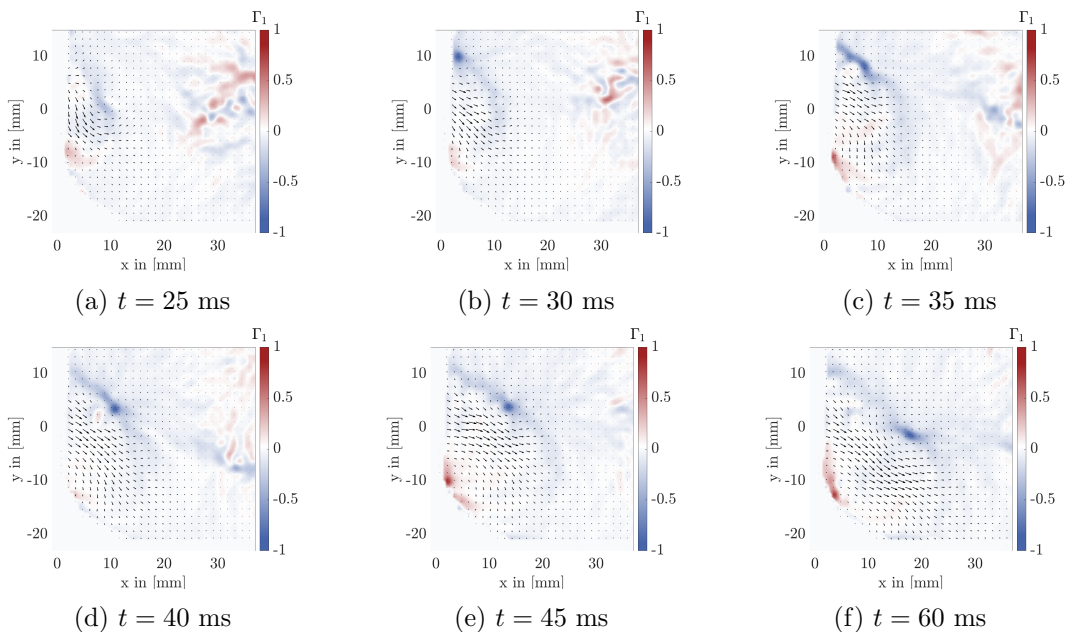


Figure 4.35: Γ_1 -criterion applied on in-phase averaged PIV evaluations of the patient-specific Mitral valve at $z = 0$ for six time steps during regurgitation.

It can be observed that prior to the appearance of a distinct vortex, a less prominent pair of vortices is visible at $t = 25$ ms (Fig. 4.35a), which disappears as the clear starting vortex appears at $t = 30$ ms. The starting vortex pair moves in parallel with the jet, similar to the generic MROPs, but skewed due to the eccentricity of MR. It is worth noting that while the vortex core on the upper side traces a fairly straight line, the one on the lower side tends to hug the atrial wall. Furthermore, the velocity of the lower side vortex core seems to be less than that of the upper side. The tendency of the jet to remain attached to the wall, commonly known as the Coanda effect, is frequently observed in eccentric MR and is associated with a significant risk of underestimation by standard quantification methods [27, 33, 91].

Future research should consider utilizing FTLE-based vortex detection methods to better comprehend the cause-and-effect relationship of vortex development in proximity to the LA wall. Furthermore, the incorporation of a metric to measure the wall impingement in the evaluation process has the potential to assess the underestimation of evaluations based on TEE.

5. Conclusion and Outlook

Mitral regurgitation is a prevalent valvular disease in the global population [66, 86]. The treatment heavily relies on accurate diagnosis [15, 28]. However, commonly used medical diagnostic techniques can lead to inaccurate assessments due to a variety of limitations [19, 100, 31, 29]. This study aims to enhance current diagnosis techniques by advancing the understanding of the fluid dynamics of the regurgitant jet.

The experimental setup for Particle Image Velocimetry (PIV) measurements on a heart simulator was prepared as part of this work. The 3D printed heart simulator was filled with a seeded transparent blood mimic enabling the optical access for the camera and necessary laser light scattering. The experiments involved using various generic Mitral regurgitation orifice phantoms, a eccentric jet generating Mitral regurgitation phantom and a patient-specific Mitral valve. Three different orifice shapes - a pinhole, a pointed oval shape (slot), and a drop shape - were selected as the generic geometries. Thin PVC film was used to create Mitral regurgitation orifice phantoms that mimic the flexibility of real heart valves. To induce eccentric regurgitation, an Mitral regurgitation orifice phantom was 3D printed with an eccentricity of 30° to the centre line and an inlet length of 12 cm, forcing the flow to deviate from the centre. The patient-specific Mitral valve was designed by [10] to match the anatomy and mechanical properties of an authentic mitral valve. Phase-averaged and phase-resolved measurements were conducted for every shape. For non-axisymmetric shapes, the laser light sheet was traversed perpendicular to the main flow direction to collect quasi three-dimensional velocity information. In order to quantify the results of the PIV experiments and to compare them with the current scientific literature, post-processing methods were developed and established. Furthermore, particular focus was directed towards identifying vortices in the flow, as they represent dominating flow characteristics in cardiac flow. Therefore, the vortex detection methods Q and Γ_1 were implemented in the post-processing scripts.

The outcomes of the **generic Mitral regurgitation orifice phantoms** were largely in alignment with the scientific literature on pulsating free jets. The potential core length and axial velocity behaved as anticipated. The center line velocity's evolution over time at the outlet exhibited a typical graph with two peaks per heartbeat. The movement of the cardiac piston pump can be linked to this phenomenon, which imitates the human heartbeat and produces two consecutive peaks during the contraction of the left ventricle. The outlet velocity has characteristic saddle-backed radial profiles, which can be attributed

to the sharp edges and missing inlet length of the PVC film orifices [23, 74]. For the drop and the slot the aspect ratios might intensify the effect [85, 74]. The inner shape of the heart simulator’s left atrium, has an influence on the regurgitant jet that is different from the standard cases in the literature, as the velocity decay and spreading for the far field cannot be compared. Additionally, the left atrium size and consequential wall-impingement of the jet might explain the characteristic saddle-backed outlet profiles [45] as well. To link the effect to one of the potential explanation further parameter studies are necessary, varying only one orifice property at a time.

Comparing the shape of the outlet velocity profiles for the three generic shapes a clear distinction was observable. Compared to the pinhole, more bulky profiles for slot shaped orifices and asymmetric profiles for the drop shaped profiles, were identified. Those findings could potentially support the ultrasound diagnosis in determining the geometry of the valve defect.

For the non-axisymmetric Mitral regurgitation orifices, the drop and slot a clear influence of the orifice shape on the spreading and velocity profiles was observed. In the jet’s near field, the regurgitant flow’s propagation perpendicular to the main flow direction corresponds to the orifice shape. However, as the distance from the jet increases, the flow tends to adopt a circular shape. In terms of ultrasound measurements, it is therefore advisable to set the Nyquist limit to lower values for non-circular orifices, as this would lead to a determination of the aliasing velocity and PISA radius at a greater distance from the opening, where rather hemispheric convergence of the flow is assumed.

The larger velocity profiles along the longer dimension of the slot exhibit similarities to examples of plane or rectangular jets found in literature [74, 40, 85]. This supports the literature on the limitations of ultrasound-based assessment methods for non-circular mitral valve defects. In case the ultrasound image plane does not coincide with the orifice’s long dimension, the severity is prone to be underestimated.

Asymmetric velocity profiles are observed in the outlet plane perpendicular to the flow and in the planes in the flow direction, in the case of the drop. The increased complexity in the regurgitant flow leads to a higher likelihood of errors in the 1D velocity measurement within the commonly used ultrasound imaging technology’s 2D planes. This limitation significantly reduces the significance of ultrasound-based evaluation for complex orifice shapes.

The results of the vortex detection show a powerful leading vortex pair, followed by Kelvin-Helmholtz instabilities in the boundary layer upstream. In line with the development of temporal velocity, a few orifices display an additional ”leading” vortex pair, which is probably due to the double peaks characteristic of the cardiac piston pump.

Furthermore, a strong decrease in vorticity is observed when the both leading vortex pairs hit the opposite left atrium wall respectively. To gain a thorough understanding of this phenomena, more detailed measurements exceeding the temporal and local resolution of this study are required.

As anticipated, the study of the eccentric jet exhibited significant similarity to the non-eccentric jet, when rotated by 30° . Nonetheless, the saddle-backed radial profiles at the outlet were not observed in the eccentric jet. This suggests that the sharp edges of the thin film, and the lack of inlet length, are responsible for the saddle-backed shape of the radial profiles of axial velocity. Although noted as a common occurrence in scientific literature on MR [29, 37, 27, 91], no ”hugging” of the atrial wall was observed for the eccentric jet. Future studies should conduct similar measurements for greater eccentricities of the Mitral regurgitation orifice phantom to investigate further.

In addition, the regurgitation phantom producing the eccentric jet showed less intense vortices. One possible explanation is that the varying inlet lengths and material properties of the rigid 3D printed phantom compared to the thin and flexible ones may affect the

formation of the vortex. Conducting further measurements that incorporate different inlet lengths and material properties could be the subsequent course of action to investigate these dissimilarities.

The primary difference in the regurgitant flow of the **patient-specific Mitral valve** is the more distorted and turbulent velocity field. This can be attributed to the valve's more complex opening shape and the higher Reynolds number observed. The temporal velocity graph near the outlet showed a strong alignment with the piston's travel over time function of the cardiac pump. The crescent-shaped opening between the Mitral valve leaflets is reflected in the three-dimensional shape of the regurgitant jet. The varying flow conditions of the jet in different planes make the ultrasound-based severity assessment questionable due to its two-dimensional limitation. This is not only due to differences in velocity magnitude, but also in the jet's shape and duration of occurrence. Some planes exhibit straight eccentric jets, while others show eccentric jets that hug the atrial wall.

When it comes to vortex detection based on single image pairs, the criteria used, did identify vortices in the flow field, but not as clearly as they did for generic Mitral regurgitation orifice phantoms. Different intensities and positions of vortical structures have been identified in various traversing planes indicating a unsteady flow situation. Vortex detection based on in-phase averaged PIV evaluations provided clear results regarding large-scale phenomena. Specifically the formation and development of the starting vortex on the free shear layer side of the jet was observed. On the side of the atrial wall, wall-hugging of the jet could be noted. For similar future investigations it is recommended, to analyse single image pairs in case the small-scale vortices are of interest and use in-phase averaged evaluations to identify large-scale phenomena in the flow.

To address the highly distorted and complex flow situation of the patient-specific mitral valve regurgitant jet, further PIV measurements are proposed. On one hand, a higher spatial resolution of the light sheet traversal would allow a more comprehensive understanding of the three-dimensional shape of the jet. On the other hand, stereo PIV measurements in the left atrium of the heart simulator could provide further improvements, including the three-dimensional velocity field. Furthermore, a Lagrangian approach could be implemented in the post-processing to investigate cause-effect relationships, e.g. a Finite Time Lyapunov Exponent (FTLE) evaluation. Therefore, it is advisable to perform time-resolved PIV experiments to enhance the temporal density of the acquired velocity information.

A potential next step for the heart simulator is to incorporate a more realistic design of the left atrium's inner shape, to observe the influence of natural geometry on jet formation. In addition, the significance of inflow conditions of the regurgitant jet could be increased by including a realistic shape for the left ventricle. The key challenges lie in the alteration of the heart chamber's contour throughout the cardiac cycle, i.e. contraction, dilatation and relaxation, and in the optical accessibility for particle image velocimetry.

One valuable next step in establishing a connection between fluid dynamics phenomena and Mitral regurgitation types is to investigate Mitral valves with diverse damages and compare their respective flow dynamics. To initiate the development of insufficient Mitral valves, which have different causation, the functional classification of Mitral regurgitation suggested by Carpentier [15] (Fig. 2.6) could serve as a starting point. A comparison of the fluid dynamic observations using particle image velocimetry could yield valuable insights that may be integrated in the analysis of ultrasound images.

In conclusion, this study examines the feasibility of using particle image velocimetry to measure flows within a heart simulator. The results confirm the complex flow situation for

regurgitant jets. By employing the developed post-processing methods, the understanding of the flow dynamics of the regurgitant jet, especially for complex orifices, has been improved. Furthermore, this thesis assesses the performance of different vortex detection criteria for complex hemodynamic flows and indicates potential next steps.

Bibliography

- [1] Vouros Alexandros, Th Panidis, A. Pollard, and Rainer Schwab. Near field vorticity distributions from a sharp-edged rectangular jet. *International Journal of Heat and Fluid Flow*, 51, 10 2014.
- [2] Anne Amblard, H el ene Berre, Benyebka Bou-Sa id, and Michel Brunet. Analysis of type i endoleaks in a stented abdominal aortic aneurysm. *Medical engineering & physics*, 31:27–33, 06 2008.
- [3] Efstratios Apostolakis and Nikolaos Baikoussis. Methods of estimation of mitral valve regurgitation for the cardiac surgeon. *Journal of cardiothoracic surgery*, 4:34, 08 2009.
- [4] Nicolas Aristokleous. *Effects of Posture Change on the Geometry and Hemodynamics of the Human Carotid Bifurcation* Nicolas Aristokleous. PhD thesis, Lund University, 07 2013.
- [5] H Baieth. Physical parameters of blood as a non - newtonian fluid. *International journal of biomedical science : IJBS*, 4:323–329, 12 2008.
- [6] C.G. Ball, H. Fellouah, and A. Pollard. The flow field in turbulent round free jets. *Progress in Aerospace Sciences*, 50:1–26, 2012.
- [7] G. K. Batchelor. *An introduction to fluid dynamics*. Cambridge University Press,, London, 1967.
- [8] H. A. Becker and T. A. Massaro. Vortex evolution in a round jet. *Journal of Fluid Mechanics*, 31(3):435–448, 1968.
- [9] Lorenzo Bennati, Vincenzo Giambruno, Francesca Renzi, Venanzio Di Nicola, Caterina Maffei, Giovanni Puppini, Giovanni Battista Luciani, and Christian Vergara. Turbulence and blood washout in presence of mitral regurgitation: a computational fluid-dynamics study in the complete left heart. *bioRxiv*, 2023.
- [10] Carl S oren Bergt. Development and manufacturing of artificial patient-specific mitral valves for surgery preparation by using the thermoforming process, 2023.
- [11] Nikolai Bessonov, Ad elia Sequeira, Sergey Simakov, Yu Vassilevskii, and Vitaly Volpert. Methods of blood flow modelling. *Mathematical Modelling of Natural Phenomena*, 11:1–25, 01 2016.
- [12] F. Billy, D. Coisne, L. Sanchez, and R. Perrault. The Mitral Valve Prolapsus: Quantification of the Regurgitation Flow Rate by Experimental Time-Dependant PIV. Conference Paper, AD-A409547, October 2001.
- [13] Martin B usen, Tim Kaufmann, Michael Neidlin, Ulrich Steinseifer, and Simon Sonntag. In vitro flow investigations in the aortic arch during cardiopulmonary bypass with stereo-piv. *Journal of biomechanics*, 48, 04 2015.

- [14] Blase A. Carabello and Fred A. Crawford. Valvular heart disease. *New England Journal of Medicine*, 337(1):32–41, 1997. PMID: 9203430.
- [15] A. Carpentier, D.H. Adams, and F. Filsoofi. *Carpentier’s Reconstructive Valve Surgery*. Elsevier Health Sciences, 2010.
- [16] Jianlong Chang, Shizhen Zheng, Yang Du, Junjie Xu, Yanchen Liu, Baoquan Guo, Yutian Pan, and Bing Han. Investigation of vortex rings for free jet and synthetic jet at various reynolds numbers and strouhal numbers. *Mathematical Problems in Engineering*, 2020:1–15, 08 2020.
- [17] M. S. Chong, A. E. Perry, and B. J. Cantwell. A general classification of three-dimensional flow fields. *Physics of Fluids A: Fluid Dynamics*, 2(5):765–777, 05 1990.
- [18] Isaac Choutapalli, A. Krothapalli, and J. ARAKERI. An experimental study of an axisymmetric turbulent pulsed air jet. *Journal of Fluid Mechanics*, 631:23 – 63, 07 2009.
- [19] Damien Coisne, Donal Erwan, Luc Christiaens, Pascal Blouin, Jose Allal, and Robert Barraine. Quantitative assessment of regurgitant flow with total digital three-dimensional reconstruction of color doppler flow in the convergent region: In vitro validation. *Journal of the American Society of Echocardiography*, 15(3):233–240, 2002.
- [20] Megan Cooke and Derek Rosenzweig. The rheology of direct and suspended extrusion bioprinting. *APL Bioengineering*, 5:011502, 03 2021.
- [21] Benoit Cushman-Roisin. Kelvin–helmholtz instability as a boundary-value problem. *Environmental Fluid Mechanics*, 5:507–525, 12 2005.
- [22] Anna Christina Daub. *Numerical Haemodynamics in the Human Heart*. PhD thesis, Karlsruher Institut für Technologie (KIT), 2018.
- [23] Ravinesh C. Deo, Jianchun Mi, and Graham J. Nathan. The influence of nozzle-exit geometric profile on statistical properties of a turbulent plane jet. *Experimental Thermal and Fluid Science*, 32(2):545–559, 2007.
- [24] Federico Domenichini, Gianni Pedrizzetti, and Baccani B. Three-dimensional filling flow into a model left ventricle. *Journal of Fluid Mechanics*, 539:179–198, 09 2005.
- [25] Steven Douedi and Hani Douedi. *Mitral Regurgitation*. 01 2020.
- [26] P.G. Drazin. Dynamical meteorology | kelvin–helmholtz instability. In Gerald R. North, John Pyle, and Fuqing Zhang, editors, *Encyclopedia of Atmospheric Sciences (Second Edition)*, pages 343–346. Academic Press, Oxford, second edition edition, 2015.
- [27] Chris F. Duncan, Emma Bowcock, Faraz Pathan, and Sam R. Orde. Mitral regurgitation in the critically ill: the devil is in the detail. *Annals of Intensive Care*, 13(1):67, Aug 2023.
- [28] Abdallah El Sabbagh, Yogesh N.V. Reddy, and Rick A. Nishimura. Mitral valve regurgitation in the contemporary era: Insights into diagnosis, management, and future directions. *JACC: Cardiovascular Imaging*, 11(4):628–643, 2018.
- [29] Maurice Enriquez-Sarano, A.Jamil Tajik, Kent R. Bailey, and James B. Seward. Color flow imaging compared with quantitative doppler assessment of severity of mitral régurgitation: Influence of eccentricity of jet and mechanism of regurgitation. *Journal of the American College of Cardiology*, 21(5):1211–1219, 1993.

- [30] Daniel Espino, Duncan Shepherd, and David Hukins. Evaluation of a transient, simultaneous, arbitrary lagrange–euler based multi-physics method for simulating the mitral heart valve. *Computer methods in biomechanics and biomedical engineering*, 17, 05 2012.
- [31] Christian Frerker, Nicole Karam, Rebecca Hahn, Holger Thiele, Gregg Stone, Hendrik Treede, and Jörg Hausleiter. New esc/eacts guideline recommendations for treatment of secondary mitral regurgitation: Reflections on the evidence. *European Journal of Heart Failure*, 24, 04 2022.
- [32] J.W. Gauntner, J.N.B. Livingood, P. Hrycak, United States. National Aeronautics, Space Administration, and Lewis Research Center. *Survey of Literature on Flow Characteristics of a Single Turbulent Jet Impinging on a Flat Plate*. NASA technical note. National Aeronautics and Space Administration, 1970.
- [33] Carmen Gingham. The coanda effect in cardiology. *J Cardiovasc Med Italian Federation of Cardiology. Journal of Cardiovascular Medicine*, 8:411–413, 06 2007.
- [34] Laurent Graftieaux, Marc Michard, and Nathalie Grosjean. Combining piv, pod and vortex identification algorithms for the study of unsteady turbulent swirling flows. *Measurement Science and Technology*, 12:1422, 08 2001.
- [35] Lew Gramer. *Kelvin-Helmholtz Instabilities*. Lew & Gov, 05 2007.
- [36] Sheldon I Green. *Fluid Vortices*. Fluid mechanics and its applications. Kluwer, Dordrecht, 1995.
- [37] F Helmcke, N C Nanda, M C Hsiung, B Soto, C K Adey, R G Goyal, and R P Gatewood. Color doppler assessment of mitral regurgitation with orthogonal planes. *Circulation*, 75(1):175–183, 1987.
- [38] Gerd Herold. *Innere Medizin*. Gerd Herold, Köln, 2019.
- [39] Katsuya Hirata, Tatuya Kubo, Yasutaka Hatanaka, Masamitsu Matsushita, Kazuaki Shobu, and Jiro Funaki. An Experimental Study of Amplitude and Frequency Effects upon a Pulsating Jet. *Journal of Fluid Science and Technology*, 4(3):578–589, January 2009.
- [40] J. Hunt, Alan Wray, and Parviz Moin. Eddies, streams, and convergence zones in turbulent flows. *Studying Turbulence Using Numerical Simulation Databases*, -1:193–208, 11 1988.
- [41] A. K. M. F. Hussain and K. B. M. Q. Zaman. The ‘preferred mode’ of the axisymmetric jet. *Journal of Fluid Mechanics*, 110:39–71, 1981.
- [42] Fazle Hussain. Elliptic jets. part 1. characteristics of unexcited and excited jets. *Journal of Fluid Mechanics*, 208:257 – 320, 11 1989.
- [43] Hussein J. Hussein, Steven P. Capp, and William K. George. Velocity measurements in a high-reynolds-number, momentum-conserving, axisymmetric, turbulent jet. *Journal of Fluid Mechanics*, 258:31–75, 1994.
- [44] Andrea Natale Impiombato, Giorgio La Civita, Francesco Orlandi, Flavia Schwarz Franceschini Zinani, Luiz Alberto Oliveira Rocha, and Cesare Biserni. A simple transient poiseuille-based approach to mimic the womersley function and to model pulsatile blood flow. *Dynamics*, 1(1):9–17, 2021.
- [45] Nick Jeffers, Jason Stafford, Ciaran Conway, Jeff Punch, and Edmond Walsh. The influence of the stagnation zone on the fluid dynamics at the nozzle exit of a confined and submerged impinging jet. *Experiments in Fluids*, 57, 01 2016.

- [46] Morteza Jeyhani, Shahrokh Shahriari, and Michel Labrosse. Experimental investigation of left ventricular flow patterns after percutaneous edge-to-edge mitral valve repair: Flow patterns after edge-to-edge mitral valve repair. *Artificial Organs*, 42, 11 2017.
- [47] Roger Karl, Robin Leister, Lubov Stroh, Mereles Derliz, Eden Matthias, Luis Neff, Raffaele de Simone, Gabriele Romano, Alexander Stroh, Jochen Kriegseis, Matthias Karck, Norbert Frey, Bettina Frohnepfel, and Sandy Engelhardt. Comparison of transesophageal echocardiography and particle image velocimetry to quantify mitral regurgitation in an high-fidelity environment. *TBD*, 2023.
- [48] Roger Frederik Karl. *Patient-specific hemodynamic simulators for cardiovascular therapies*. PhD thesis, Ruprecht-Karls-Universität, 2023.
- [49] Nikolaos D. Katopodes. Chapter 5 - viscous fluid flow. In Nikolaos D. Katopodes, editor, *Free-Surface Flow*, pages 324–426. Butterworth-Heinemann, 2019.
- [50] Nikolaos D. Katopodes. Chapter 6 - ideal fluid flow. In Nikolaos D. Katopodes, editor, *Free-Surface Flow*, pages 428–515. Butterworth-Heinemann, 2019.
- [51] V Kini, Claire Bachmann, Arnold Fontaine, S Deutsch, and John Tarbell. Integrating particle image velocimetry and laser doppler velocimetry measurements of the regurgitant flow field past mechanical heart valves. *Artificial organs*, 25:136–45, 03 2001.
- [52] R. Klinke, H.C. Pape, A. Kurtz, and S. Silbernagl. *Physiologie*. Georg Thieme Verlag, 2009.
- [53] Rüdiger Kramme. *Medizintechnik*, volume 4. Springer Berlin Heidelberg, 2017.
- [54] Jochen Kriegseis. Vorlesung wirbeldynamik. Technical report, Karlsruhe Institute of Technology, 2021.
- [55] Florian Lang. Basiswissen physiologie, 2007.
- [56] Gabriel S. Levi, Steven F. Bolling, and David S. Bach. Eccentric mitral regurgitation jets among patients having sustained inferior wall myocardial infarction. *Echocardiography*, 18(2):97–103, 2001.
- [57] Quan Long, R Merrifield, Xiao Xu, Philip Kilner, David Firmin, and Yang G-Z. Subject-specific computational simulation of left ventricular flow based on magnetic resonance imaging. *Proceedings of the Institution of Mechanical Engineers. Part H, Journal of engineering in medicine*, 222:475–85, 06 2008.
- [58] Xingyu Ma, Xuan Gong, and Nan Jiang. Experimental study of vortex formation in pulsating jet flow by time-resolved particle image velocimetry. *Physics of Fluids*, 34(3):035105, 03 2022.
- [59] Keefe Manning, Vinayak Kini, Arnold Fontaine, Steven Deutsch, and John Tarbell. Regurgitant flow field characteristics of the st. jude bileaflet mechanical heart valve under physiologic pulsatile flow using particle image velocimetry. *Artificial organs*, 27:840–6, 10 2003.
- [60] G.F. Marsters and J. Fotheringham. The influence of aspect ratio on incompressible, turbulent flows from rectangular slots. *Aeronautical Quarterly*, 31(4):285–305, 1980.
- [61] K. J. Mcnaughton and C. G. Sinclair. Submerged jets in short cylindrical flow vessels. *Journal of Fluid Mechanics*, 25(2):367–375, 1966.
- [62] Blausen Medical. Medical gallery of blausen medical 2014. *WikiJournal of Medicine*, 1(2):1–79, 2014.

- [63] Jiaxing Mi and Graham Nathan. Statistical properties of turbulent free jets issuing from nine differently-shaped nozzles. *Flow, Turbulence and Combustion*, 84:583–606, 06 2010.
- [64] A. Michalke. The instability of free shear layers. *Progress in Aerospace Sciences*, 12:213–216, 1972.
- [65] Michela Moraldo, Fabrizio Cecaro, Matthew Shun-Shin, Punam Pabari, Justin Davies, Xiao Xu, Alun Hughes, Charlotte Manisty, and Darrel Francis. Evidence-based recommendations for pisa measurements in mitral regurgitation: Systematic review, clinical and in-vitro study. *International journal of cardiology*, 168, 12 2012.
- [66] Vuyisile T Nkomo, Julius M Gardin, Thomas N Skelton, John S Gottdiener, Christopher G Scott, and Maurice Enriquez-Sarano. Burden of valvular heart diseases: a population-based study. *Lancet (London, England)*, 368(9540):1005–1011, September 2006.
- [67] David Nordsletten, M. McCormick, Philip Kilner, P. Hunter, David Kay, and N. Smith. Fluid–solid coupling for the investigation of diastolic and systolic human left ventricular function. *International Journal for Numerical Methods in Biomedical Engineering*, 27:1017 – 1039, 07 2011.
- [68] Herbert Oertel. Modelling the human cardiac fluid mechanics. *Modelling the Human Cardiac Fluid Mechanics*, 01 2005.
- [69] Herbert Oertel and Jan Delfs. *Strömungsmechanische Instabilitäten. Originalveröffentlichung. im Springer-Verl., Berlin, 1996.* Universitätsverlag Karlsruhe, 2005.
- [70] Catherine M. Otto. Evaluation and management of chronic mitral regurgitation. *New England Journal of Medicine*, 345(10):740–746, 2001. PMID: 11547744.
- [71] Paul Y. Paik, Michelle Capdeville, and Andra E. Duncan. Turbulence in the left ventricular outflow tract caused by an eccentric mitral inflow jet masquerades as aortic regurgitation. *Anesthesia and analgesia*, 118 1:76–9, 2014.
- [72] Stephen B. Pope. *Turbulent Flows*. Cambridge University Press, 8 2000.
- [73] Anne-Catherine Pouleur, Jean-Benoit le Polain de Waroux, Céline Goffinet, David Vancraeynest, Agnes Pasquet, Bernhard Gerber, and Jean-Louis Vanoverschelde. Accuracy of the flow convergence method for quantification of aortic regurgitation in patients with central versus eccentric jets. *The American journal of cardiology*, 102:475–80, 08 2008.
- [74] W. R. Quinn. On mixing in an elliptic turbulent free jet. *Physics of Fluids A*, 1(10):1716–1722, October 1989.
- [75] Markus Raffel, Christian Willert, Fulvio Scarano, Christian J. Kähler, Steven T. Wereley, and Jürgen Kompenhans. *Particle Image Velocimetry - A Practical Guide (3rd Edition)*, volume 1. Springer Verlag, April 2018.
- [76] Vrishank Raghav, Sudeep Sastry, and Neelakantan Saikrishnan. Experimental assessment of flow fields associated with heart valve prostheses using particle image velocimetry (piv): Recommendations for best practices. *Cardiovascular Engineering and Technology*, 9, 03 2018.
- [77] Vitor Rosa, João Fernandes, Antonio Lopes, Tarso Accorsi, and Flávio Tarasoutchi. Recommendation of early surgery in primary mitral regurgitation: Pros and cons. *Arquivos Brasileiros de Cardiologia*, 107, 08 2016.

- [78] Omer San and Anne Staples. An improved model for reduced-order physiological fluid flows. *Journal of Mechanics in Medicine and Biology*, 12, 10 2012.
- [79] H. Schlichting and K. Gersten. *Boundary-Layer Theory*. Springer, 8th edition, 2000.
- [80] Simon Sonntag, Wei Li, Michael Becker, Wiebke Kaestner, Martin Büsen, Nikolaus Marx, Dorit Merhof, and Ulrich Steinseifer. Combined computational and experimental approach to improve the assessment of mitral regurgitation by echocardiography. *Annals of biomedical engineering*, 42, 01 2014.
- [81] Joseph H. Spurk and Nuri Aksel. *Strömungslehre einföhrung in die theorie der strömungen*, 2007.
- [82] Vincent Strouhal. Ueber eine besondere art der tonerregung. *Annalen der Physik*, 241:216–251, 1878.
- [83] Sugantha Sundar, Devi Mahendran, and Eswar Sundar. *Anesthetic goals in patients withvalvular heart disease*, page 28–36. Cambridge University Press, 2011.
- [84] Cameron Tropea, Alexander Yarin, and John Foss. *Springer Handbook of Experimental Fluid Mechanics*. Springer Verlag, 01 2007.
- [85] Y. Tsuchiya, C. Horikoshi, and T. Sato. On the spread of rectangular jets. *Experiments in Fluids*, 4(4):197–204, July 1986.
- [86] Muthiah Vaduganathan, George A. Mensah, Justine Varieur Turco, Valentin Fuster, and Gregory A. Roth. The global burden of cardiovascular diseases and risk. *Journal of the American College of Cardiology*, 80(25):2361–2371, 2022.
- [87] Alec Vahanian, Friedhelm Beyersdorf, Fabien Praz, Milan Milojevic, Stephan Baldus, Johann Bauersachs, Davide Capodanno, Lenard Conradi, Michele De Bonis, Ruggero De Paulis, Victoria Delgado, Nick Freemantle, Martine Gilard, Kristina H Haugaa, Anders Jeppsson, Peter Jüni, Luc Pierard, Bernard D Prendergast, J Rafael Sádaba, Christophe Tribouilloy, Wojtek Wojakowski, ESC/EACTS Scientific Document Group, and ESC National Cardiac Societies. 2021 ESC/EACTS Guidelines for the management of valvular heart disease: Developed by the Task Force for the management of valvular heart disease of the European Society of Cardiology (ESC) and the European Association for Cardio-Thoracic Surgery (EACTS). *European Heart Journal*, 43(7):561–632, 08 2021.
- [88] C. Vlachopoulos, M. O’Rourke, and W.W. Nichols. *McDonald’s Blood Flow in Arteries: Theoretical, Experimental and Clinical Principles*. CRC Press, 2011.
- [89] S Wang, L Lee, and J Lee. A linear relation between the compressibility and density of blood. *The Journal of the Acoustical Society of America*, 109:390–6, 02 2001.
- [90] F.M. White. *Fluid Mechanics*. McGraw-Hill International Editions. WCB/McGraw-Hill, 1999.
- [91] Philip C. Wiener, Evan J. Friend, Ruchika Bhargav, Kirthi Radhakrishnan, Lyes Kadem, and Gregg S. Pressman. Color doppler splay: A clue to the presence of significant mitral regurgitation. *Journal of the American Society of Echocardiography*, 33(10):1212–1219.e1, 2020.
- [92] J. R. Womersley. Method for the calculation of velocity, rate of flow and viscous drag in arteries when the pressure gradient is known. *The Journal of Physiology*, 127, 1955.
- [93] Jie-Zhi Wu, Hui-Yang Ma, and Ming-De Zhou. *Vorticity and Vortex Dynamics*. 01 2006.

- [94] Harekrishna Yadav, Amit Agrawal, and Atul Srivastava. Mixing and entrainment characteristics of a pulse jet. *International Journal of Heat and Fluid Flow*, 61, 08 2016.
- [95] Shiyong Yao, Yong Guo, Nan Jiang, and Junjie Liu. An experimental study of a turbulent jet impinging on a flat surface. *International Journal of Heat and Mass Transfer*, 83:820–832, 04 2015.
- [96] Chaim Yosefy, Judy Hung, Sarah Chua, Mordehay Vaturi, Thanh-Thao Ton-Nu, Mark Handschumacher, and Robert Levine. Direct measurement of vena contracta area by real-time 3-dimensional echocardiography for assessing severity of mitral regurgitation. *The American journal of cardiology*, 104:978–83, 10 2009.
- [97] Alexander Zhivov, Håkon Skistad, Elisabeth Mundt, Vladimir Posokhin, Mike Ratcliff, Eugene Shilkrot, Andrey Strongin, Xianting Li, Tengfei Zhang, Fuyun Zhao, Xiaoliang Shao, and Yang Yang. *Principles of air and contaminant movement inside and around buildings*. Academic Press, 01 2020.
- [98] J. Zhou, Ronald Adrian, Sivaramakrishnan Balachandar, and T.M. Kendall. Mechanisms for generating coherent packets of hairpin vortices in channel flow. *Journal of Fluid Mechanics*, 387:353–396, 05 1999.
- [99] Li Zhou, Michael Grushko, James Tauras, and Cynthia Taub. Initial misdiagnosis of acute flail mitral valve is not infrequent: The role of echocardiography. *Journal of cardiovascular disease research*, 4:123–6, 06 2013.
- [100] William A Zoghbi, David Adams, Robert O Bonow, Maurice Enriquez-Sarano, Elyse Foster, Paul A Grayburn, Rebecca T Hahn, Yuchi Han, Judy Hung, Roberto M Lang, Stephen H Little, Dipan J Shah, Stanton Shernan, Paaladinesh Thavendiranathan, James D Thomas, and Neil J Weissman. Recommendations for noninvasive evaluation of native valvular regurgitation: A report from the american society of echocardiography developed in collaboration with the society for cardiovascular magnetic resonance. *J Am Soc Echocardiogr*, 30(4):303–371, March 2017.

Appendix

A Measurement Protocol

Time and Date	MROP	Name MROP	Comment	Nominal Width [mm]	Nominal Height [mm]	Nominal Area [mm ² (calc.)	Pump Settings	Fluid mixture (Water-Glycerin)	Compliance Volume [ml]	BPM [1/min]	Stroke Volume [ml]	Peak pressure LV [mmHg]	Laser	Frequency [Hz]	Pulse Distance [μs]	Laser Energy [μs]	
15.3.23 10:30		Pinhole S	phase-avg.	5,00		19,63		70-30									
15.3.23 11:50		Pinhole M	phase-avg.	9,00		58,90		70-30									
17.5.23 11:30		Pinhole L	phase-avg.	13,00		132,73		70-30	80	80	117	120		15	80	135	
17.5.23 15:10		Pinhole XL	phase-avg.	18,00		254,47		70-30	20	80	158,8	73		15	80	135	
17.5.23 17:31		Drop S	phase-avg.	5,00	10,00	19,19		70-30	80	80	69,7	120		15	80	135	
17.5.23 17:53		Drop M	phase-avg.	7,00	14,00	37,62		70-30	80	80	82,5	120		15	80	135	
17.5.23 18:19		Drop ML	phase-avg.	10,00	20,00	76,77		70-30	80	80	106,9	120		15	80	135	
19.5.23 9:21		Drop L	phase-avg.	14,00	28,00	150,47		70-30	20	80	152,4	80		15	80	135	
17.5.23 17:10		Slot S	phase-avg.	4,00	12,00	37,70		70-30	80	80	70,7	120		15	80	135	
17.5.23 16:48		Slot SM	phase-avg.	5,00	15,00	58,90		70-30	80	80	76,7	120		15	80	135	
18.5.23 16:47		Slot M	phase-avg.	7,00	21,00			70-30									
17.5.23 16:14		Slot L	phase-avg.	8,00	24,00	150,80		70-30	80	80	113,5	120		15	80	135	
17.5.23 15:43		Slot XL	phase-avg.	10,00	30,00	235,62		70-30	20	80	158,8	85		15	80	135	
19.5.23 10:20		DropL_phase	phase-res.	14,00	28,00	150,47		70-30	20	80	152,4	80		1,33	80	135	
19.5.23 11:10		PinholeL_phase	phase-res.	13,00		132,73		70-30	80	80	106,6	120		1,33	80	135	
17.08.2023 14:32		SlotL_phase	phase-res.	8,00	24,00			70-30	80	80	135	90		1,33	100	135	
21.08.2023 14:00		Ecclet_phase	phase-res.	8,00		50,27		70-30	80	80	105	120		1,33	100	135	
22.08.2023 11:37		DropM	phase-avg.	7,00	14,00	37,62		70-30	80	80	82,5	120		15	100	135	
22.08.2023 16:45		Patspez1_phase	phase-res.	30,00	10,00			70-30	60	80	150	120		1,33	100	135	

Figure A.1: Documentation of the PIV experiments conducted for this study, including the settings of the cardiac piston pump and the laser/synchronizer.